UNIVERSITÉ CATHOLIQUE DE LOUVAIN

FACULTY OF SCIENCE

EARTH AND LIFE INSTITUTE

EARTH AND CLIMATE RESEARCH CENTER

CLIMATE RESPONSE TO ASTRONOMICAL PARAMETERS, CO_2 AND ICE SHEETS DURING PAST INTERGLACIALS

DOCTORAL DISSERTATION PRESENTED BY

ZHIPENG WU

IN PARTIAL FULFILLMENT OF THE

REQUIREMENTS FOR THE DEGREE OF

DOCTOR IN SCIENCES

中国科学院地质与地球物理研究所
Institute of Geology and Geophysics, Chinese Academy of Sciences
中国科学院地球科学研究院
Innovation Academy for Earth Science, CAS

UNIVERSITY OF CHINESE ACADEMY OF SCIENCES

INSTITUTE OF GEOLOGY ANG GEOPHYSICS, CHINESE ACADEMY OF SCIENCES (CAS)

INNOVATION ACADEMY FOR EARTH SCIENCES, CAS

CLIMATE RESPONSE TO ASTRONOMICAL PARAMETERS, CO_2 AND ICE SHEETS DURING PAST INTERGLACIALS

DOCTORAL DISSERTATION PRESENTED BY

ZHIPENG WU

IN PARTIAL FULFILLMENT OF THE

REQUIREMENTS FOR THE DEGREE OF

DOCTOR IN SCIENCES

THESIS COMMITTEE:

Prof. Qiuzhen Yin (Supervisor)
Université catholique de Louvain

Prof. Zhengtang Guo (Supervisor)
Institute of Geology and Geophysics, CAS

Prof. Kristof Van Oost (Chair)
Université catholique de Louvain

Prof. Yan Zhao
Institute of Geographic Sciences and Natural Resources Reseacrch, CAS

Prof. Michel Crucifix
Université catholique de Louvain

Prof. Hugues Goosse
Université catholique de Louvain

Prof. Qingzhen Hao
Institute of Geology and Geophysics, CAS

Prof. Haibin Wu
Institute of Geology and Geophysics, CAS

Contents

Acknowledgements..ix

Abstract...xiii

List of abbreviations...xvii

Chapter 1 Introduction...1

1.1 An overview of interglacial climate research..................................1

1.2 Diverse response of NH and SH climate to astronomical forcing, CO_2 and ice sheets..3

1.3 The half-precession cycles..8

1.4 Objectives and research questions...9

Chapter 2 Methods...13

2.1 Model description...13

2.2 Model evaluation..14

2.3 Experiments design and climate forcing.......................................27

Chapter 3 Hemisphere differences in response of sea surface temperature and sea ice to precession and obliquity.....................39

3.1 Introduction..39

3.2 The response of sea ice to precession and obliquity.....................42

3.3 The response of SST to precession and obliquity.........................49

3.4 Conclusions..52

Chapter 4 Effect of Hudson Bay closure on global and regional climate under different astronomical configurations...................55

4.1 Introduction..55

4.2 The effect of Hudson Bay closure on global and regional climate……………………………………………………………….58
4.3 The forcing mechanisms for the global and regional climate changes……………………………………………………...….62
4.4 Comparison of the effect of Hudson Bay closure with the effect of ice sheets…………………………………………………………....65
4.5 Conclusions..67
Chapter 5 Hemisphere differences in response of sea ice and sea surface temperature to astronomical parameters, CO_2 and Northern Hemisphere ice sheets...69
5.1 Introduction..69
5.2 Influence of astronomical parameters on sea ice and SST............70
5.3 Impacts of CO_2 on sea ice and SST...74
5.4 Effect of NH ice sheets on sea ice and SST..................................78
5.5 The relative importance of insolation, CO_2 and NH ice sheets on sea ice and SST...85
5.6 Comparison between simulated sea ice and SST with proxy records…………………………………………………………………88
5.7 Conclusions..90
Chapter 6 The half-precession signals during the Quaternary.....91
6.1 Introduction..91
6.2 The first compilation of the half-precession signals during the Quaternary..93
6.3 The half-precession signals over the past 800 ka………………....99

6.4 Simulated half-precession signals in LOVECLIM1.3...............103

6.5 Conclusions..113

Chapter 7 Comparison of Arctic and Southern Ocean sea ice between the last nine interglacials and the future........................117

7.1 Introduction..117

7.2 Sea ice difference between interglacials and the impact of insolation and CO_2……………………………………………...119

7.3 Comparison of sea ice between the past interglacials and the present..124

7.4 Comparison of sea ice between interglacials and the future..127

7.5 Conclusions..128

Chapter 8 Conclusions and perspectives......................................131

8.1 Conclusions..131

8.2 Perspectives..134

Supplement to Chapter 3..137

Supplement to Chapter 6..141

References..145

Publications and Presentations...173

Acknowledgements

Science is the most important and most beautiful thing in the world, but the pursuit of science takes special courage. Many thanks to the people who have helped me during my PhD study, I could not finish my PhD thesis without your help.

First of all, I would like to express my deepest gratitude to my two supervisors, Prof. Qiuzhen Yin and Prof. Zhengtang Guo, for their continuous guidance, support, help and kindness. I am very grateful to Prof. Qiuzhen Yin, you help me to open the door of the climate simulations and lead me to enjoy the world of paleoclimate simulations. You spend lots of time and energy in teaching me how to make a good research, how to do numerical experiments, how to write a good paper and how to make a good presentation. Not only in my study and work, but you also give a lot of help in my life. I greatly appreciate everything you have done for me. I especially thank Prof. Zhengtang Guo for his guidance and for sharing his knowledge on how to be a responsible person and how to do a good job in scientific research. During the worst COVID-19 situation in China, you organized a group meeting almost every week. Your accompaniment through this difficult time was especially important for me. I feel very lucky to have the opportunity to be the student of Prof. Qiuzhen Yin and Prof. Zhengtang Guo, I am always inspired by your rigorous academic attitudes and insightful ideas.

Many many special thanks to Prof. André Berger. I am so grateful to have worked with you not only because you are such a great and famous scientist but also because of your great personality and kindness. Your continous love for science and hard working on it even after your retirement is worth of my lifelong learning. Not only have you given me many very useful suggestions for my study and work, but also you have helped me a lot in my life, you take care of me like my grandfather. When I was sick, you even helped me to ask for appointment with the doctor. I greatly appreciate everything you have done for me.

Many thanks to the two supervisory panel members of my doctoral study, Prof. Michel Crucifix and Prof. Hugues Goosse, for your support and discussions through my doctoral study. You are always available when I ask for help and advice. Many thanks to Prof. Yan Zhao, Prof. Qingzhen Hao and Prof. Haibin Wu for accepting to be the jury members of my thesis. Thank you all for spending your time to review my thesis and to provide many very useful comments and suggestions, which greatly improved my thesis. Many thanks to the chairman of my thesis committee, Prof. Kristof Van Oost, for your valuable time and chair of my private and public defenses.

Many thanks to Pierre-Yves Barriat and CISM team for your patience and support in helping me to solve many problems related to the model and servers during my PhD study. Many thanks to Livia Lai, Dominique Angelot and Alice Gasasira for your kind help in providing comfortable and convenient environment for my study and work at Mercator.

Many thanks to my colleagues in Prof. Yin’s research group: Prof. Guoqiao Xiao, Hao Lu, Qianqian Su, Anqi Lyu, Rui Zhang, Yun Li, Chengguang Pan, Mingqiang Liang, Wei Liu and Ranathunga Arachchige Keerthika Nirmani. We have worked together, attended meetings, discussed research and personal questions, traveled and did sports together, I have learned a lot from you. Prof. Guoqiao Xiao and Hao Lu gave me a lot of advice on my research, Qianqian Su gave me lots of help in my life, Anqi Lyu taught me to use HadCM3 and emulator, Mingqiang Liang gave me many good suggestions on Matlab codes and Wei Liu helped me to solve many problems especially at the end of my PhD study. Many special thanks to Fu Liu and Mei-Li Liu, you drove me to travel many beautiful places and invited me to eat lots of delicious food in both the restaurants and your home. In addition, you gave me many very useful suggestions to deal with the problems of my life. I really enjoy the life in Belgium under your help.

Many thanks to the professors and students in Prof. Guo's research group: Prof. Feng Shi, Prof. Chenglong Deng, Prof. Chunxia Zhang, Prof. Yanyan Yu, Prof. Chenxi Xu, Wenlin An, Bin Hu, Ning Tan, Xiaolin Ren, Zhilin He, Yang Fu, Long Chen, Chaoqin Chen, Zijian Zhang, Zijuan Yang, Yuzhe Zhang, Xinbo Gao, Qida Jiang, Pengcheng Tan, Xuechao Wu, Mingliang Zhou, Yucheng Liu. Under your help, my study and life in Beijing was wonderful.

Many special thanks to my most sincere friends, Min Chen and Mingyue Xu.

Warmest thanks to my girlfriend, Fuzhen Li, for your love and for being with me. We have so many beautiful memories in Beijing and in Louvain-la-Neuve, and I feel blessed to be with you.

Warmest thanks to my parents, Baixiang Dong and Yonghong Wu, and my little brother, Zhixiang Wu, for your unconditional love and support all the time. You are my strongest backing forever.

This PhD project is supported by the Fonds de la Recherche Scientifique-FNRS (F.R.S.-FNRS) under Grant MIS F.4529.18 and Grant n° T.0246.23, and the National Natural Science Foundation of China (Grant No. 41888101). Computational resources have been provided by the supercomputing facilities of the Université catholique de Louvain (CISM/UCL) and the Consortium des Équipements de Calcul Intensif en Fédération Wallonie Bruxelles (CÉCI) funded by the Fond de la Recherche Scientifique de Belgique (F.R.S.-FNRS) under convention 2.5020.11.

Abstract

Characterized by warm climate, small ice sheets and high sea level, past interglacials are quite relevant for a better understanding of our present-day warm climate and its future evolution. Investigating the response of climate system to different forcing factors, such as astronomical parameters, greenhouse gases (GHG) and ice sheets, could help better constrain the uncertainty of the sensitivity of the climate system and provide a basis for better understanding the internal climate processes and feedbacks. This thesis aims to perform a comprehensive and systematic investigation of the climate response in the two hemispheres to astronomical parameters, CO_2 and Northern Hemisphere (NH) ice sheets during the interglacials of the past 800 ka mainly based on snapshot and transient simulations using the LOVECLIM model.

The results show that the climate of the two hemispheres responds differently to astronomical parameters, CO_2 and NH ice sheets. In terms of the effect of astronomical parameters, precession plays a dominant role on the Arctic sea ice, while obliquity plays a dominant role on the Southern Ocean sea ice. This is mainly related to the different geographical condition of the Arctic and the Southern Ocean and the related atmospheric and oceanic feedbacks. In the low latitudes of both hemispheres, SST shows a strong precession signal. However, in the mid and high latitudes, obliquity plays a dominant role on the Southern Hemisphere (SH) SST whereas precession is more important on the NH SST. This is largely due to the different response to insolation and feedbacks related to the different land-ocean distribution in the two hemispheres. The model results also show that the effect of CO_2 on the SST in the mid-high latitudes is larger than in the low latitudes of both hemispheres, and CO_2 plays a more important role on the SST at mid-high latitudes and sea ice in the SH than in the NH.

The status of the Hudson Bay changed (closed or open) with the advance and retreat of the North American ice sheet. Therefore, before investigating the effect of the NH ice sheets on the climate, the effect of Hudson Bay closure on global and regional climate under different astronomical configurations was studied. The results show that the closure of the Hudson Bay could lead to a strengthening of the Atlantic Meridional Overturning Circulation (AMOC), which in turn leads to a warming in the NH with notable warming in the Labrador Sea and northeast North Atlantic, a cooling in the SH and a northward shift of the Inter-tropical Convergence Zone (ITCZ). In addition to the large-scale climate changes, the closure of Hudson Bay also leads to a strong cooling over the Hudson Bay region due to changes of surface properties and a cooling to the southeast of Greenland due to more wind-driven sea ice export from the Arctic. However, the effect of the Hudson Bay closure depends on background climate conditions, and it could weaken or slightly reinforce the effect of the ice sheets for different astronomical configurations.

When the effect of the NH ice sheets is considered, the changes in Southern Ocean sea ice are highly and positively correlated with the NH ice volume, but the effect of the NH ice sheets on Arctic sea ice appears nonlinear, which depends on the size and location of the ice sheets as well as the NH summer insolation. The response of the mid-high latitude SST to the NH ice sheets is similar to the sea ice response in the same hemisphere. If the relative effect of insolation, CO_2 and NH ice sheets is concerned, the NH mid-high latitude SST and sea ice are dominated by insolation, while the SH mid-high latitude SST and sea ice are dominated by ice sheets. Both CO_2 and NH ice sheets play an important role in the SST at low latitudes of the two hemispheres.

The half-precession cycles are systematically investigated based on both proxy records and transient simulations for the past interglacials. A compilation of available proxy records and the reanalysis of seven long, high-resolution records covering a wide region from Arctic to Antarctic, show that the half-precession signals are persistent and widely distributed at least over the last 800 ka, although their strength varies in time and regions. Our simulated results show that in response to the maximum equatorial insolation, the half-precession cycles can be simulated in the SST, surface air temperature (SAT) and precipitation near the Equator, and the half-precession signals in the tropics can be transported to the mid and high latitudes through oceanic circulations. The half-precession cycles can also be simulated in the grass fraction in the 'Asian' and 'African' monsoon regions due to vegetation feedbacks. Both eccentricity (and therefore precession) and obliquity can affect the strength of the half-precession signals. It is suppressed when eccentricity is small (leading to weak variation of precession) and obliquity variation is large, and vice versa. The half-precession signals are also weakened if the long-term variations of GHG and NH ice sheets are taken into account.

Finally, the variations of the Arctic and Southern Ocean sea ice during the peak interglacials are investigated and compared with the sea ice of the present and future. The results show that the annual mean Arctic sea ice variation is primarily controlled by local summer insolation, while the annual mean Southern Ocean sea ice variation is more influenced by the CO_2 concentration but the effect of local summer insolation can't be ignored. The lowest Arctic sea ice area results from the highest summer insolation at MIS-15, and the lowest Southern Ocean sea ice area at MIS-9 is explained by the highest CO_2 concentration and moderate local summer insolation. As compared to the present, the last nine interglacials all have much less sea ice in the Arctic annually and seasonally due to high summer insolation. They also have much less Arctic sea ice in summer than the double CO_2 experiment, which makes to some degree the interglacials possible analogues for the future in terms of the changes of sea ice. However, compared to the double CO_2 experiment, the interglacials all have much more sea ice in the Southern Ocean due to their much lower CO_2 concentration, which suggests the inappropriateness of considering the interglacials as analogues for the future in the Southern Ocean. The results suggest that in the search for potential analogues of the present and future climate, the seasonal and regional climate variations should be considered.

List of abbreviations

AMOC	Atlantic meridional overturning circulation
BP	Before present
CMIP	Coupled Model Intercomparison Project
DO	Dansgaard-Oeschger
EASM	East Asian summer monsoon
ECS	Equilibrium climate sensitivity
EMIC	Earth system model of Intermediate Complexity
ENSO	El Niño-Southern Oscillation
GCM	General circulations model
GHG	Greenhouse gases
IPCC	Intergovernmental Panel on Climate Change
ITCZ	Intertropical Convergence Zone
ka	Thousand years
LGM	Last Glacial Maximum
MBE	Mid-Brunhes Event
MBT	Mid-Brunhes Transition
MHT	Meridional heat transport
MIS	Marine isotope stages
NH	Northern hemisphere
ODP	Ocean Drilling Program
OHC	Ocean heat content
PAGES	Past Global Changes Project
PI	Pre-industrial
PMIP	Paleoclimate Modelling Inter-comparison Project
SAT	Surface air temperature
SCS	South China Sea
SH	Southern Hemisphere
SSP	Shared Socioeconomic Pathway
SST	Sea surface temperature
WEP	Western equatorial Pacific

Chapter 1 Introduction

1.1 An overview of interglacial climate research

Global warming has been confirmed by numerous observational data, and many of the observed changes are unprecedented over the last millennium, mainly due to the increased anthropogenic CO_2 emissions (IPCC, 2021). Global surface temperature is predicted to continue to increase at least over the next decades, which would have a great effect on the environment, ecosystems, biodiversity, agriculture and the society (IPCC, 2021). However, both the understanding of the present-day climate variability and the prediction of future climate changes are still facing great challenges largely due to the lack of long-term observations.

An interglacial is the warmer time period between glacials where glaciers retreat and sea levels rise (Past Interglacials Working Group of PAGES, 2016). The Quaternary interglacials, as the most recent warm periods in the Earth's history, provide a good opportunity to better understand internal climate processes and related feedbacks during warm intervals, which would be helpful for a better understanding of our present-day warm climate and its future changes. Moreover, past interglacials can also be used to investigate the response of climate system to different external forcings, including astronomical parameters, CO_2 and ice sheets, over a wide range of background climate situations, which could help to improve our estimate of the sensitivity of the climate system to different drivers.

Due to data availability, a large number of studies have focused on the interglacials of the last 800 ka. Our current interglacial, the Holocene, which is tightly related to our present-day climate and its future, has probably received the greatest attention (e.g. Crucifix et al., 2002; Renssen et al., 2009). In order to find possible analogues of our current interglacial and its future, Marine Isotope Stage (MIS)-5e, -9, -11 and -19 are often considered. MIS-5e (the last interglacial) is the most recent interglacial with higher temperature especially at NH high latitudes, reduced ice sheets and higher global sea level than our present interglacial, which may provide a suitable analog with the IPCC predictions of our future global warming climate (CAPE-Last Interglacial Project Members, 2006; NEEM community members, 2013; Past Interglacials Working Group of PAGES, 2016). With small eccentricity related to the 400-kyr cycle of eccentricity, MIS-11 and MIS-19 have been considered as good astronomical analogues for the present interglacial MIS-1 (Berger and Loutre, 2002, 2003; Loutre and Berger, 2003; Tzedakis, 2010; Tzedakis et al., 2012; Yin and Berger, 2010, 2012, 2015). MIS-11 and MIS-19 have also been confirmed to be possible analogues for the MIS-1 and its future by proxy records (e.g. McManus et al., 2003; Pol et al., 2010). Numerous reconstructions show that MIS-11 was characterized by significantly smaller ice sheets and higher sea level than MIS-1 (e.g. Olson and Hearty, 2009; Raymo and Mitrovica, 2012), which gives another reason of considering MIS-11 as a good analogue for the future climate. If the phasing between obliquity and precession, and the caloric summer half-year insolation are considered, MIS-9 was suggested to be the closest insolation analogue for the MIS-1 (Ruddiman, 2007). In addition, modelling simulations show that MIS-9 is the simulated warmest interglacial over the last 800 ka due to its high CO_2 concentration and an in-phase relationship between obliquity maximum and precession minimum (Yin and Berger, 2012, 2015).

Different from MIS-1, -5, -9, -11 and -19 which are more popularly studied by the paleoclimate community, MIS-13 is less studied but it is a very intriguing interglacial due to its extremely asymmetrical hemispheric climate (Yin and Guo, 2008; Yin et al., 2008, 2009; Guo et al., 2009; Shi et al., 2020). The Antarctic ice core records show that MIS-13 is a cool interglacial (Jouzel et al., 2007) with relatively low CH_4 and CO_2 concentrations (Loulergue et al., 2008; Lüthi et al., 2008) among the nine interglacials of the past 800 ka, and the ocean sediments also indicate MIS-13 is a relatively weak interglacial compared with more recent interglacials, suggesting higher ice volume and/or cooler deep-ocean temperature (Lisiecki and Raymo, 2005). However, the Chinese loess records suggest an exceptionally strong East Asian summer monsoon (EASM) during MIS-13 (Guo et al., 1998, 2009; Yin and Guo, 2006, 2008). Besides the Chinese loess records, abundant proxy records in the NH also suggest a warm climate during MIS-13 (e.g. Rzechowski, 2020; Fawcett et al., 2011). In addition to the six interglacials discussed above, other three interglacials, MIS-7, MIS-15 and MIS-17, are also paid attention by both modelling and proxy communities (e.g. Asami et al., 2013; Rowe et al., 2014; Past Interglacials Working Group of PAGES, 2016; Goñi et al., 2019).

Thanks to the numerous studies on the past interglacials, our understanding of the interglacial climate changes during the last 800 ka has been greatly improved, but many questions still remain. Some key questions which are still not fully understood and deserve more in-depth study include for example: (1) what caused the Mid-Brunhes Event (or Transition) about 430 ka ago, (2) what caused the interglacial diversity in terms of their intensity, duration, internal variability and their temporal and spatial diversity, (3) how and when an interglacial start and end, (4) how the climate system respond to different external forcings, like insolation, CO_2 and ice sheets, and what are the important internal processes and feedbacks, and (5) what cause the sub-orbital (here defined as the periodicities <15 ka) timescale climate changes within the interglacials.

1.2 Diverse response of NH and SH climate to astronomical forcing, CO_2 and ice sheets

A large number of evidences show that the response of climate system to different external forcings depends strongly on different climate variables, different time periods and on different regions. For example, the pollen records of the past 1.7 Ma from eastern Tibetan Plateau indicate that the vegetation and climate changes there display strong ~20 ka cycles during the interval 1.74-1.54 Ma and strong ~20 ka and ~40 ka cycles during 1.54-0.62 Ma, while they are dominated by the

~100 ka cycle during the past 0.62 Ma (Zhao et al., 2020). For a given time period, proxies of different regions could show different characteristics. For example, during 1.25-0.7 Ma, the IRD record in the northeastern Atlantic show strong precession cycles, but no precession signal was found in the benthic $\delta^{18}O$ record in the western Indian ocean (Barker et al., 2022). Although both are considered as indicators for the East Asian summer monsoon, the loess records in North China show strong glacial-interglacial cycles (Hao et al., 2012), but the speleothem records in South China mainly show precession cycles (Cheng et al., 2016). In Antarctica, the total air content in the ice core, which may represent the local summer temperature, is dominated by obliquity cycles (Raynaud et al., 2007), while the δD in the ice core, which may represent annual mean temperature, is dominated by glacial-interglacial cycles (Jouzel et al., 2007).

On hemisphere scale, evidence from both proxy records and numerical simulations shows that the climate changes in the two hemispheres seem to respond differently to astronomical parameters, CO_2 and ice sheets. Polyak et al. (2010) found that the Arctic sea ice was apparently most wide-spread during the Quaternary, which is related to the overall cooler climate due to the formation of NH permanent ice sheets. Nevertheless, there still exist time periods of considerably reduced sea ice and even seasonally ice-free conditions, which are mainly controlled by the orbital variations (Polyak et al., 2010). Cronin et al. (2017) suggested a major shift towards perennial sea ice in the western Arctic Ocean occurred after MIS-11 using sea-ice planktic and benthic indicator species. Based on the results of sea ice indicator (ostracode assemblages) in the western Arctic Ocean, Cronin et al. (2013) found that the Arctic sea ice varied mainly at precession and obliquity frequencies with precession playing a more important role during the last 600 ka. The novel organic geochemical proxies of sea ice (IP25) in the central Okhotsk Sea indicated that autumn Arctic sea ice extent was governed by insolation for an atmospheric CO_2 concentration ranging from 190 to 260 ppmv during the last 130 ka (Lo et al., 2018). In the Southern Ocean, the ssNa flux-reconstructed sea ice shows that it was dominated by glacial-interglacial cycles over the past 800 ka, with the main periodicity of about ~100 ka (Wolff et al., 2006). These results indicate that the Arctic and Southern Ocean sea ice show significantly different characteristics on orbital timescale. The Arctic sea ice is mainly controlled by insolation with precession playing a dominant role, while the Southern Ocean sea ice is well followed the glacial-interglacials cycles (Figure 1.1).

The SST variations at different latitudinal bands of the two hemispheres also show significant difference based on proxy reconstructions (Figure 1.2). In addition to the glacial-interglacial cycles (about ~100 ka), the SST variations also contain obliquity and precession signals. However, precession is more important at low latitudes than at mid and high latitudes in both hemispheres. Precession is also more important at mid and high latitudes in the NH than that in the SH, while obliquity is more important in the SH than in the NH (e.g. Ruddiman et al., 1989; Liu and Herbert, 2004; Medina-Elizalde and Lea, 2005; Schaefer et al., 2005; Lawrence et al., 2009; Herbert et al., 2010). Based on snapshot and transient simulations during the last nine interglacials, Yin and Berger (2012, 2015) found that insolation is more important in the NH, while CO_2 is more important in the SH.

Although hemisphere differences in climate response to astronomical forcing, CO_2 and ice sheets have been widely observed in proxy records, the cause and mechanism are still not very well understood. This is mostly because in geological records, it is not easy to distinguish the individual effect of astronomical parameters, CO_2 and ice sheets as they contain common periodicities and jointly act on the proxy records. Very few model simulations deal with this topic. Therefore, there is a need to comprehensively and systematically investigate the different response of different components of the climate system to astronomical parameters, CO_2 and ice sheets between the two hemispheres using numerical simulations.

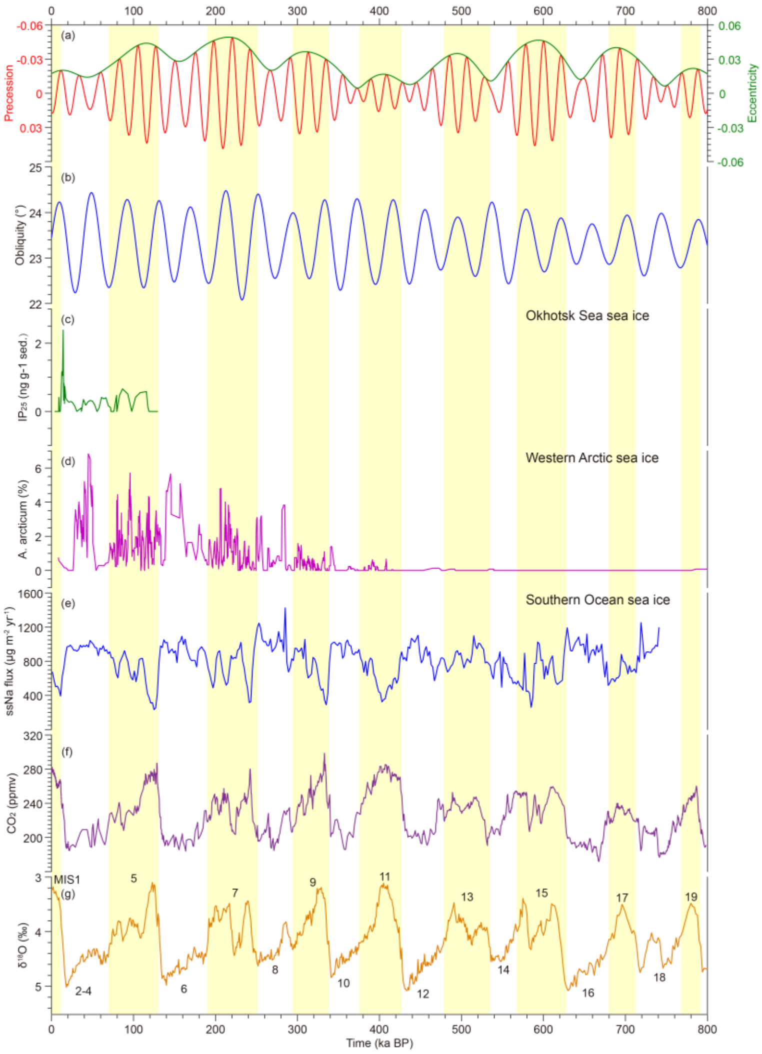

Figure 1.1 Reconstructed Arctic and Southern Ocean sea ice from proxy records over the past 800 ka and their possible external forcings. (a) eccentricity (green line) and precession (red line), (b) obliquity (Berger and Loutre, 1991), (c) IP25-reconstructed Okhotsk Sea sea ice (Lo et al., 2018), (d) ostracode-reconstructed western Arctic sea ice (Cronin et al., 2017), (e) ssNa flux-reconstructed Southern Ocean sea ice (Wolff et al., 2006), (f) CO_2 concentration (Lüthi et al., 2008), (g) LR04 $\delta^{18}O$ (Lisiecki and Raymo, 2005). The numbers of MIS stages are indicated; the yellow shaded vertical bars indicate interglacial periods and non-shaded bars indicate glacial periods.

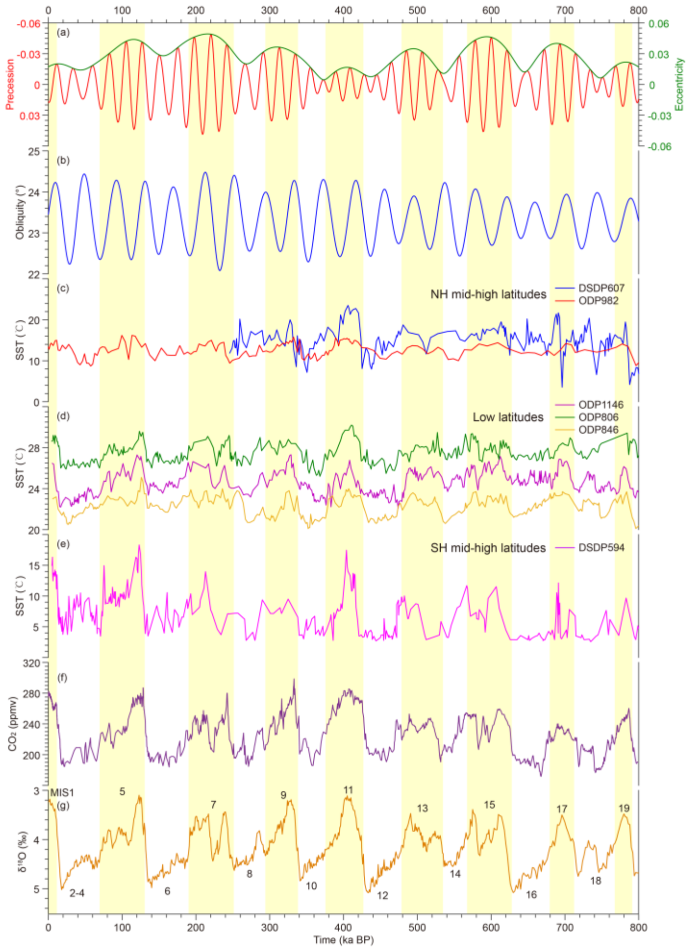

Figure 1.2 Reconstructed SST at different latitudinal bands from proxy records over the past 800 ka and their possible external forcings. (a) eccentricity (green line) and precession (red line), (b) obliquity (Berger and Loutre, 1991), (c) SST at NH mid-high latitudes from cores DSDP607 (blue line, Ruddiman et al., 1989) and ODP982 (red line, Lawrence et al., 2009), (d) SST at low latitudes from cores ODP1146 (pink line, Herbert et al., 2010), ODP806 (green line, Medina-Elizalde and Lea, 2005) and ODP846 (yellow line, Liu and Herbert, 2004), (e) SST at SH mid-high latitudes from core DSDP594 (Schaefer et al., 2005) (f) CO_2 concentration (Lüthi et al., 2008), (g) LR04 $\delta^{18}O$ (Lisiecki and Raymo, 2005). The numbers of MIS stages are indicated; the yellow shaded vertical bars indicate interglacial periods and non-shaded bars indicate glacial periods.

1.3 The half-precession cycles

In addition to orbital timescale climate changes, a large number of sub-orbital timescale climate variations have also been discovered during the interglacials (e.g. Rutherford and D'Hondt, 2000; Guo et al., 2012; Cheng et al., 2016; Hodell et al., 2015; Sun et al., 2021a). However, the climate changes on sub-orbital timescale are far less understood than those on orbital timescale, which are partly due to the lack of linear forcing mechanisms for different sub-orbital timescale climate variations.

Among different sub-orbital timescale climate changes, the climate changes with a periodicity near ~10 ka, also called the half-precession cycle, have received more attention, including the forcing mechanisms and the related processes and feedbacks. This is because : (1) the climate variations with half-precession cycles can be directly explained by the equatorial maximum insolation (Berger et al., 2006), which would be the first step to understand the sub-orbital timescale climate variations; (2) both proxy records and numerical simulations indicate that a better understanding of the half-precession signal could help understand other important climate changes, like the Dansgaard-Oeschger (DO) events (Hinnov et al., 2002; Deng et al., 2018) and the mid-Pleistocene transition (Rutherford and D'Hondt, 2000; Le Treut and Ghil, 1983; Berger et al., 2006); (3) the half-precession signals are normally originated from the tropics (Berger et al., 2006; Guo et al., 2012) and can be transported to mid and high latitudes through atmospheric and oceanic circulations (Hernández-Almeida et al., 2012; Ferretti et al., 2010, 2015). Therefore, understanding the half-precession cycles in climate variations could help to give a more comprehensive picture on how the low latitude climate would affect the global climate and on the high-low latitudes interactions (Wang et al., 2014, 2017).

The half-precession signals have been found in different kinds of geological records, such as marine sediments (Weirauch et al., 2008; Billups and Scheinwald, 2014), lake sediments (Trauth et al., 2003;

Ulfers et al., 2022), ice cores (Guo et al., 2012), loess (Sun and Huang, 2006) and vegetation (Turney et al., 2004). Some possible forcing mechanisms have been proposed to explain the half-precession signals, including the equatorial maximum insolation (Berger et al., 2006), the bi-hemisphere insolation at low latitudes (Guo et al., 2012), the combination tones of the orbital cycles due to a nonlinear climatic oscillator (Le Treut et al., 1988; Guo et al., 2012) and the internal processes and feedbacks in response to precession (Tuenter et al., 2007). However, they are often not easy to be distinguished mainly due to the interactions of different climate components. For example, both the equatorial maximum insolation and the bi-hemisphere insolation at low latitudes are the tropic forcings and both of them have been used to explain the half-precession signals in the hydrological changes in equatorial East Africa (Trauth et al., 2003; Verschuren et al., 2009). Moreover, the spatial distribution of the half-precession cycles is still unclear due to a lack of comprehensive compilation of the half-precessional signal. Therefore, a comprehensive and systematical investigation of the half-precession signals, including their forcing mechanisms and the related internal processes and feedbacks, is needed.

1.4 Objectives and research questions

1.4.1 Research questions and outlines

Sections 1.1, 1.2 and 1.3 give an overview on the studies on interglacials, the hemisphere differences in climate response to different forcing factors and the half-precession cycles, and they highlight the major existing questions. This thesis does not intend to answer all the questions raised but tryies to focus on several major ones. Its main objective is to make a comprehensive and systematic investigation on the different response of major climate variables to astronomical parameters, CO_2 and NH ice sheets, as well as the half-precession cycles during the interglacials of the last 800 ka, including MIS-1, -5, -9, -11, -13, -15, -17 and -19. The major research questions that are intended to be answered in this thesis include:

(1) What are the major differences of the NH and SH climate in response to astronomical parameters, CO_2 and ice sheets?
(2) How about the spatial distribution of the half-precession signals and what are the major forcing mechanisms for selected climate variables?
(3) What are the differences between the interglacials in terms of their response to different external forcings and between the past interglacials and the present and future?

These questions will be answered mainly based on model simulations, but proxy records are also used to give a complementary view. The models used and the experiments design are described in Chapter 2. The results are presented in Chapters 3-7. Chapter 3 studies the hemisphere differences in the response of SST and sea ice to precession and obliquity. As the Hudson Bay could be strongly affected by the advance and retreat of the North American ice sheet, its effect on global and regional climate is studied in Chapter 4. In Chapter 5, the hemisphere differences in the response of sea ice and SST to astronomical forcing, CO_2 and NH ice sheets during the interglacials MIS-13 and MIS-11 are comprehensively and systematically investigated. In Chapter 6, the half-precession signals, including their spatial distribution and different forcing mechanisms as well as the internal processes and feedbacks are investigated. In Chapter 7, the variations of the Arctic and Southern Ocean sea ice of the last nine interglacials are analyzed and compared with the present and future. Chapter 8 includes the main conclusions of this thesis and perspectives for future studies.

1.4.2 Research strategy and innovation

This study systematically investigates the response of different components of the climate system to astronomical parameters, CO_2 and NH ice sheets, as well as the half-precession cycles for the interglacials of the past 800 ka. The model used in this thesis is LOVECLIM, including two versions LOVECLIM1.2 and LOVECLIM1.3. LOVECLIM is a three-dimension Earth system

Model of Intermediate Complexity (EMIC). Due to its reduced complexity, LOVECLIM can be run faster and requires less compute resource as compared to more complex GCMs. It allows to perform long transient simulations and large ensemble of simulations. The number of modelling studies on investigating the individual and combined effect of insolation, CO_2 and ice sheets on different components of the climate system remains low and most studies cover a short period and use acceleration technique which could bias some results. In this thesis, the effects of astronomical parameters, CO_2 and ice sheets are investigated by using 28 long transient simulations without acceleration as well as many snapshot simulations performed for nine glacial-interglacial periods of the last 800ka.

Although the half-precession cycles have been observed in numerous paleoclimate records, the understanding of their mechanisms remains poor. This thesis has provided a first compilation of the half-precession signals during the Quaternary and reanalyzed seven high-resolution proxy records to discuss the characteristics of the spatial and temporal distribution of the half-precession cycles. The forcing mechanisms, as well as the internal processes and feedbacks, are investigated using transient climate simulations. This study is expected to timely provide some new insights for the response of different components of climate system to different external forcings, as well as the half-precession cycles during the past warm periods.

Chapter 2 Methods

2.1 Model description

The model used in this thesis is LOVECLIM, it is a three-dimension Earth system Model of Intermediate Complexity (EMIC). Five main components of the climate system are contained in LOVECLIM (Goosse et al., 2010), including the atmosphere (ECBilt, Opsteegh et al., 1998), the terrestrial biosphere (VECODE, Brovkin et al., 2002), the Greenland and Antarctic ice sheets (AGISM, Huybrechts, 2002), the ocean and sea ice (CLIO, Goosse and Fichefet, 1999) and carbon and biogeochemical cycles (LOCH, Mouchet and François, 1996). A comprehensive description and evaluation of LOVECLIM1.2 are provided in Goosse et al (2010) and a more recent version LOVECLIM1.3 is introduced in Loutre et al (2014). In this thesis, most simulations were performed with LOVECLIM1.3, while some simulations which had been performed with LOVECLIM1.2 before the release of LOVECLIM1.3 are also analyzed (see Section 2.3). In all the simulations, the ECBilt, CLIO and VECODE are interactively coupled, while the AGISM and LOCH are uncoupled.

The atmospheric model ECBilt, developed at KNMI, it is a spectral atmospheric model with truncature T21, which corresponds approximately to a horizontal resolution of 5.625°×5.625°. It has three vertical layers and its dynamics are governed by the quasi-geostrophic potential vorticity (Opsteegh et al., 1998). The sensitivity of ECBilt to small changes of topography is overall realistic (Timmerman et al., 2004). The terrestrial biosphere model VECODE is a reduced-form dynamical global vegetation model (DGVM) that simulates changes in vegetation structure and terrestrial carbon pools (Brovkin et al., 2002). Two primary plant functional types (tree and grass) are identified as the vegetation cover based on the fractional bioclimatic classifcation. Both the tree fraction and the desert fraction are calculated based on the relationship between climate (annual mean precipitation and growing degree days above 0 (GDD0)) and vegetation, and the grass fraction is the rest of the grid cell (Brovkin et al., 1997). Its horizontal resolution is the same as ECBilt. Despite the simplicity of VECODE, it has reasonably simulated the basic global vegetation patterns as compared to the present-day observations and proxy records, as well as the results of other more complex DGVM (Cramer et al., 2001). The ocean and sea ice model CLIO results from the coupling of a global free-surface ocean general circulation model (OGCM) and a thermodynamic-dynamic sea ice model, both developed at the Institut d'Astronomie et de Géophysique G. Lemaître, Louvain-la-Neuve (ASTR) of the UCLouvain (Goosse and Fichefet, 1999). A detailed formulation of boundary layer mixing based on Mellor and Yamada's (1982) level-2.5 turbulence closure scheme (Goosse and Fichefet, 1999) and a parameterization of density-driven downslope flows (Campin and Goosse, 1999) is included in OGCM. The heat capacity of the snow-ice system, the storage of latent heat in brine pockets trapped inside the ice, the effect of the subgrid-scale snow and ice thickness distributions on sea-ice thermodynamics, the formation of snow ice under excessive snow loading and the existence of leads within the ice cover all are considered in the sea ice model. The horizontal resolution of CLIO is 3° in longitude and latitude, and there are 20 unevenly spaced levels along vertical in the ocean (Goosse and Fichefet, 1999).

Within the hierarchy of EMICs, LOVECLIM is classified into the "simplified comprehensive model group" (Goosse et al., 2010). Its main advantage is that it is much faster and costs less compute resources, allowing to perform long transient simulations and large ensemble of simulations, as required by this study.

2.2 Model evaluation

The performances of LOVECLIM1.2 and LOVECLIM1.3 have been evaluated in Goosse et al. (2010) and Loutre et al. (2014) respectively. The performance of LOVECLIM1.2 have been evaluated from different aspects and for different time periods, including the last decades, the past millennium, the Holocene, the last glacial maximum and the last interglacial (Goosse et al., 2010). However, the performance of LOVECLIM1.3 was mainly evaluated for the last interglacial (Loutre et al., 2014). In this study, we mainly investigate the climate changes at different latitudes bands in response to astronomical parameters, CO_2 and NH ice sheets. Therefore, here the performance of LOVECLIM1.2 is further evaluated based on the comparison of its climate sensitivity with other models, and the performance of LOVECLIM1.3 is further evaluated based on the comparison of simulated present-day climate at different latitudinal bands with the observations.

2.2.1 The climate sensitivity of LOVECLIM1.2

To further evaluate the performance of LOVECLIM1.2, the climate sensitivity of LOVECLIM1.2 is investigated and compared with other model results from Phase 6 of the Coupled Model Intercomparison Project (CMIP6). First, the PI and 2xCO_2 experiments are used to analyze the equilibrium climate sensitivity (ECS). The ECS is a key point in projecting future climate change (Cox et al. 2018; Nijsse et al. 2020), and it is defined as the global mean surface air temperature increase once radiative equilibrium is reached in response to the atmospheric CO_2 concentration twice the pre-industrial level (Hansen et al. 1984; Rugenstein et al. 2020). The results show that the ECS of LOVECLIM1.2 is relatively low in comparison with other models from CMIP6 (Figure 2.1a). In addition to the ECS, the sensitivity of surface air temperature in the high latitudes of both two hemispheres to double CO_2 is also analyzed, because sea ice is essentially influenced by temperature in the high latitudes. For the sensitivity of surface air temperature in the northern mid-high latitudes (40°N-90°N), LOVECLIM1.2 is at the middle level of the CMIP6 models (Figure 2.1b), and it is at high level in the southern mid-high latitudes (40°S-90°S) (Figure 2.1c).

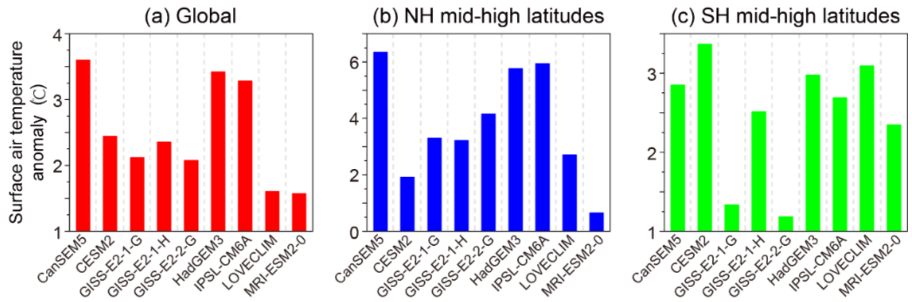

Figure 2.1 Surface air temperature anomaly of the $2xCO_2$ experiment relative to the PI experiment simulated by different models for (a) global, (b) NH mid-high latitudes (40°N-90°N) and (c) SH mid-high latitudes (40°S-90°S). The data of LOVECLIM1.2 is from this study, and those of other models are from CMIP6 and the data link is: https://esgf-data.dkrz.de/search/cmip6-dkrz/.

When the sea ice is concerned, the sensitivity of the global sea ice area in response to double CO_2 concentration in LOVECLIM1.2 is at the medium level (5th) among the nine models (Figure 2.2a). For the sensitivity of the Arctic sea ice area, LOVECLIM is within the low range and is only higher than CESM2 and MRI-ESM2-0 (Figure 2.2b), but it is at high level for the sensitivity of the Southern Ocean sea ice area (Figure 2.2c). These results have a good consistency with the sensitivity of surface air temperature to double CO_2 in the Arctic and Southern Ocean respectively. Considering the global, Arctic and Southern Ocean sea ice, LOVECLIM 1.2 is the closest to CESM2 among the nine models. Nevertheless, the sea ice concentration anomalies between the $2xCO_2$ and the PI simulations of these two models show some spatial difference. The extent of sea ice reduction in CESM2 is slightly larger than in LOVECLIM (Figure 2.3), which may be partly related to the higher resolution in CESM2.

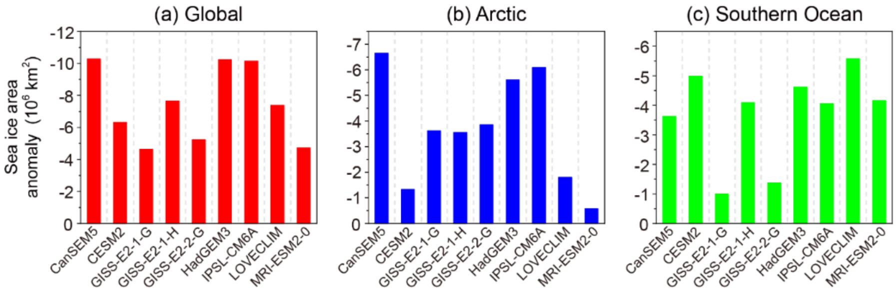

Figure 2.2 Sea ice area anomaly of the $2xCO_2$ experiment relative to the PI experiment simulated by different models for (a) global, (b) Arctic and (c) Southern Ocean. The data of LOVECLIM1.2 is from this study, and those of other models are from CMIP6 and the data link is: https://esgf-data.dkrz.de/search/cmip6-dkrz/.

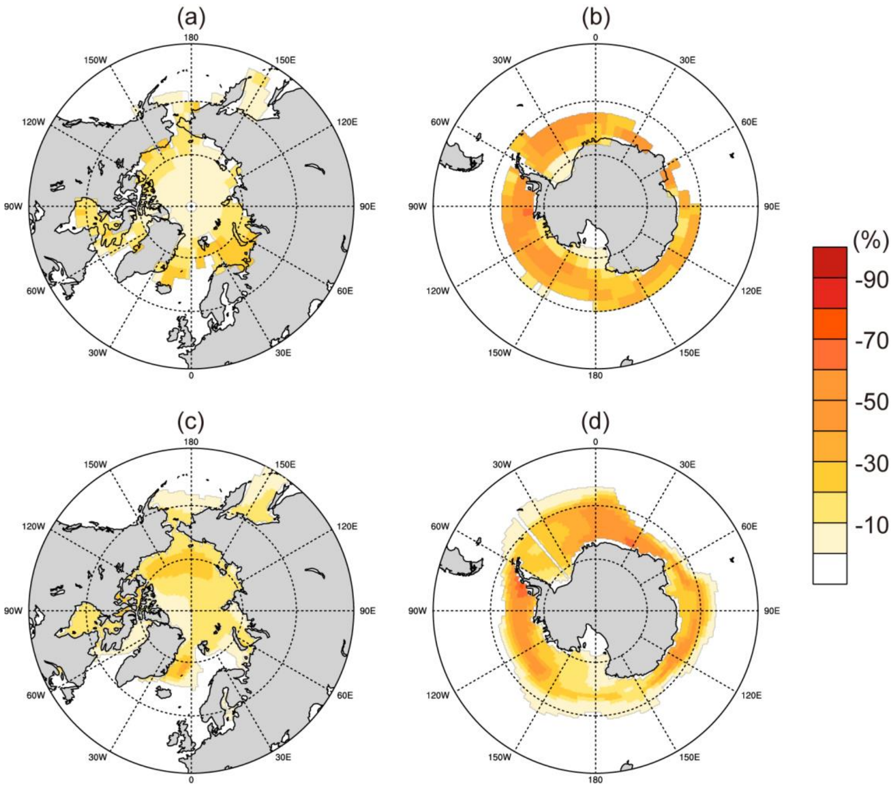

Figure 2.3 Comparison of the sea ice anomaly between the $2xCO_2$ and the PI simulations using LOVECLIM1.2 (a) in the Arctic and (b) in the Southern Ocean, and using CESM2 (c) in the Arctic and (d) in the Southern Ocean.

In addition to the 2xCO_2 experiment, to further investigate the sensitivity of sea ice in LOVECLIM, three experiments are also performed with only time-varied GHG concentrations under the Shared Socioeconomic Pathway (SSP)1-2.6, SSP2-4.5 and SSP5-8.5 scenarios from 2015 AD to 2100 AD, which represent the low, mid and high GHG emissions scenarios, respectively (IPCC, 2021). The last 5-year average climatology is compared with the model results from CMIP6. Figure 2.4 shows that under these three scenarios, the global, Arctic and Southern Ocean sea ice areas simulated by LOVECLIM1.2 all fall in the range of the multi-model results from CMIP6, which indicate that LOVECLIM has a reasonable sensitivity in simulating the global, Arctic and Southern Ocean sea ice.

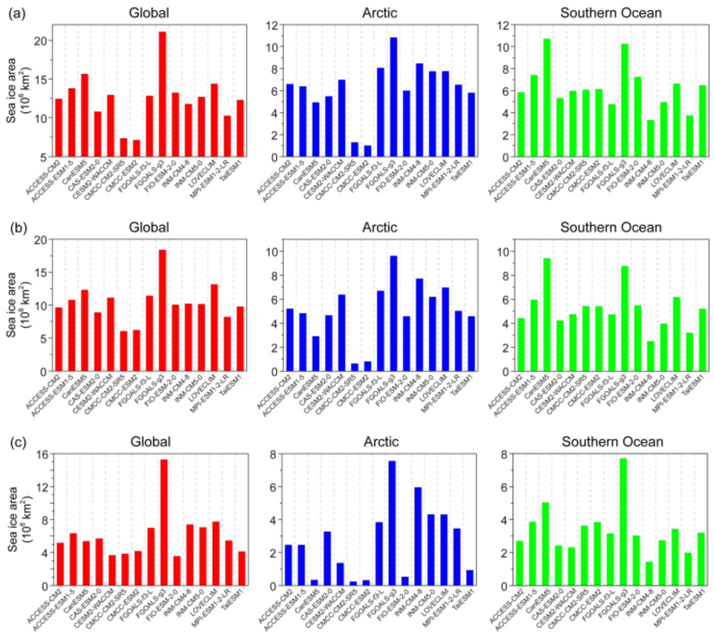

Figure 2.4 Sea ice area simulated by different models under the (a) low (SSP1-2.6), (b) mid (SSP2-4.5), and (c) high (SSP5-8.5) GHG emission scenario for global, Arctic (40°N-90°N) and Southern Ocean (40°S-90°S). These simulations are from 2015 AD to 2100 AD, and the last 5-year average climatology is analyzed. The data of LOVECLIM1.2 is from this study (only with varied GHG), and those of other models are from CMIP6 and the data link is: https://esgf-data.dkrz.de/search/cmip6-dkrz/.

2.2.2 The performance of LOVECLIM1.3 in simulating present-day climate

The performance of LOVECLIM1.2 in simulating present-day climate has been evaluated in detail in Goosse et al. (2010). Their results show that LOVECLIM1.2 has a good performance in simulating the climate at mid and high latitudes. For example, LOVECLIM1.2 can reasonably simulate the sea ice extent in both hemispheres, the surface temperature spatial distribution, the deep convection in the Greenland-Norwegian Sea and Labrador Sea. In addition, LOVECLIM1.2 can also reasonably simulate the main characteristics of large-scale climate changes, including the large-scale structure of the near-surface circulation and the magnitude of zonal mean precipitation at different latitudinal bands. Due to the relatively coarse resolution and the low level of complexity of some parameterizations, it also has some limitations. For instance, an overestimation of temperature at low latitudes, especially in the equatorial Eastern Pacific, and the temperature gradient between the Eastern and Western Pacific is too weak. Due to the relatively weak atmospheric circulation in LOVECLIM1.2, an overestimation of the Aleutian low and the simulated low-pressure center in the North Atlantic is located too far eastwards. In addition, the simulated zonal mean precipitation is too symmetric between the Northern and Southern hemispheres and the Intertropical Convergence Zone is not as well reproduced as in observation, and there is an overestimation of the vegetation cover in tropics. The sea ice concentration is slightly overestimated in the Southern Ocean in both summer and winter.

As compared to LOVECLIM1.2, some new or revised modules and some important mechanisms have been implemented in LOVECLIM1.3, for example, the representation of atmospheric dynamics in the tropics, the cloud feedbacks (these two both are contributed to Axel Timmermann) and the katabatic winds (Barthélemy et al., 2012). These have been shown to have reduced the model biases and improved the simulation of the present-day and past climate (Loutre et al., 2014). In order to evaluate the performance of

LOVECLIM1.3 in simulating present-day climate, a transient simulation over the past 2 ka (1-2000 AD) is performed following the protocol of the Paleoclimate Modeling Intercomparison Project Phase 4 (PMIP4) (Jungclaus et al., 2017), using the model LOVECLIM1.3 (L2M_PMIP4). The major forcings include the astronomical forcing, GHG, solar activity and aerosols from volcanic eruptions over the last 2 ka (Jungclaus et al., 2017). The last 20-year (1981-2000 AD) average climatology (surface temperature, sea surface temperature, precipitation and sea ice) is compared with the observations. For the observations, the surface temperature data is from the fifth generation European Centre for Medium-Range Weather Forecasts (ECMWF) reanalysis data (ERA5), and it covers the Earth on a 30 km grid and resolves the atmosphere using 137 levels from the surface up to a height of 80 km (https://cds.climate.copernicus.eu/cdsapp#!/search?text=ERA5, Bell et al., 2021). The precipitation data is from the Global Precipitation Climatology Project analysis data (GPCP), and its resolution is 2.5°×2.5° (144×72 grid points) (https://psl.noaa.gov/data/gridded/data.gpcp.html, Adler et al., 2018). Both the SST data and sea ice data are from the Hadley Centre Sea Ice and Sea Surface Temperature data set (HadISST), and their resolution are 1°×1° (360×180 grid points) (https://www.metoffice.gov.uk/hadobs/hadisst/, Titchner and Rayner, 2014).

As quite expected, LOVECLIM1.3 shares many fundamental similarities as LOVECLIM1.2. It simulates reasonably well the main characteristics of the present-day mean climate as compared with the observations. For example, the simulated annual mean and seasonal global temperature distribution, both surface temperature and sea surface temperature, have a good consistence with the observations (Figure 2.5 and Figure 2.6). The simulated precipitation spatial pattern and the magnitude of zonal mean precipitation at different latitudinal bands are very similar with the GPCP observation data (Figure 2.7). In addition, LOVECLIM1.3 simulates well the sea ice extent in both the Arctic and Southern Ocean as compared to the HadISST data (Figure

2.8). As compared to LOVECLIM1.2, some simulated results of the present-day climate are improved in LOVECLIM1.3. For example, the simulated Arctic and Southern Ocean sea ice concentration and sea ice extent in LOVECLIM1.3 are closer to the observations than in LOVECLIM1.2. The temperature biases in LOVECLIM1.3 are also smaller than in LOVECLIM1.2, especially in the tropics and Southern Ocean. However, LOVECLIM1.3 still have some limitations. Both the simulated annual mean and seasonal temperature over the Greenland and in the tropics are still warmer than the observations (Figure 2.5 and Figure 2.6). For the annual mean precipitation, the maximum rain belt in the tropics is a little moved southward in LOVECLIM1.3 as compared to the GPCP observation data, which is mainly due to their difference in NH winter (Figure 2.7). In addition, the simulated ENSO signal is very weak in LOVECLIM1.3 as compared to observation and the simulated results of CESM, due to its poor performance at low latitudes mainly related to its simple atmosphere component (Figure 2.9).

In addition to the present day, LOVECLIM can also reasonably simulate the climate changes during some past important periods as compared to the proxy records and other models. For example, LOVECLIM well simulated the warmer summer climate during the mid-Holocene than the present-day, and a large cooling of more than 25 °C over the Laurentide and Fennoscandian ice sheet regions during the last glacial maximum (Goosse et al., 2010). LOVECLIM also successfully simulated the sea ice variations in the central Okhotsk Sea over the past 130 ka that are dominated by precession, which have a good consistence with the sea ice reconstruction using the proxy IP25 (Lo et al., 2018). In addition, the abrupt climate changes at the end of the interglacials simulated by LOVECLIM1.3 have a good consistence with the marine sediments, ice cores and stalagmite records, and the results further show that these abrupt climate changes were triggered by the insolation threshold (Yin et al., 2021). At the peaks of the last nine interglacials, the Southern Ocean sea ice variations simulated by LOVECLIM are in line with the sea ice reconstructions using the ssNa from Antarctic ice core (Yin and

Berger, 2012). Probably due to its stronger polar amplification, the mid-high latitude temperature of the last interglacial simulated by LOVECLIM was closer to the reconstructions than many other GCMs (Berger and Yin, 2012; Lunt et al., 2013). Although LOVECLIM's performance in tropical regions is considered poor as mentioned above, it has been shown to well capture the response of the tropical and sub-tropical monsoons to changes in external forcing and boundary conditions. For example, LOVECLIM simulates a strong East Asian summer monsoon during MIS-13 under different external forcings (Yin et al., 2008, 2009), which is in agreement with many proxy records (Guo et al., 2009). The reinforcement of the East Asian summer monsoon by the Eurasian ice sheet and the related atmospheric wave pattern were confirmed by other more complex GCMs like HadCM3 (Muri et al., 2013).

The results above show that LOVECLIM can reasonably simulated the climate changes at mid-high latitude latitudes, such as the Arctic and Southern Ocean sea ice changes and the temperature changes. It also has a reasonable performance in simulating the long-term evolution of the regional average climate changes at different latitudinal bands, which as required in this thesis. Due to the relatively coarse resolution of LOVECLIM and its simple atmosphere component, the performance of LOVECLIM in low latitudes is relatively poor.

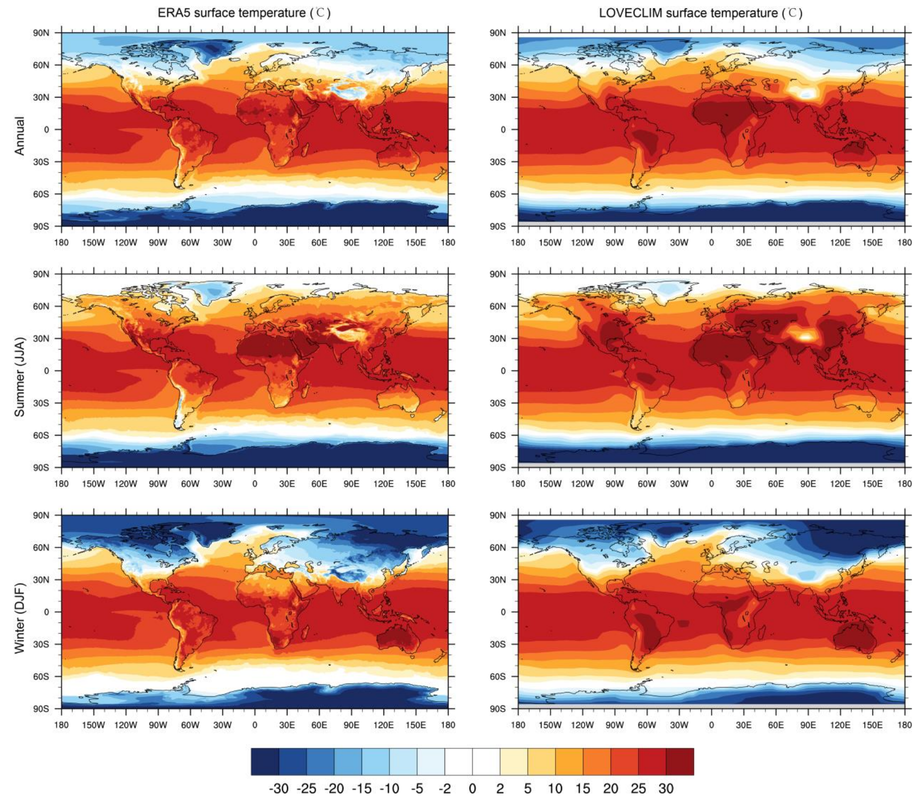

Figure 2.5 Comparison of the annual mean and seasonal surface temperature between the ERA5 reanalysis data and the LOVECLIM1.3 simulation.

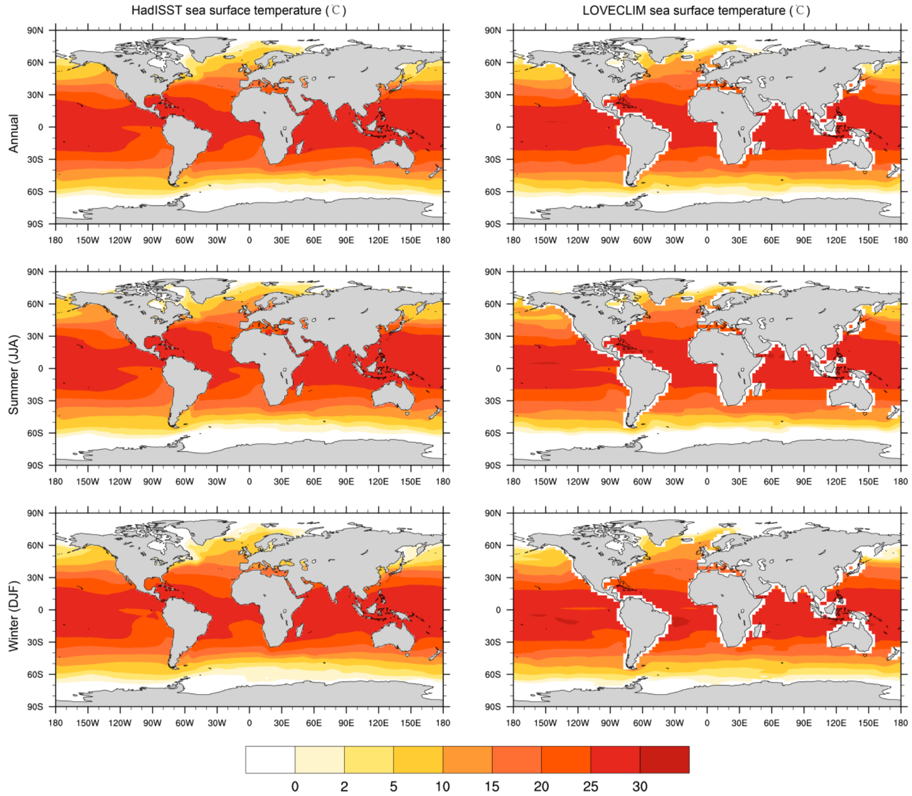

Figure 2.6 Comparison of the annual mean and seasonal sea surface temperature between the HadISST observation data and the LOVECLIM1.3 simulation.

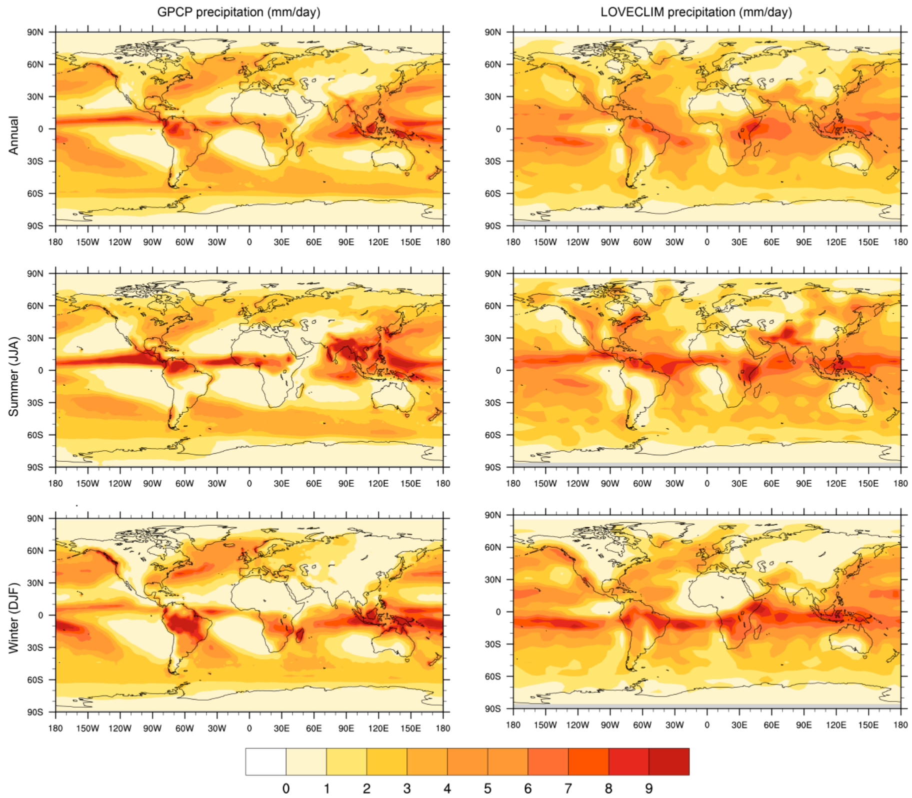

Figure 2.7 Comparison of the annual mean and seasonal precipitation between the GPCP observation data and the LOVECLIM1.3 simulation.

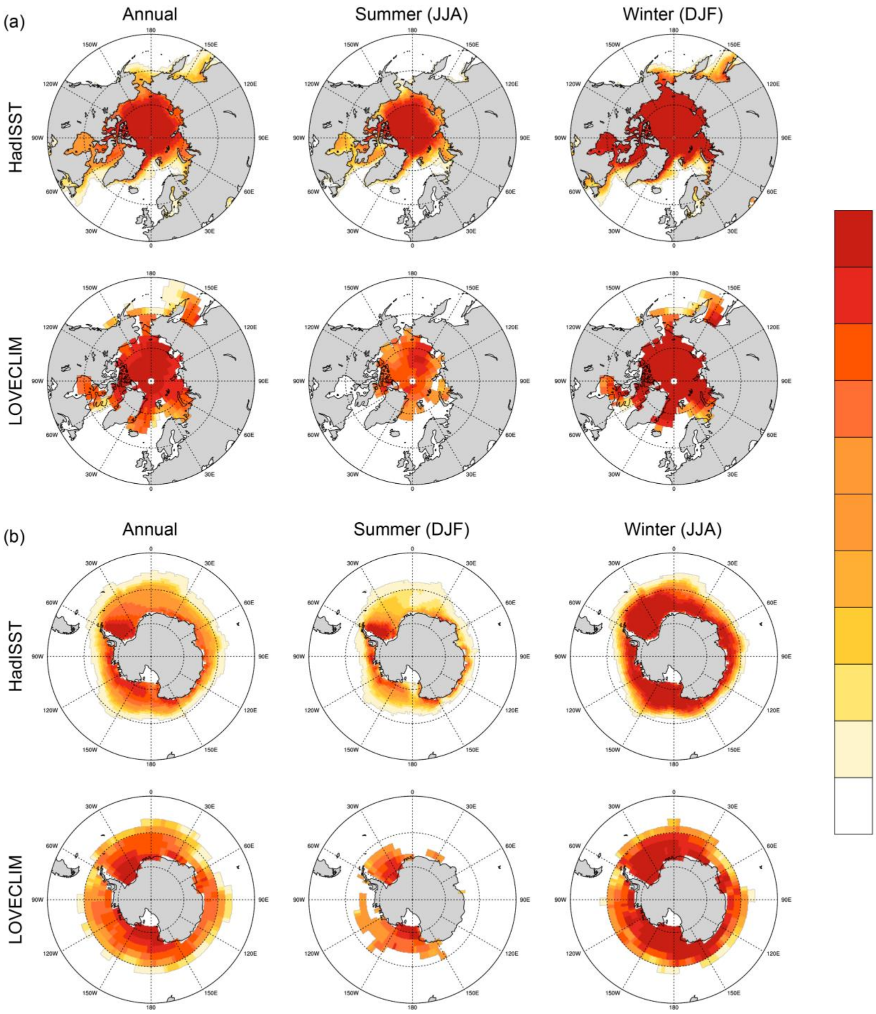

Figure 2.8 Comparison of the annual mean and seasonal Arctic (a) and Southern Ocean (b) sea ice between the HadISST observation data and the LOVECLIM1.3 simulation.

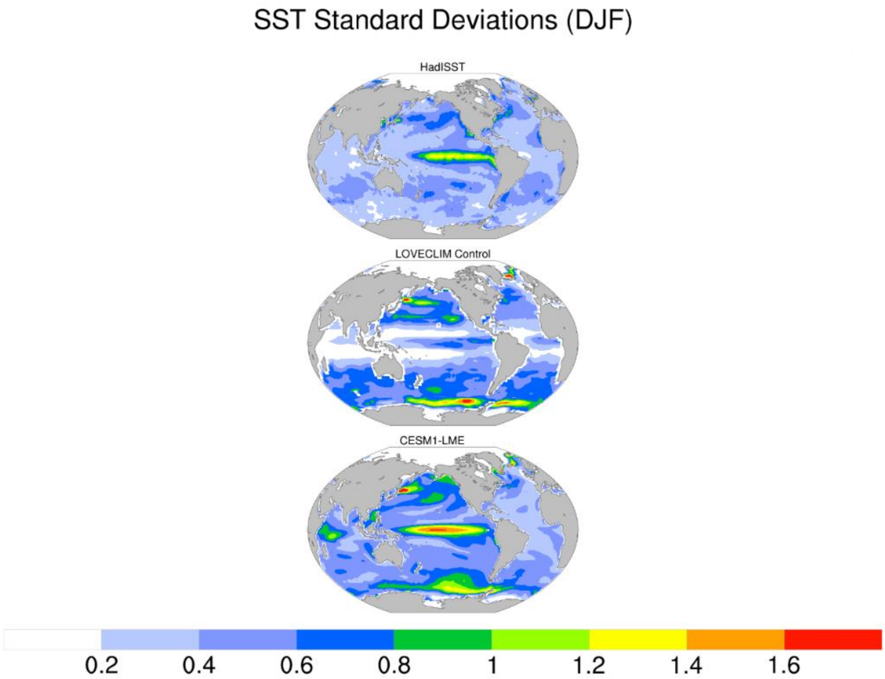

Figure 2.9 Standard deviations of winter (DJF) SST. From top to bottom: observation data (HadISST, Titchner and Rayner, 2014), simulated results of LOVECLIM1.3 and simulated results of CESM1-LME (Otto-Bliesner et al., 2016).

2.3 Experiments design and climate forcing

The experiments used in this thesis are summarized in Table 2.1.

2.3.1 Simulations with LOVECLIM1.2

Using the model LOVECLIM1.2, a more than 90,000-years transient simulation with only time-dependent insolation is first performed (T511_Orb in Table 2.1), to investigate the hemisphere differences in the response of sea surface temperature (SST) and sea ice to precession and obliquity (the results are presented in Chapter 3). The simulated time period is between 511 and 417 ka BP, a time interval corresponding to MIS-13, MIS-12 and the beginning of MIS-11. Covering four precessional cycles and two obliquity ones, it allows to investigate the impact of a large range of precession and obliquity. In order to investigate the impact of insolation alone, only astronomical parameters (Berger, 1978) vary in time (Figure 2.10). Constant GHG concentrations (CO_2 = 236 ppmv, CH_4 = 530 ppbv, N_2O = 265 ppbv) are used and the ice sheets are fixed to present-day condition. In order to avoid any possible influence of the acceleration technique, no acceleration is used in this simulation. The initial condition of the transient simulation is the equilibrium climate state of a 2000-year snapshot simulation performed with the astronomical parameters at 511 ka BP and the GHG concentrations same as the transient experiment. It is worth noting that this experiment is actually a sensitivity experiment and the GHG concentrations and ice sheets conditions do not correspond to the real conditions during MIS-13, MIS-12 and MIS-11. The GHG concentrations used here are the average values over 20,000 years between 511 to 491 ka BP, and are intermediate between a typical interglacial level (e.g. 280 ppmv) and a glacial level (e.g. 180 ppmv).

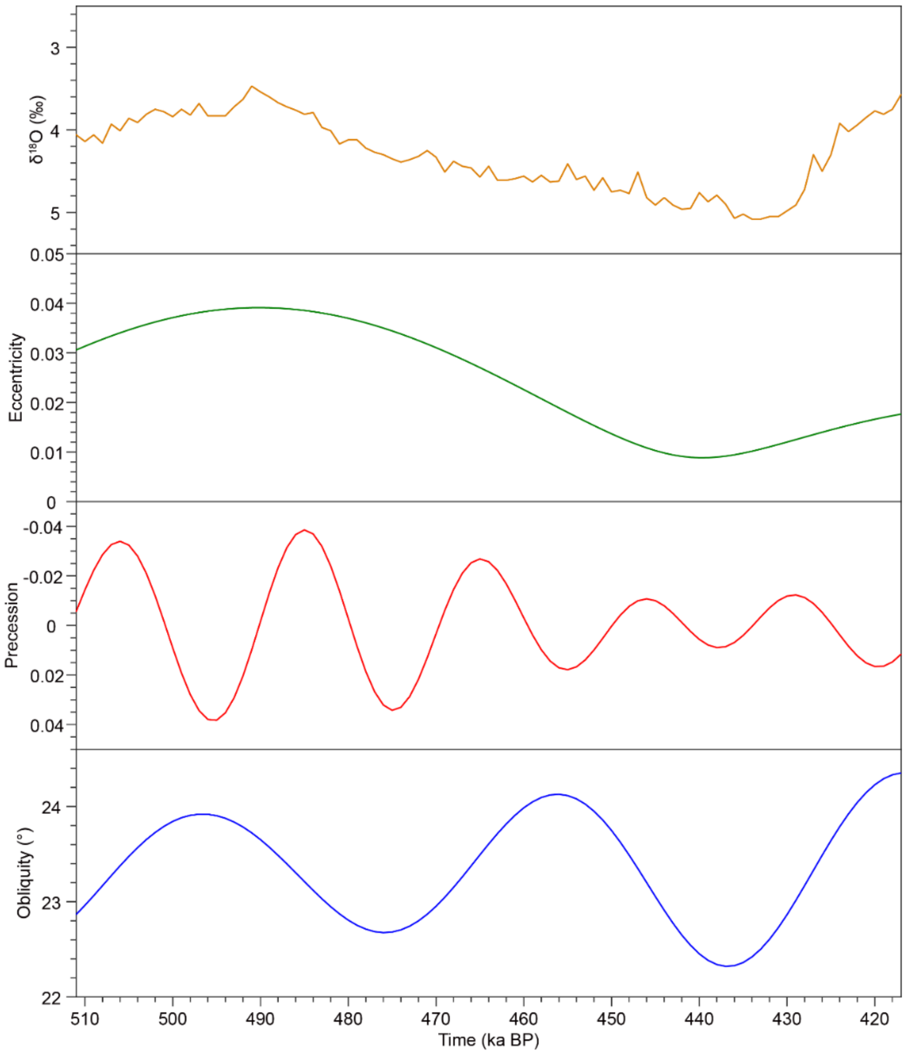

Figure 2.10 Benthic $\delta^{18}O$ (Lisiecki and Raymo, 2005), eccentricity, precession and obliquity (Berger, 1978) between 511 ka BP and 417 ka BP.

To investigate insolation and CO_2 induced variations in the Arctic and Southern Ocean sea ice during the last nine interglacials and their comparison with the present-day and future (Chapter 7), the nine control experiments (f11) performed in Yin and Berger (2012) are also used in this study. In these control experiments, both insolation and CO_2 are taken at their interglacial levels, and details of experiments setup have been given in Yin and Berger (2012), here I only describe it briefly. First, the benthic $\delta^{18}O$ stack (Lisiecki and Raymo, 2005) peaks of the interglacials were selected. Then, the values of the astronomical parameters (Berger, 1978) at the dates when NH summer occurs at perihelion just preceding the $\delta^{18}O$ peaks were taken based on the hypothesis that the maximum insolation in the NH summer controls the interglacials (Kukla et al., 1981). However, there are two exceptions: NH summer at perihelion occurs 3 ka later than the $\delta^{18}O$ peak during MIS-17 and the peak selected is at 501 ka BP rather than at 491 ka BP in the $\delta^{18}O$ stack (Lisiecki and Raymo, 2005) during MIS-13.1. Finally, the GHG concentrations at the dates of the CO_2 peaks just preceding the $\delta^{18}O$ peaks were taken in order to maximize the climate response. The details of the dates and values of the astronomical parameters and GHG concentrations at these nine interglacials can be found in Table 1 of Yin and Berger (2012).

Three new experiments are also performed using LOVECLIM1.2 in this study to represent the present and future climate, in order to compare them with the interglacials (Chapter 7). Two experiments are used to represent the present climate: one is the pre-industrial experiment (hereafter abbreviated as PI experiment) which could be considered as the present-day climate under the natural climate variability, its astronomical parameters are taken the values at 0 ka (Berger 1978), CO_2 = 280 ppmv, CH_4 = 760 ppbv, and N_2O = 270 ppbv; the other is a transient simulation from 1500 AD to 2000 AD in which the effect of the anthropogenic forcing is also included, and the last 30-year average climatology is analyzed (hereafter abbreviated as PD experiment). The CO_2 concentration is increased with time in the PD experiment, and the last 30-year average CO_2 concentration is 66 ppmv higher than the PI one (346 vs. 280 ppmv). For the future climate, the CO_2 concentration projected at the end of the 21th century is most likely much higher with the largest probability between 446 and 1135 ppmv (IPCC, 2021) and as a nearly ice-free Arctic Ocean in the summer sea ice minimum is projected near mid-century under mid and high GHG emissions scenarios (IPCC, 2021), it would be interesting to see if sea ice conditions similar to projected for the future happened during the interglacials. The double CO_2 experiment (CO_2 doubled as compared to the PI) was early used to discuss the global warming with increased atmospheric CO_2 concentration in the future (Manabe and Wetherald, 1967), and now has become a standard and classic experiment in climate science (Manabe and Wetherald, 1967; Myhre et al., 2017), and this CO_2 concentration being very close to the mid GHG emissions scenarios (IPCC, 2021). In this study, a double CO_2 experiment is also performed to represent the future (hereafter abbreviated as $2xCO_2$ experiment).

2.3.2 Simulations with LOVECLIM1.3

Using the latest version LOVECLIM1.3, three sets of transient simulations with no acceleration are performed for the nine glacial-interglacial periods over the past 800 ka. The model setup is the same as the one used in Yin et al. (2021). Each simulation period is centered on an interglacial and covers also part of the transitions of the glacial termination and inception before and after each interglacial. To be simple, hereafter we use Marine Isotope Stage (MIS)-1, -5, -7, -9, -11, -13, -15, -17 and -19 to represent these nine simulated time periods. The simulation periods are 17-0 ka BP for MIS-1, 133-75 ka BP for MIS-5, 247-192 ka BP for MIS-7, 340-282 ka BP for MIS-9, 424-382 ka BP for MIS-11, 538-471 ka BP for MIS-13, 627-564 ka BP for MIS-15, 719-679 ka BP for MIS-17 and 794-766 ka BP for MIS-19 (Figure 2.11). This leads to large amplitude variations of both CO_2 and ice sheets. For example, the CO_2 concentration varied between 180 ppmv and 290 ppmv (Lüthi et al., 2008), and the NH ice volume varied between 4 million km^3 and 40 million km^3 (Ganopolski and Calov, 2011). These nine periods also cover a wide range of astronomical forcing. They include high and low values of eccentricity which lead to large and small amplitude variations of precession, and they also include large and small amplitude variations of obliquity (Berger and Loutre, 1991). In addition, they include both situations where precession minimum and obliquity maximum are in-phase and anti-phase, which could be critical for the climate system (Yin and Berger, 2010, 2015). In terms of the half-precession cycle, all of the simulation periods cover more than one half-precession cycle, and seven of them cover more than four half-precession cycles. Therefore, the last nine interglacials over the past 800 ka are suitable to investigate the response of different climatic variables at different regions to astronomical parameters, CO_2 and NH ice sheets between the two hemispheres, as well as the half-precession signals.

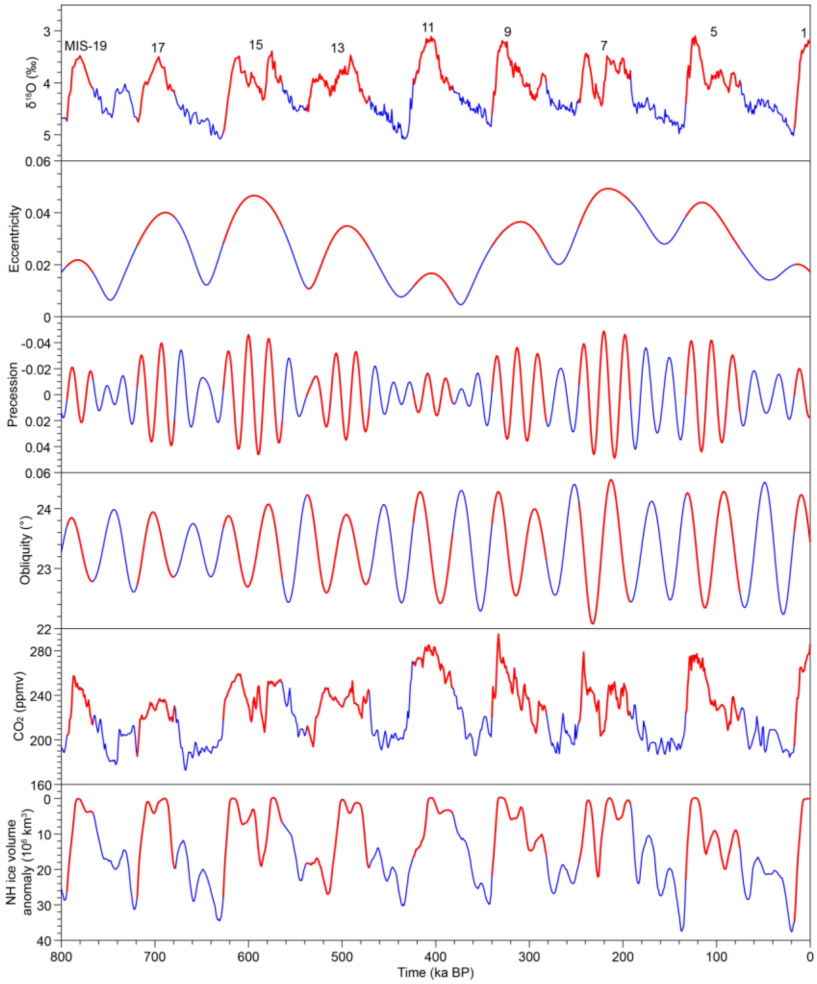

Figure 2.11 Benthic $\delta^{18}O$ (Lisiecki and Raymo, 2005), eccentricity, precession and obliquity (Berger and Loutre, 1991), CO_2 concentrations (Lüthi et al., 2008) and NH ice volume anomaly as compared to pre-industrial (Ganopolski and Calov, 2011) over the past 800 ka. The numbers of MIS stages are indicated, and the red lines indicate the time periods of simulations performed in this thesis.

In the first set of simulations, only astronomical parameters (Berger and Loutre, 1991) vary with time (hereafter they are referred as Orb experiments), the GHG concentrations and ice sheets being fixed at the pre-industrial values. The initial conditions are provided by a 2000-year equilibrium experiment with the astronomical parameters at the starting date of the simulated period and the pre-industrial GHG concentrations and ice sheets. In the second set of simulations, both the GHG concentrations (Lüthi et al., 2008; Loulergue et al., 2008; Schilt et al., 2010) and astronomical parameters vary with time (hereafter they are referred as OrbGHG experiments), the ice sheets being fixed at the pre-industrial values. The initial conditions are provided by a 2000-year equilibrium experiment with the astronomical parameters and GHG concentrations at the starting date of the simulated period and the pre-industrial ice sheets. The GHG concentrations are reconstructed from the Antarctic ice core (Lüthi et al., 2008; Loulergue et al., 2008; Schilt et al., 2010), and they are linearly interpolated to one-year resolution and used in this study. Detailed description of these two sets of simulations can also be found in Yin et al. (2021). In the third set of simulations, the NH ice sheets (Ganopolski and Calov, 2011), GHG concentrations and astronomical parameters all vary with time (hereafter they are referred as OrbGHGICE experiments), the Antarctic ice sheet being fixed at the pre-industrial condition. The initial conditions are provided by a 2000-year equilibrium experiment with the NH ice sheets, GHG concentrations and astronomical parameters at the starting date of the simulated period.

In the presence of land ice, albedo, topography, vegetation and surface soil types corresponding to ice-covered condition were prescribed at corresponding model grids in LOVECLIM1.3. The ice sheet data is from the simulated results of Ganopolski and Calov (2011) and interpolated to LOVECLIM grid, and it is updated every one thousand years. In addition, the status of the Hudson Bay (closed or open) is changed based on the extent of the North American ice sheet. If the extent of the North American ice sheet over the Hudson Bay is more than a half, the Hudson Bay is changed to closed, otherwise it keeps open. Moreover, if the North American ice sheet is large and the Hudson Bay is closed, the prescribed river routes were disrupted. For the changes of the river routes over North America, we follow the protocol for Last Glacial Maximum (LGM) experiments in the Paleoclimate Modelling Intercomparison Project-Phase 4 (PMIP4) (Kageyama et al., 2017). For instance, the river runoff that previously entered into the Hudson Bay was consequently rerouted, partly northward entering into the Arctic Ocean and partly southward entering into the Atlantic.

As discussed above, the status of the Hudson Bay (closed or open) is changed due to the advance and retreat of the North American ice sheet. In order to investigate the effect of the Hudson Bay closure on global and regional climate under different background climate conditions (Chapter 4), a pair of sensitivity experiments were performed at the initial date of each simulation period shown in Figure 2.11. At these dates, the North American ice sheet was sufficiently large to cover completely the Hudson Bay, and there are large variations in the astronomical parameters, GHG concentrations and NH ice volume. For example, obliquity ranges from 24.2º at 538 ka BP to 22.7º at 719 ka BP, precession ranges from 0.00409 at 794 ka BP to -0.00735 at 247 ka BP (Berger and Loutre, 1991), and the CO_2 equivalent (CO_{2eq}, which is calculated based on the formula in https://gml.noaa.gov/aggi/aggi.html) ranges from 267 ppmv at 424 ka BP to 171 ppmv at 719 ka BP (Luthi et al., 2008; Loulergue et al., 2008; Schilt et al., 2010). In addition, the total NH ice volume ranges from 39 million km^3 at 17 ka BP to 21 million km^3 at 424 ka BP (Ganopolski and Calov, 2011). Therefore, these experiments allow to explore the effect of the Hudson Bay closure on global and regional climate under different background climate conditions.

At each date (and each pair), the astronomical parameters (Berger and Loutre, 1991), GHG concentrations (Luthi et al., 2008; Loulergue et al., 2008; Schilt et al., 2010) and the NH ice sheet configurations (Ganopolski and Calov, 2011) are taken at the values of this date for both experiments in each pair, the Antarctic ice sheet being kept the same as the pre-industrial one. Within each pair of experiments, the Hudson Bay is open in one experiment and is closed in another one (hereafter they are referred as OHB and CHB respectively). In the OHB experiments, the ocean-land mask was kept the same as the present-day one (Figure 2.12a), while the ocean over the Hudson Bay was changed to land in the CHB experiments (Figure 2.12b). Actually, the nine CHB experiments are the initial conditions of the nine transient OrbGHGICE experiments discussed above. As land ice covers only land grids in LOVECLIM1.3, the Hudson Bay was covered by land ice in the CHB experiments, while it was still kept as ocean in the OHB experiments. Figure 2.13 gives an example of the NH topography anomaly at 133 ka BP and 424 ka BP relative to the pre-industrial conditions in the OHB and CHB experiments.

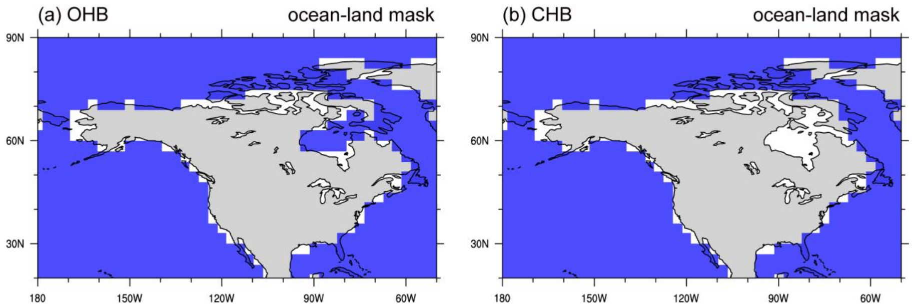

Figure 2.12 The ocean-land mask over North America in the OHB (a) and CHB (b) experiments.

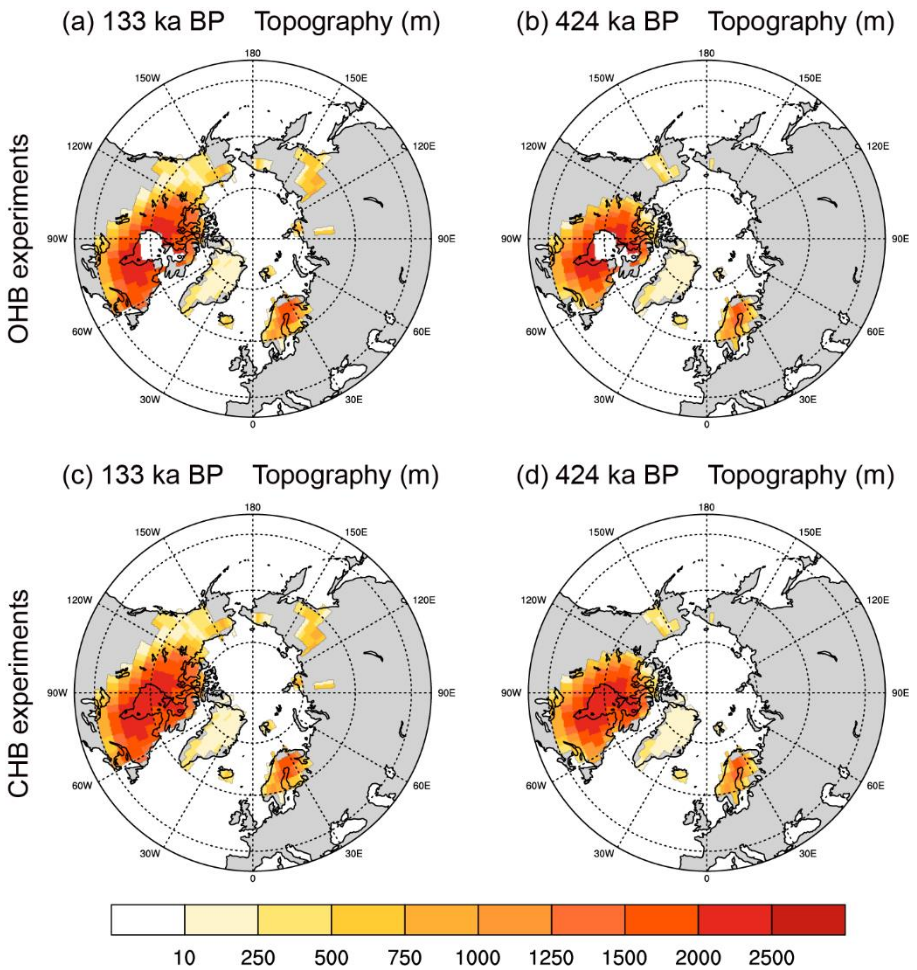

Figure 2.13 Topography anomaly (m) at 133 ka BP and 424 ka BP relative to the pre-industrial conditions in the OHB and CHB experiments. The ice sheet data is from the simulated results of Ganopolski and Calov (2011) and interpolated to LOVECLIM grid.

All the 18 experiments were run for 2000 years to reach equilibrium, and the last 100-year average climatology was analyzed. In addition, in order to compare the effect of the Hudson Bay closure with the effect of the NH ice sheets, the snapshot experiments with the present-day ice sheets but the insolation and GHG at 133 ka BP and 424 ka BP are also analyzed. The difference between the CHB and OHB experiments gives the impact of the Hudson Bay closure, and the difference between the OHB and OG experiments gives the impact of the NH ice sheets (Chapter 4).

Table 2.1 A summary of all the experiments used in this thesis. For the simulations of past time periods, GHG concentrations (Lüthi et al., 2008; Loulergue et al., 2008; Schilt et al., 2010) and NH ice volume (Ganopolski and Calov, 2011) are used, and astronomical parameters of Berger (1978) are used in LOVECLIM1.2 and astronomical parameters of Berger and Loutre (1991) are used in LOVECLIM1.3. For the L2M_PMIP4 experiment, the forcing data is from Kageyama et al. (2018). For the SSP experiments, the GHG data is from O'Neill et al. (2016). For the insolation, GHG, NH ice sheets and Hudson Bay status, √ represents the true values are used in these experiments, otherwise they are fixed at the PI condition.

Experiment name	Model	Type	Insolation	GHG	NH ice sheets	Hudson Bay	Used in	Reference
PI	LOVECLIM1.2	Snapshot					Chapter 2, 7	Wu et al., 2022
Double_CO2				√				
F11_MIS-1 (5.5, 7.5, 9.3, 11.3, 13.13, 15.1, 17, 19)			√	√			Chapter 7	Yin and Berger, 2012
I17 (133, 247, 340, 424, 538, 627, 719, 794)_Orb	LOVECLIM1.3		√				Chapter 5, 6	Yin et al., 2021
I17 (133, 247, 340, 424, 538, 627, 719, 794)_OrbGHG			√	√				
I17 (133, 247, 340, 424, 538, 627, 719, 794)_CHB			√	√	√	√	Chapter 4, 5, 6	Wu et al., 2023
I17 (133, 247, 340, 424, 538, 627, 719, 794)_OHB			√	√	√		Chapter 4	
PD	LOVECLIM1.2	Transient	√	√			Chapter 2, 7	Wu et al., 2022
SSP1-2.6 (2-4.5, 5-8.5)			√	√			Chapter 2	
T511_Orb			√	√			Chapter 3	Wu et al., 2020
L2M_PMIP4	LOVECLIM1.3		√	√			Chapter 2	This thesis
T17 (133, 247, 340, 424, 538, 627, 719, 794)_Orb			√				Chapter 5, 6	Yin et al., 2021
T17 (133, 247, 340, 424, 538, 627, 719, 794)_OrbGHG			√	√				
T17 (133, 247, 340, 424, 538, 627, 719, 794)_OrbGHGICE			√	√	√	√		This thesis

Chapter 3 Hemisphere differences in response of sea surface temperature and sea ice to precession and obliquity[1]

3.1 Introduction

As one of the most important drivers of the climate system, the incoming solar radiation (insolation), depends on the three astronomical parameters: eccentricity, obliquity and climatic precession (Berger, 1976, 1978). The total energy received by the whole Earth over one year is only a function of eccentricity, while obliquity and precession can modify the latitudinal-seasonal distribution of insolation (Berger, 1988; Loutre et al., 2004; Berger et al., 2010). The astronomical signals related to these three parameters have been found in plenty of geological records like deep-sea sediments, continental archives and ice cores.

The relationship between different climatic variables and the astronomical parameters has long been a center topic in paleoclimate study. For example, the relationship between SST and the astronomical parameters have been discussed based on marine records from the Pacific (e.g. de Garidel-Thoron et al., 2005), Atlantic (e.g. Lawrence et al., 2009) and Indian Ocean (e.g. Howard and Prell, 1992). The response of other climatic variables to astronomical forcing have also been discussed, like sea ice (e.g. Cronin et al., 2013), vegetation (e.g. Joannin et al., 2011; Goñi et al., 2016; Oliveira et al., 2018) and the Asian monsoon (e.g. Cheng et al., 2016). Climate model simulations have also been used to understand the response of the climate system to the astronomical forcing. For example, Earth system

[1] This chapter is published in Wu Z.P., Yin Q.Z., Guo Z.T., Berger A., 2020. Hemisphere differences in response of sea surface temperature and sea ice to precession and obliquity. Global and Planetary Change, 192, 103223.

models of intermediate complexity (EMICs), such as CLIMBER (Ganopolski and Calov, 2011) and GENIE (Holden et al., 2011), have been used to perform long transient simulations to study the climate response to astronomical parameters, GHG and NH ice sheets over many glacial-interglacial cycles. More complex atmosphere-ocean general circulations models, such as HadCM3 (Singarayer et al., 2011), have been used to perform snapshot experiments to study the response of one or more components of the climate system to changes in insolation. Both proxy and modelling studies show that the climate response to the astronomical forcing depends strongly on regions and on different climatic variables.

On hemisphere scales, evidence from both paleoclimate records and simulations shows that the two hemispheres seem to respond differently to obliquity and precession. For the sea ice, Lo et al. (2018) found that the autumn sea ice extent was governed by insolation and showed strong precession cycles when the atmospheric CO_2 concentrations ranging from 190 to 260 ppmv during the last 130 ka in the central Okhotsk Sea. Cronin et al. (2013) reconstructed the sea ice extent during the last 600 ka in western Arctic Ocean and found that the sea ice varied mainly at precessional and obliquity frequencies with precession playing a more important role. In the Southern Ocean, Wolff et al. (2006) reconstructed winter sea ice extent using the ssNa flux over the past eight glacial cycles, and found that its variation was dominated by periodicities on time scales of 80-120 ka although the obliquity and precessional components can also be found. For SST, the reconstructed results also show an obvious difference between the NH and SH. Besides the 100 ka periodicity, the SST reconstructions show a clear obliquity signal in both hemispheres, but the precessional signal is much stronger in the NH than in the SH (Martrat et al., 2007; Bard and Rickaby, 2009). Based on snapshot and 10-times accelerated transient simulations, Yin and Berger (2012, 2015) found that in general the NH climate responds more to precession whereas the SH responds more to obliquity, but in-depth analysis on internal processes and feedbacks are still needed. In addition, Timmermann et al. (2014) investigated the response of the SH climate to obliquity and CO_2 using a series of snapshot simulations and a 5-times accelerated transient simulation. They found that the SH westerlies were mainly controlled by the obliquity cycle and the temperature changes in Antarctica were determined by the combined effect of shortwave obliquity forcing, GHG forcing, and meridional heat transport.

In spite of many existing studies, the different response of the climate system to obliquity and precession between the two hemispheres is still not very clear. This is mainly due to: (1) in the geological records, it is not straightforward to distinguish the impact of the astronomical parameters from the other forcings, like GHG and ice sheets, because they can contain the same periodicities; and (2) the numerical simulations, which focus on understanding the response of the climate system to obliquity and precession and especially the differences between the two hemispheres, are still scarce. Thus, there is a need to investigate the response of the different climatic variables to obliquity and precession using long and continuous transient simulations.

Here we focus on understanding the relative importance of precession and obliquity on two important components in the climate system, sea ice and sea surface temperature, in both hemispheres as well as the internal processes and feedbacks involved to explain the differences between the two hemispheres. The study of this Chapter is based on a transient simulation using the model LOVECLIM1.2 (T511_Orb, see Chapter 2). Although LOVECLIM is classified as an Earth system model of intermediate complexity, its complexity is on the top of this kind of models and thus it cannot be used easily to run a transient simulation spanning several glacial cycles. Therefore, in our study, we choose the time interval between 511 and 417 ka BP which covers the interglacial peak of MIS-13, the glacial MIS-12 and the beginning of MIS-11. There are three reasons to choose this period. First, this period includes relatively high and low values of eccentricity which leads to both large and small amplitude of variations in precession and therefore in daily insolation. In particular, it covers MIS-11 with near-zero eccentricity that has been considered as an astronomical analogue of our present-day interglacial (Loutre and Berger, 2003). Second, this period includes both situations where precession minima and obliquity maxima are in-phase and are anti-phase (Figure 3.1) (the phase relationship between precession and obliquity could be critical for the climate system (Yin and Berger, 2010, 2015)). Third, this period covers the Mid-Brunhes Transition or Event (MBT or MBE) that is characterized by relatively warmer interglacials after about 430 ka BP than before (e.g. Jansen et al.,1986; Jouzel et al., 2007). The causes proposed to explain the MBE includes for example astronomical forcing (Pisias and Rea, 1988; Yin, 2013) and a major ice-sheet expansion during MIS-12 (Bard and Rickaby, 2009). In this study, we don't intend to investigate the MBE, but our results and simulation might be useful for other studies working on this topic.

3.2 The response of sea ice to precession and obliquity

Figure 3.1 shows clearly that the responses of the Arctic and Southern Ocean sea ice to the astronomical forcing are different. In the Arctic, the variation of the annual mean sea ice is highly correlated with precession, while in the Southern Ocean, it is highly correlated with obliquity. In order to quantify the relative weight of each astronomical parameter on the sea ice variations, multiple linear regression analyses (using the standardized values of the variables) are performed. The results (Table 1) show that precession plays a dominant role on the Arctic sea ice and the importance of obliquity is also obvious, but obliquity is more important for the Southern Ocean sea ice. Our results on the Arctic sea ice is in line with the finding of Lo et al. (2018) where both proxy records and numerical simulations show that the sea ice in the central Okhotsk sea during the last 130,000 years is mainly governed by precession-dominated insolation changes when the atmospheric CO_2 concentrations range from 190 to 260 ppmv. Cronin et al. (2013) also indicate that the sea ice in western Arctic Ocean during the last 600 ka varied primarily at precessional and obliquity frequencies, and precession plays a dominant role. As CO_2 and ice sheets are fixed in our simulation, it is impossible for us to discuss about the 100 ka cycle that might be strongly related to these forcings (Clark et al., 1999). However, the Southern Ocean sea ice reconstruction of Wolff et al. (2006) shows a dominant 80-120 ka cycle. This indicates that other forcings than insolation, such as GHG and ice sheets, must have a major influence on the Southern Ocean sea ice. Indeed, Yin and Berger (2012) show that GHG plays a dominant role in the SH whereas insolation is more important in the NH.

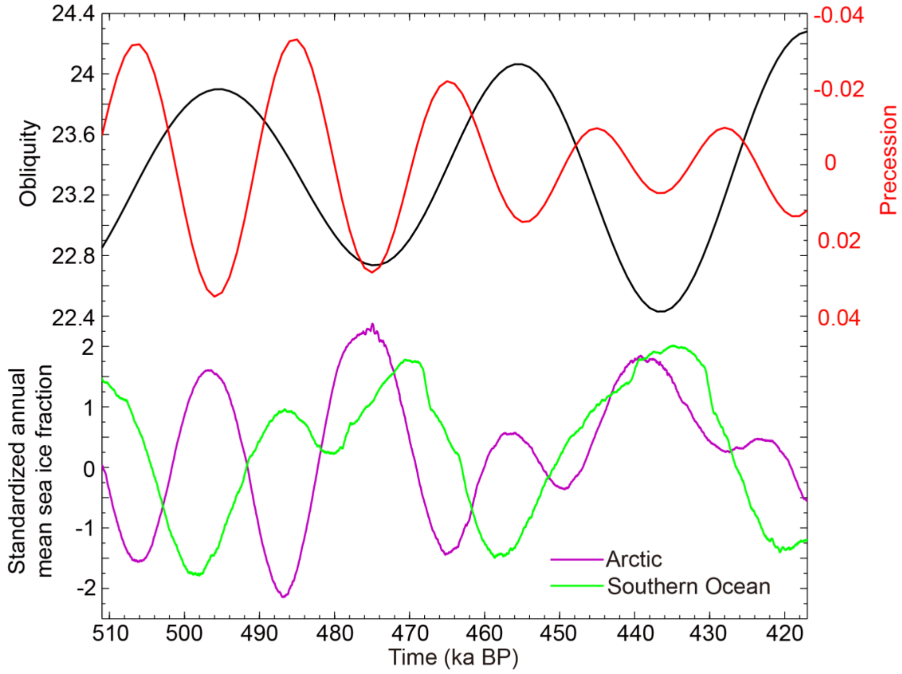

Figure 3.1 Comparison of the simulated annual mean Arctic and Southern Ocean sea ice fraction with obliquity and precession. A 1000-year running mean is performed on the curves of the Arctic and Southern Ocean sea ice fraction to reduce the high-frequency fluctuations.

Table 3.1 Regression coefficients of a linear multiple regression between the insolation-induced climatic variables (the predictand) and E (eccentricity), O (obliquity) and P (precession) (the predictors). The calculation is based on the data of the whole simulation period between 511 and 417 ka BP. The variables are annual mean sea ice fraction and sea surface temperature. All the values have been standardized to have the regression coefficients representing comparable weights of the predictors on the predictand.

	sea ice fraction		sea surface temperature (SST)						
	Arctic	Southern Ocean	60°S-90°S	30°S-60°S	10°S-30°S	10°S-10°N	10°N-30°N	30°N-60°N	60°N-90°N
R^2	0.77	0.67	0.86	0.90	0.40	0.12	0.32	0.68	0.74
E	-0.15	-0.14	0.10	0.11	0.15	0.06	0.05	-0.07	-0.04
O	-0.45	-0.72	0.91	0.93	0.38	-0.16	0.20	0.75	0.65
P	0.78	-0.24	-0.02	-0.19	-0.51	-0.29	-0.55	-0.50	-0.68

Our simulation period contains a period of high amplitude variation of precession (511-460 ka BP) and a period of low amplitude variation of precession (460-417 ka BP). We might expect a dominant role of obliquity when the variation of precession is small, as shown in Yin and Berger (2015) for MIS-11. Therefore, we also performed separately linear multiple regression analyses for 511-460 ka BP and for 460-417 ka BP. The results of 511-460 ka BP are very similar to those obtained from the whole time period (see supplementary Table S3.1), but the results of 460-417 ka BP (Table S3.2) show that obliquity is more important than precession in both the Arctic and Southern Ocean sea ice, which is quite expected from the low amplitude variation of precession. However, obliquity still plays more important role in the SH than in the NH and precession is more important in the NH than SH even in the latter case.

To better understand the different response of the Arctic and Southern Ocean sea ice to precession and obliquity, and related internal processes and feedbacks, the seasonal variations of the Arctic and Southern Ocean sea ice are also analyzed (Figure 3.2). In the Arctic, the amplitude of the sea ice variation is much larger in summer than in other seasons (Figure 3.2a), this is in line with the results of snapshot simulations of the last nine interglacials (Yin and Berger, 2012) and the observation records over the last 30 years (Titchner and Rayner, 2014). This can also be observed by comparing the seasonal geographical distributions of sea ice fraction between a precession maximum (e.g. 496 ka BP) and a precession minimum (e.g. 486 ka BP) (Figure S3.1 and Figure S3.2). The variation of the annual mean sea ice is therefore dominated by the variation of the summer sea ice, which is mainly controlled by local summer insolation that in turn is mainly a function of precession. When climatic precession is low (NH summer at perihelion), the local summer insolation is high, leading to low sea ice fraction (Figure 3.3, left). In addition, the Arctic sea ice is also influenced, but to a lesser degree, by the northward oceanic heat transports across 60°N (Goosse and Renssen, 2001) which is also dominated by precession (not shown). However, the local summer insolation also contains obvious obliquity signal, a smaller obliquity directly leading to lower summer insolation and finally to a cooling and more sea ice formation, which could explain why obliquity is also present in the Arctic sea ice (Table 3.1). In the Southern Ocean, the difference in the magnitude of sea ice variations between the four seasons is smaller than in the Arctic, but the amplitude is still the largest in local summer (Figure 3.2b, Figure S3.1 and Figure S3.2). The annual mean sea ice variation is more equally influenced by the variations of the sea ice of the four seasons when compared to Arctic. Different from the summer sea ice variation in the Arctic, the variation of the summer sea ice in the Southern Ocean shows a very strong obliquity signal. These explain why obliquity is more important for the sea ice in the Southern Ocean than in the Arctic. A smaller obliquity directly leads to lower insolation at high latitudes and finally to a cooling and more sea ice formation (Figure 3.3, right), and vice versa. In addition, obliquity could also influence the Southern Ocean sea ice through its influence on the westerlies. Our results (Figure 3.3, right) show that a smaller obliquity leads to larger latitudinal temperature and pressure gradients, and finally to stronger westerly winds. In line with Timmermann et al. (2014), in our simulation the SH westerlies are mainly influenced by obliquity. The strong obliquity signal in the SH westerlies could also help to explain the obliquity signal in the Southern Ocean sea ice. The formation of the Southern Ocean sea ice may also be influenced by the southward oceanic heat transports across 60°S that is dominated by precession (not shown). This might partly explain why there is a weak precessional signal in the annual mean Southern Ocean sea ice (Table 3.1). This agrees with the geological evidence that the Southern Ocean sea ice variation also contains precession periodicity (Wolff et al., 2006).

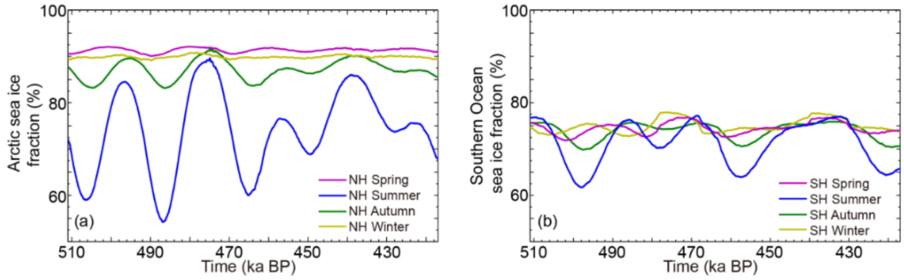

Figure 3.2 The seasonal variations of the sea ice fraction in the (a) Arctic and (b) Southern Ocean. A 1000-year running mean is performed on the curves to reduce the high-frequency fluctuations.

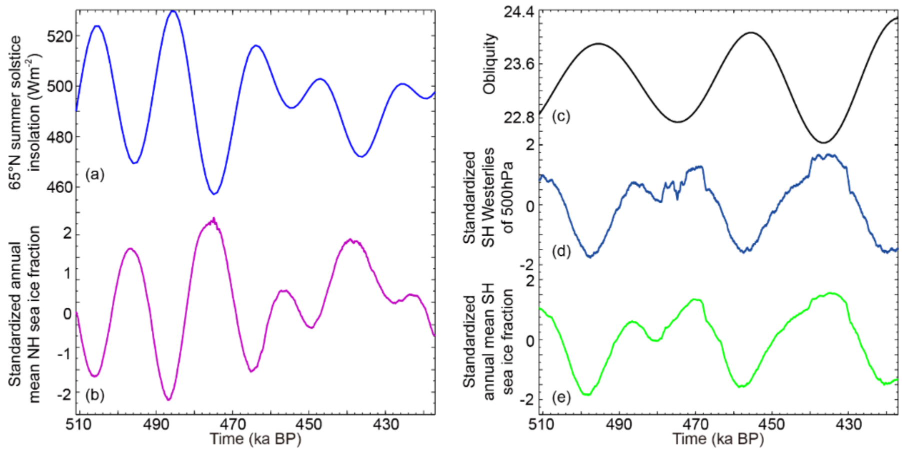

Figure 3.3 The forcing mechanisms for the annual mean Arctic (left) and Southern Ocean sea ice (right). (a) 65°N summer solstice insolation (Berger, 1978), (b) standardized annual mean Arctic sea ice fraction, (c) obliquity (Berger, 1978), (d) standardized SH westerlies of 500hPa, (e) standardized annual mean Southern Ocean sea ice fraction. A 1000-year running mean is performed on the curves of (b), (d), and (e) to reduce the high-frequency fluctuations.

The key internal processes responsible for the response of sea ice to precession and obliquity lie in the relationships between the surface energy budget (surface solar radiation – surface thermal radiation + surface sensible heat flux + surface latent heat flux), SST and sea ice. The surface energy budget is dominated by the surface shortwave radiation. Figure 3.4 shows that the surface energy budget (40°N-90°N and 40°S-90°S) is directly related to the SST (40°N-90°N and 40°S-90°S) which in turn influence the sea ice: when the surface energy budget is high, SST is high, leading finally to less sea ice, for a relationship which happens in both hemispheres (but the sea ice could also influence the SST, a feedback which will be discussed below). The surface energy budget is directly and strongly influenced by precession and obliquity: linear multiple regression analyses (Table 3.2) show that obliquity plays a dominant role in the SH surface energy budget whereas precession is more important in the NH, explaining the different response of the NH and SH sea ice to precession and obliquity. The different response of the annual mean sea ice between the Arctic and Southern Oceans to obliquity and precession is related to their different geographic locations. The Arctic is located in the northern highest polar latitudes, while the Southern Ocean is located between about 60°S and 75°S; so the amplitude of the local summer insolation variation is much larger in the Arctic than in the Southern Ocean. In addition, the large area of the SH ocean makes it reacting more slowly than lands surrounding the Arctic Ocean and therefor more sensitive to the total energy integrated over time that is only a function of obliquity (Berger and Pestiaux, 1984; Berger et al., 2010). If the two periods 511-460 ka BP and 460-417 ka BP are considered separately, the results of the surface energy budget are in line with those of sea ice, the importance of obliquity being enhanced during 460-417 ka BP due to the low amplitude variation of precession (Table S3.3 and Table S3.4).

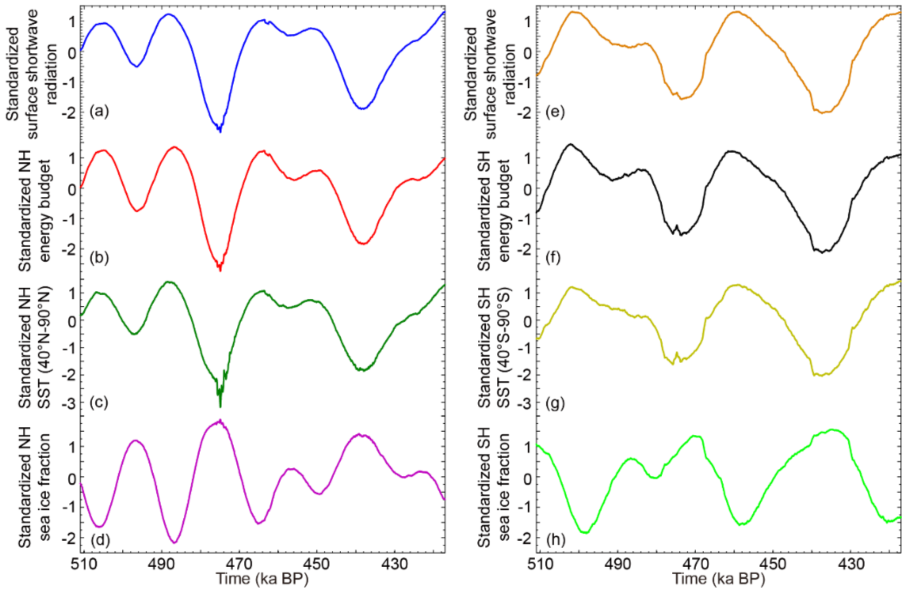

Figure 3.4 Comparison of the standardized annual mean sea ice fraction with the standardized annual mean SST, surface energy budget and surface shortwave radiation. (a) surface shortwave radiation in the NH (40°N-90°N), (b) surface energy budget in the NH (40°N-90°N), (c) SST in the NH (40°N-90°N), (d) Arctic sea ice fraction, (e) surface shortwave radiation in the SH (40°S-90°S), (f) surface energy budget in the SH (40°S-90°S), (g) SST in the SH (40°S-90°S), (h) Southern Ocean sea ice fraction. A 1000-year running mean is performed on the curves to reduce the high-frequency fluctuations.

Table 3.2 Regression coefficients of a linear multiple regression between the surface energy budget (the predictand) and E (eccentricity), O (obliquity) and P (precession) (the predictors). The calculation is based on the data of the whole simulation period between 511 and 417 ka BP. The surface energy budget has been standardized to have the regression coefficients representing comparable weights of the predictors on the predictand.

	surface energy budget			
	40°N-90°N	40°S-90°S	60°N-90°N	60°S-90°S
R^2	0.91	0.84	0.87	0.83
E	0.04	0.18	0.01	0.10
O	0.70	0.86	0.69	0.90
P	-0.75	-0.28	-0.74	-0.18

3.3 The response of SST to precession and obliquity

The SST variations at the low latitudes of both NH and SH show strong precessional signals (Figure 3.5), which can be partly explained by the very strong precessional signal in the daily insolation at low latitudes (Berger, 1978). In addition, the oceanic heat transports have a great contribution to the variations of the SST at low latitudes of both hemispheres, as shown from modern reanalysis data (Trenberth and Caron, 2001). Our simulated oceanic heat transports at low latitudes show very strong precessional signals (not shown), which could also explain the strong precessional signal in our simulated SST at low latitudes.

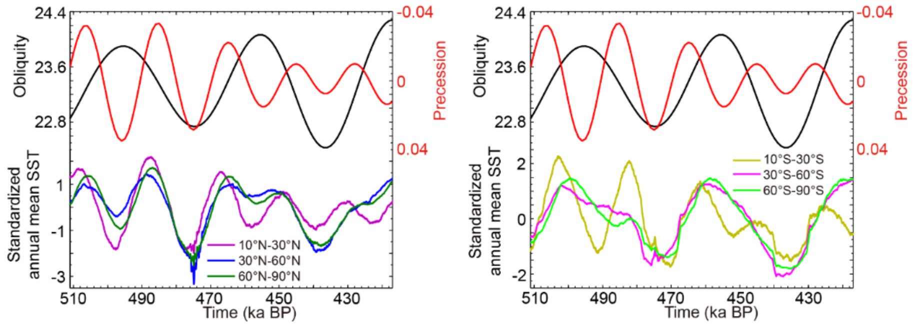

Figure 3.5 Comparison of the simulated standardized annual mean SST in the NH (left) and SH (right) with obliquity and precession. A 1000-year running mean is performed on the curves of the SST to reduce the high-frequency fluctuations.

At mid and high latitudes, there are obvious differences between the NH and SH in the SST response. In the SH, the SST variations are highly correlated with obliquity, while they are highly correlated with both obliquity and precession in the NH (Figure 3.5 and Table 3.1). In terms of proxy data, almost all SST records show strong periodicity around 100 ka after the mid-Pleistocene transitions. This is not shown in our simulated SST, most probably because only insolation is used in our experiment as forcing, GHG and ice sheets being kept constant. Besides the 100 ka cycle signals, in geological record, the SST of both hemispheres shows strong obliquity signal, but the precessional signal is much stronger in the NH than in the SH (Martrat et al., 2007; Bard and Rickaby, 2009). This is consistent with our simulated results. Compared to low latitudes, obliquity has a larger effect on the daily insolation at mid and high latitudes (Berger, 1978). Thus, the SST variations at mid and high latitudes of both hemispheres show stronger obliquity signals. In the meantime, the different distribution of continents and oceans between the NH and SH lead to different response in the two hemispheres. Due to the relatively slow response of oceans, the SST variations in the SH, where large area of oceans appear, are more sensitive to integrated insolation which is only a function of obliquity (Berger and Pestiaux, 1984; Berger et al., 2010). In the NH, the precessional forcing can be amplified by vegetation dynamics, leading to strong precessional signal in the annual mean

SST variations (Claussen et al., 2006; Ganopolski and Roche, 2009). In a previous study where LOVECLIM was used to study the last nine interglacials, it was also shown that the vegetation change in the NH mid and high latitudes is mainly controlled by precession (Yin and Berger, 2012). The same is found in our study for the time period investigated and the simulated vegetation shows strong precession signal (not shown). In addition, the variation of the Arctic sea ice shows strong precessional signal while the variation of the Southern Ocean sea ice shows strong obliquity signal, which would also influence the SST variations through sea ice-temperature feedbacks. Both vegetation and sea ice feedbacks in the NH explain the strong precessional signals in the NH SST variations. As discussed above, the key internal processes responsible for the response of SST to precession and obliquity are related to surface energy budget. Our results show that the surface energy budget and SST have a very good and positive relationship (for instance, at high latitudes of both hemispheres, Figure 3.6). When the surface energy budget is high, the SST is also high, and vice versa. Obviously, the surface energy budget is highly correlated with obliquity in the SH, while it is highly correlated with both precession and obliquity in the NH (Figure 3.6 and Table 3.2), which could explain the different response of the NH and SH SST at mid and high latitudes to precession and obliquity. The different response of the surface energy budget to precession and obliquity between two hemispheres is also due to the different distribution of continents and oceans in the NH and SH as discussed above.

If we analyze the results of 511-460 ka BP and 460-417 ka BP separately (Table S3.1 and Table S3.2), the results of 511-460 ka BP are similar to those obtained from the whole time period, but precession signal is more amplified as expected from the high amplitude variation of precession during this time period. It is also as expected from the low amplitude variation of precession during 460-417 ka BP, obliquity plays a more important role than precession in the SST in both NH and SH mid and high latitudes during this time period. Nevertheless, precession is still more important in the NH than

SH, similar to the results of sea ice. The results of the multiple linear regression analyses for the surface energy budget are consistent with the SST (Table S3.3 and Table S3.4).

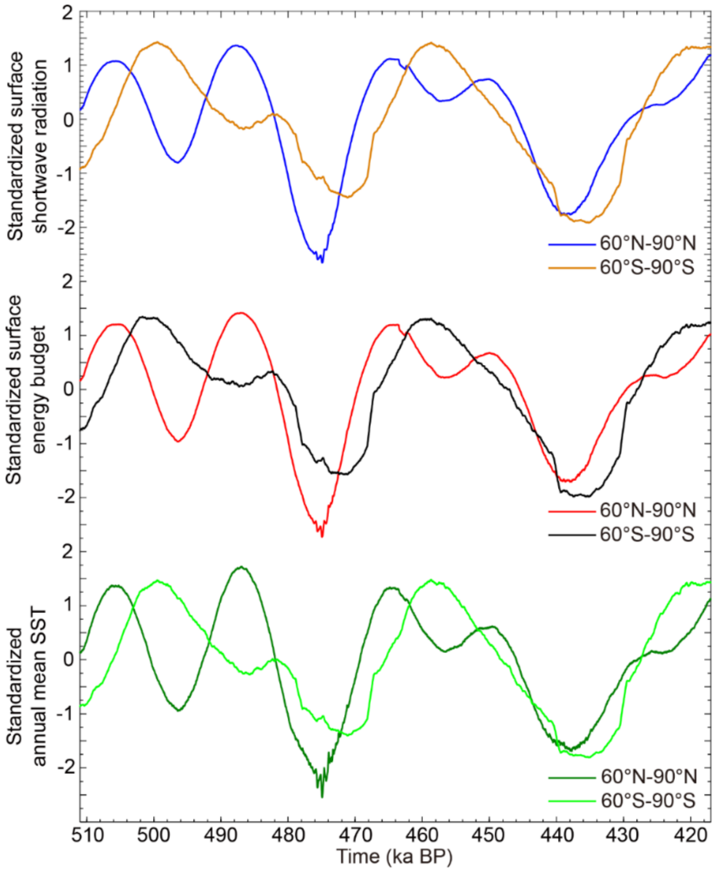

Figure 3.6 Comparison between the standardized annual mean SST at high latitudes and the standardized annual mean surface energy budget and surface shortwave radiation. A 1000-year running mean is performed on the curves to reduce the high-frequency fluctuations.

3.4 Conclusions

In this study, the different responses of the SST and sea ice to precession and obliquity between the two hemispheres are investigated through a transient simulation with the LOVECLIM model.

Our results show that the responses are different between the two hemispheres. The Arctic sea ice is highly correlated with precession, while the Southern Ocean sea ice is highly correlated with obliquity. In the Arctic, the variation of the annual mean sea ice is dominated by the variation in local summer which, through the surface energy budget and SST, is controlled by local summer insolation that in turn is mainly a function of precession. It is also influenced by the northward oceanic heat transports across 60°N which is mainly controlled by precession. In the Southern Ocean, the sea ice variations are more equally weighted between seasons with the amplitude being slightly larger in local summer during which the sea ice variation is dominated by obliquity. The large area of the SH oceans makes it reacting more slowly and being more sensitive to total energy integrated over time that is only a function of obliquity.

At low latitudes of both two hemispheres, the SST variations show strong precessional signal, due to strong precessional signal in the daily insolation at the low latitudes and also in the oceanic heat transports. Compared with low latitudes, the SST variations at mid-high latitudes show stronger obliquity signal in both two hemispheres due to the increased importance of obliquity in the daily insolation at mid-high latitudes. Due to sea ice and vegetation feedbacks and also large continental area, the SST variations in the mid-high latitudes of the NH show stronger precessional signal and weaker obliquity signal than in the SH.

Our results also show that during the period of low eccentricity and therefore of low amplitude variation of precession, obliquity always plays the dominant role in both sea ice and SST, which is quite expected, but precession is still more important in the NH than in the SH. Half-precessional signal vanishes during low-eccentricity period due to the reduced impact of precession.

Chapter 4 Effect of Hudson Bay closure on global and regional climate under different astronomical configurations[2]

4.1 Introduction

The Hudson Bay is one of the largest inland seas in the world and it receives a large amount of freshwater through riverine input (~760 km^3/yr; Déry et al., 2011). It is connected with the Arctic Ocean through the Canadian Arctic Archipelago and with the Labrador Sea through the Hudson Strait. The outflow through Hudson Strait into the Labrador Sea and on to the North Atlantic is thought to play an important role in the Labrador current, the northern North Atlantic circulation and its dense water formation (Figure 4.1; Straneo and Saucier, 2008). It thus has a great effect on the weather/climate of the Northern Hemisphere (NH), especially in the Labrador Sea and Atlantic, and perhaps over the whole globe (dos Santos et al., 2010).

---

[2] This chapter is published in Wu Z.P., Yin Q.Z., Ganopolski A., BergerA., Guo Z.T., 2023. Effect of Hudson Bay closure on global and regional climate under different astronomical configurations. Global and Planetary Change, 222, 104040.

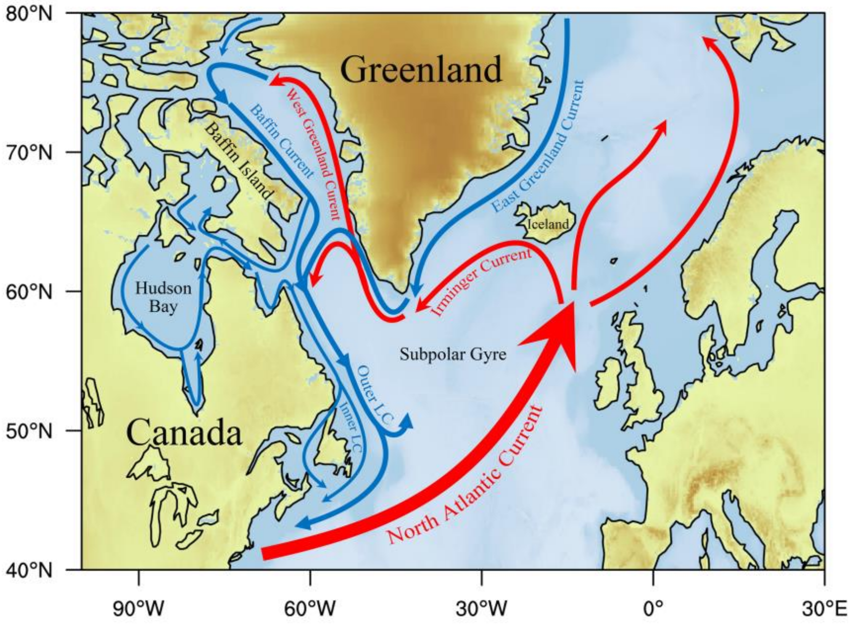

Figure 4.1 Map of Hudson Bay and surroundings showing modern surface circulations with cold (blue) and warm (red) currents (adopted from Straneo and Saucier, 2008; Lochte et al., 2020). The topography data is from https://www.ngdc.noaa.gov.

Due to the importance of the Hudson Bay on local and remote climate, some studies have been performed on the role of the Hudson Bay on climate variations in different time periods of the past. For instance, both geological records (e.g. Lochte et al., 2019) and numerical simulations (e.g. Wagner et al., 2013) suggested that the Hudson Bay Ice Saddle collapse may have played a significant role in the noticeable reduction of the Atlantic Meridional Overturning Circulation (AMOC) and the rapid NH cooling 8200 years before present (BP). Rennermalm et al. (2007) used the University of Victoria Earth system climate model (UVic ESCM) to investigate the sensitivity of the AMOC to the variations of freshwater flux into the Arctic Ocean and the Hudson Bay through riverine input, and their results show that, compared to the Arctic Ocean, decreasing freshwater flux into the Hudson Bay has a much greater effect on intensifying the AMOC. Using an early version of LOVECLIM, Friedrich et al. (2010) found that the atmospheric anomalies triggered by the internal variability over the Hudson Bay could drive freshwater release from the Hudson Bay into the Labrador Sea, which played a significant role in the centennial-to-millennial scale AMOC variability. Their study also showed that the centennial-to-millennial scale AMOC variability could only happen when the Hudson Bay was open, and it was suppressed under the last glacial maximum (LGM) boundary conditions when the Hudson Bay was closed. However, sensitivity experiments taking into account the time-varying insolation, greenhouse gases concentrations (GHG) and the NH ice sheets during the last interglacial showed that the Hudson Bay closure could not prevent the abrupt reduction of AMOC which was instead strongly dependent on the external forcings (Loutre et al., 2014).

During periods of maximum extent of the Laurentide ice sheet, the Hudson Bay was the geographic center of the Laurentide ice sheet and it was covered by ice sheet during a large portion of the Quaternary. During these times, Hudson Bay was partially or completely closed, leading to a very different hydrological condition in northeastern Canada. This could cause significant changes not only in local climate but also in climate of other places through its effect on the Atlantic Ocean circulations. However, the effect of the Hudson Bay closure is seldomly investigated in paleoclimate simulations, most probably due to the technical difficulty in modifying the land-sea mask in many models, and only a few studies have taken into account the changes of the Hudson Bay during different time periods (e.g. Friedrich et al., 2010; Meccia and Mikolajewicz, 2018; Tan et al., 2020). In most transient simulations with time-dependent ice sheets covering the glacial-interglacial cycle(s), the Hudson Bay was kept open (e.g. Smith and Gregory, 2012). It is unclear how the Hudson Bay condition (open or closed) affects the regional and global climate, especially under different background climate conditions. It could be one of the factors contributing to the simulation uncertainty and to model-proxy discrepancy.

In this study, we aim to investigate the effect of the Hudson Bay closure on the mean climate state under different background conditions (different astronomical configurations, GHG concentrations and ice sheet configurations). This would help us better understand the importance of the proper treatment of the ice mask and elevation of the Laurentide ice sheet in modelling studies, especially during the glacial times. The study of this Chapter is based on nine pairs of sensitivity experiments using the model LOVECLIM1.3. Within each pair of experiments, the Hudson Bay is open in one experiment and is closed in another one (OHB experiment and CHB experiment respectively, see Chapter 2).

4.2 The effect of Hudson Bay closure on global and regional climate

Figure 4.2 shows the sea surface temperature (SST) changes at the nine dates when the Hudson Bay is closed, and they can be divided into two groups according to their different characteristics. In group one which includes seven of the nine dates, 17, 133, 340, 538, 627, 719 and 794 ka BP, the NH becomes warmer with the largest warming of ~4 ℃ in the Labrador Sea, whereas the oceans in the Southern Hemisphere (SH) get cooler (Figure 4.2). The mean SST over the eastern North Atlantic (40° N-80° N, 50° W-30° E) increases with the maximum of about ~0.59 ℃ at 719 ka BP, and the average warming of the seven dates is about ~0.45 ℃. In group two which includes only 247 and 424 ka BP, the SST changes in the NH are very weak and even slightly opposite to the changes in group one, with a cooling of ~0.03 ℃ and ~0.26 ℃ respectively in the mean SST over the eastern North Atlantic. The changes in surface air temperature (SAT) show a similar pattern with the SST changes in both group one and group two (Figure 4.3). In group one, there is a warming over most regions of the NH and a cooling in the SH. Over the Labrador Sea, the SAT increases by ~6 ℃. In group two, the SAT change over the eastern North Atlantic is very weak at 247 ka BP, and there is a cooling at 424 ka BP. However, a large cooling of ~6 ℃ occurs over the Hudson Bay in both groups (Figure 4.3), which is due to the replacement of ocean by ice-covered land over this region. On the other hand, a warming occurs over the Baffin Bay, Davis Strait and north Labrador Sea in both groups (Figure 4.3), which is mainly due to the topography effect of the ice sheet over the Hudson Bay that alters the atmospheric stationary wave field.

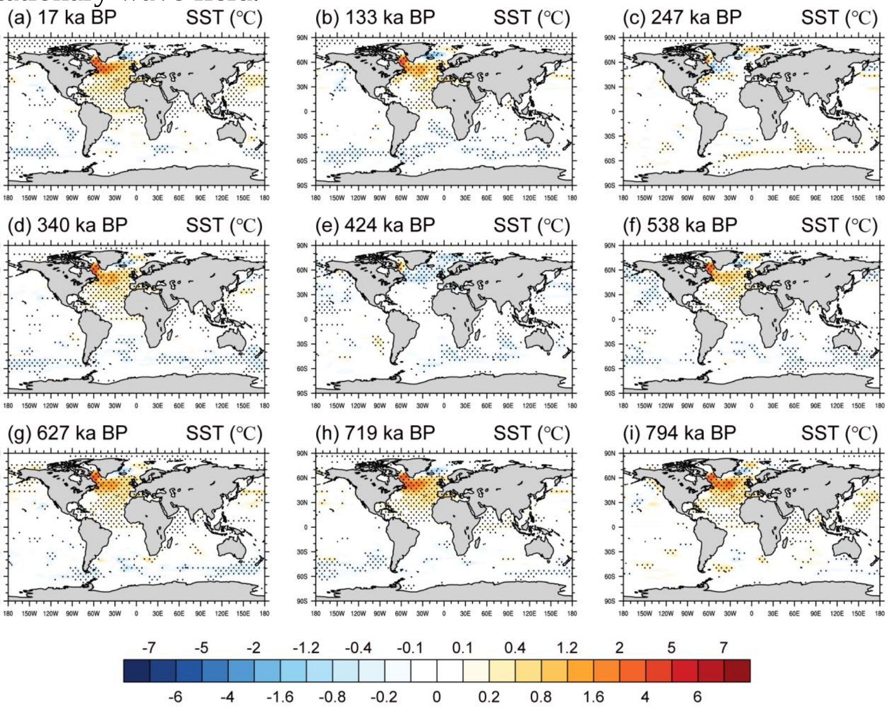

Figure 4.2 Impact of the Hudson Bay closure on annual mean sea surface temperature (SST) at (a) 17 ka BP; (b) 133 ka BP; (c) 247 ka BP; (d) 340 ka BP; (e) 424 ka BP; (f) 538 ka BP; (g) 627 ka BP; (h) 719 ka BP; (i) 794 ka BP. The difference between the CHB and OHB experiments are shown. Stippling indicates the statistically 95% significant changes by using a double sided t-test.

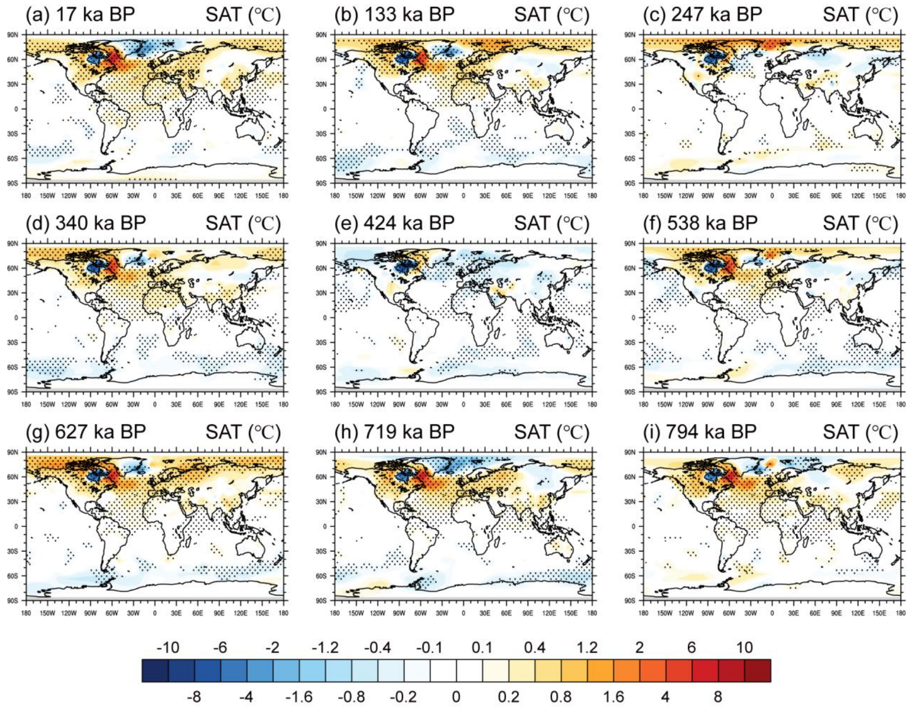

Figure 4.3 Same as Figure 4.2 but for annual mean surface air temperature (SAT).

In addition to temperature changes, the Hudson Bay closure also causes precipitation change at global scale especially in the tropical regions. In group one, there is more precipitation in the tropics of the NH and less precipitation in the tropics of the SH (Figure 4.4), which is related to a northward shift of the Inter-tropical Convergence Zone (ITCZ). While in group two, the variation of the ITCZ is very weak at 247 ka BP, and the ITCZ shifts southward at 424 ka BP, which leads to more precipitation in the tropics of the SH and less precipitation in the tropics of the NH (Figure 4.4).

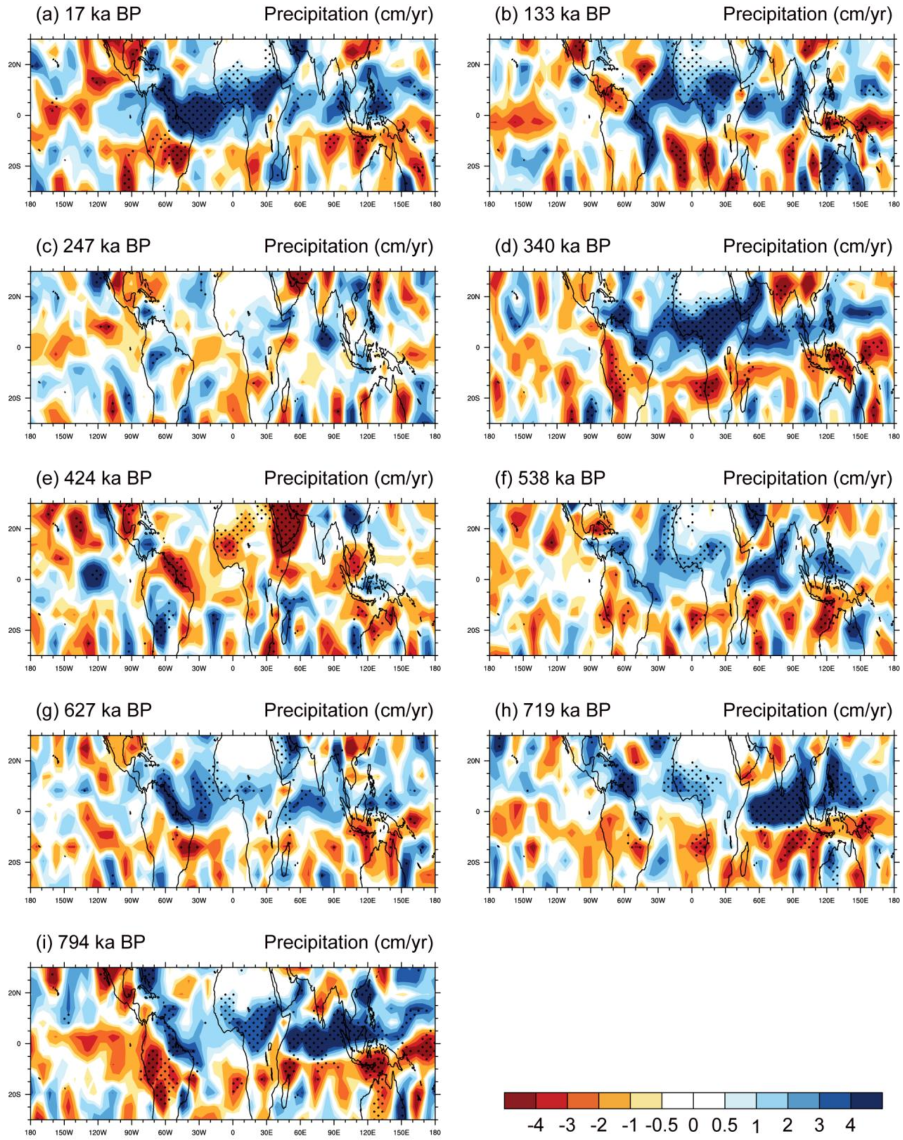

Figure 4.4 Same as Figure 4.2 but for annual mean tropical precipitation.

The results above show that the simulated effect of the Hudson Bay closure depends on background climate conditions. In group one, a warming in the NH and a cooling in the SH, and a northward shift of the ITCZ occur when the Hudson Bay is closed; while in group two, these climate changes are very weak and even slightly opposite to the changes in group one. In order to further investigate the mechanisms involved, the results of 133 ka BP and 424 ka BP are analyzed in

Section 4.3 to represent group one and group two respectively for illustration, and our additional analyses show that the processes are similar at the other dates of each group.

4.3 The forcing mechanisms for the global and regional climate changes

As mentioned above, the closure of the Hudson Bay causes a warming in the NH and a cooling in the SH, and a northward shift of the ITCZ at 133 ka BP (similar results are obtained for other dates in group one). The opposite change in temperature in the two hemispheres and a northward shift of the ITCZ are associated with a strengthening of AMOC (Figure 4.5a). The increase of the AMOC strength is 8.4% at 133 ka BP, and the average increase of the seven dates in group one is 5.5%. Accompanying the strengthening of AMOC, more heat is transported into the subpolar North Atlantic from the tropical-subtropical Atlantic, leading to an increase of the northward meridional heat transport (MHT). At 40° N in the North Atlantic, the Hudson Bay closure leads to an MHT increase of 6.98% at 133 ka BP, and the average increase of the seven dates in group one is 6.22%.

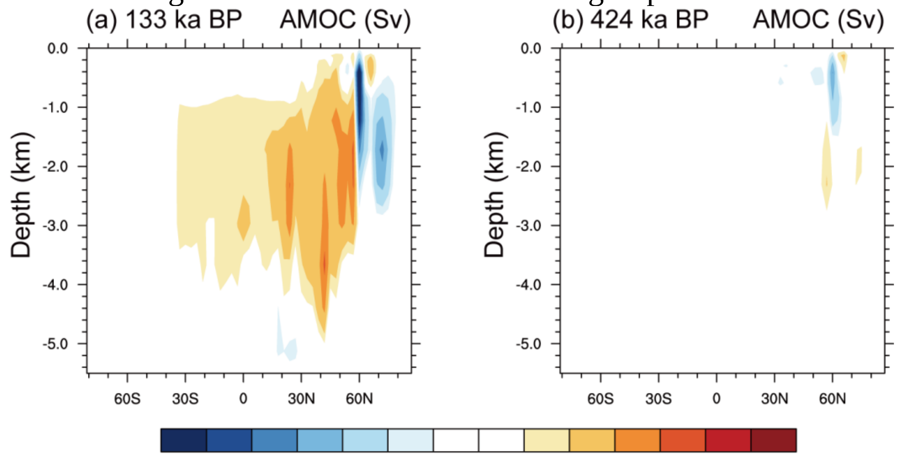

Figure 4.5 Differences between the CHB and OHB experiments in Atlantic meridional streamfunction at (a) 133 ka BP and (b) 424 ka BP.

In response to the enhanced northward MHT and the large warming in the Labrador Sea (Figure 4.6a and also Figure 4.2, Figure 4.3), sea ice substantially declines in the Labrador Sea (Figure 4.6c), which would further enhance the warming. However, sea ice increases to the southeast of Greenland due to more sea ice export from the Arctic (Figure 4.6c) which is driven by northeasterly wind anomaly (Figure 4.6b). The increased sea ice in turn leads to a cooling to the southeast of Greenland (Figure 4.6a and also Figure 4.2, Figure 4.3). This cooling anomaly and the one over the Hudson Bay lead to subsidence anomaly over these regions; the warming anomalies in the Labrador Sea and the northeast North Atlantic lead to ascent anomaly over these regions (Figure 4.6d). These ascent and subsidence anomalies finally lead to more precipitation over both the northeast North Atlantic and the Labrador Sea but less precipitation over the Hudson Bay and southeast of Greenland (Figure 4.6e).

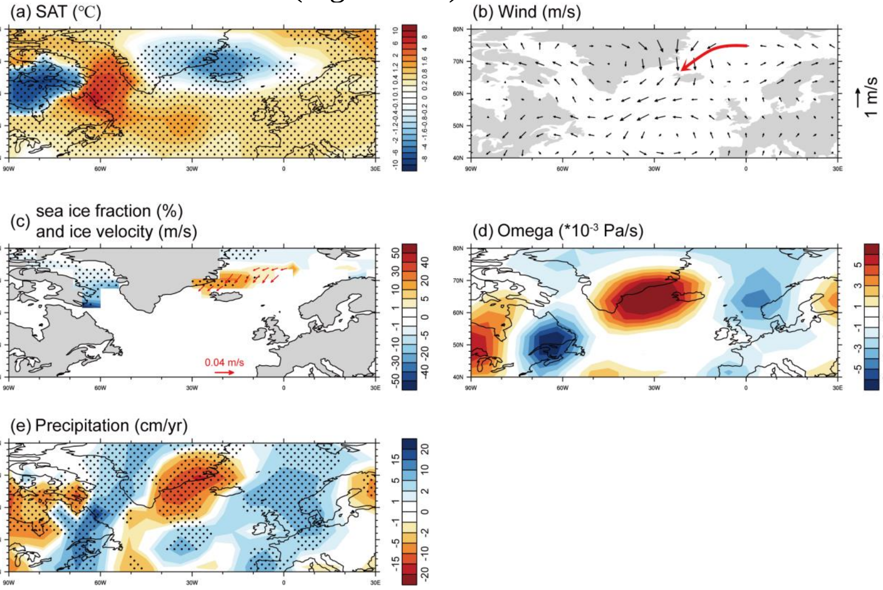

Figure 4.6 Differences between the CHB and OHB experiments at 133 ka BP in: (a) SAT, (b) 800 hPa wind, (c) sea ice fraction (shaded) and ice velocity (arrows) over the sea ice increased regions, (d) 650 hPa omega field indicating vertical motion in the atmosphere (negative anomalies for ascent and positive anomalies for subsidence), and (e) precipitation. Stippling indicates the statistically 95% significant changes by using a double sided t-test.

To have a better understanding of the effect of the Hudson Bay closure at 133 ka BP, it is essential to understand how it affects the AMOC. When the Hudson Bay is closed, the evaporation minus precipitation is increased in the Labrador Sea (Figure 4.7a) due to the strongly increased evaporation, which is related to the largest warming there (Figure 4.6a and also Figure 4.2, Figure 4.3), and the sea surface water becomes saltier in the Labrador Sea (Figure 4.7b), leading to denser surface water (Figure 4.7c), and finally stronger deep convection there (as diagnosed by mixed layer depth; Figure 4.7d). Again, the results of other dates in group one (not show) are similar with the results at 133 ka BP. The Labrador Sea is one of major centers for deep-water formation in the North Atlantic (e.g. Thornalley et al., 2018) and also in LOVECLIM1.3 (Yin et al., 2021). The stronger deep convection in the Labrador Sea leads to a more vigorous AMOC.

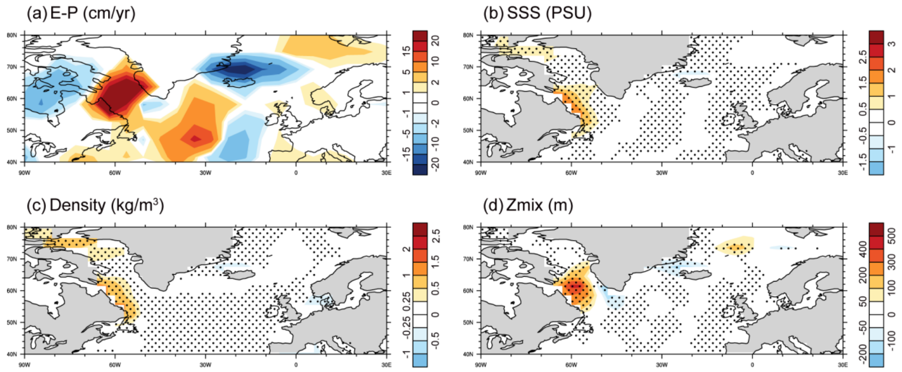

Figure 4.7 Differences between the CHB and OHB experiments at 133 ka BP in (a) E - P (evaporation minus precipitation), (b) SSS, (c) sea surface density and (d) mix layer depth. Stippling indicates the statistically 95% significant changes by using a double sided t-test.

On the other hand, as mentioned above, the effect of the Hudson Bay closure at 424 ka BP is slightly opposite as compared to that at 133 ka BP, which causes a cooling in the NH and a southward shift of the ITCZ at 424 ka BP. However, both the AMOC (Figure 4.6b) and the northward MHT at 40° N in the North Atlantic vary very small (less than 1%) at 424 ka BP. The cooling in the NH and a southward shift of the ITCZ at 424 ka BP should be related to the cooling over the Hudson Bay (Figure 4.3) which could cool the climate locally and also in the mid-high latitudes through atmospheric circulations and sea ice feedbacks. The different effect of the Hudson Bay closure on the global and regional climate in group one and group two must be related to differences in background climate conditions. However, a simple relationship is hard to be found mainly due to the joint effect of several different forcing factors.

4.4 Comparison of the effect of Hudson Bay closure with the effect of ice sheets

In order to assess the effect of the Hudson Bay closure in comparison with the effect of the property changes of the ice sheets themselves, we compare their respective effects on the annual mean SST and SAT using the results at 133 ka BP and 424 ka BP (Figure 4.2, Figure 4.3 and Figure 4.8).

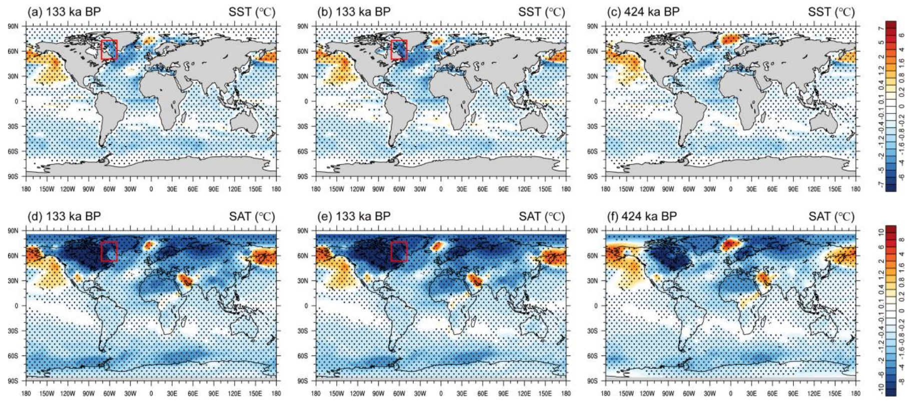

Figure 4.8 The combined effect of the NH ice sheets and Hudson Bay closure on temperature at 133 ka BP, and the individual effect of the NH ice sheets on temperature at 133 ka BP and 424 ka BP. (a) SST anomaly and (d) SAT anomaly between the CHB and OG experiments, (b, c) SST anomaly and (e, f) SAT anomaly between the OHB and OG experiments. Stippling indicates the statistically 95% significant changes by using a double sided t-test.

As compared to the pre-industrial condition (PI), the NH ice volume increases by 23.04 and 16.52 million km^3 at 133 ka BP and 424 ka BP respectively (it is 36.93 million km^3 for the Last Glacial Maximum) (Ganopolski and Calov, 2011). The large NH ice sheets at these dates cause substantial cooling almost everywhere over the globe, especially in the high latitudes and over the ice sheets. Over the Labrador Sea, the SST decreases by ~7 ℃ and SAT decreases by ~10 ℃ at 133 ka BP (Figure 4.8). The cooling in the NH at 424 ka BP is smaller than that at 133 ka BP, which is mainly due to its smaller NH ice sheets. However, there is a notable warming in the northern North Pacific in both SST and SAT. This warming has also been found in the ice sheets experiments of other studies (e.g. Yin et al., 2009; Muri et al., 2012; Ullman et al., 2014) and it is related to the topography effect of the North American ice sheet, which significantly alters the atmospheric stationary wave field and induces an increased energy-flux convergence in the northern North Pacific (e.g. Ullman et al., 2014; Liakka and Lofverstrom, 2018; Shi et al., 2020).

As compared to the effect of the NH ice sheets, the effect of the Hudson Bay closure could be quite significant, especially in the northern North Atlantic region and the surrounding continents (Figure 4.2, Figure 4.3 and Figure 4.8). For example, at 133 ka BP, the SST increases by ~4 ℃ over the Labrador Sea and ~1.1 ℃ over the North Atlantic (40° N-80° N, 90° W-30° E) when the effect of the Hudson Bay closure is considered, while it decreases by ~7 ℃ over the Labrador Sea and ~2.1 ℃ over the North Atlantic when the effect of the NH ice sheets is considered. However, as showed in Section 4.2, the effect of the Hudson Bay closure could vary according to background climate conditions. It causes strong warming in the North Atlantic in most cases, but it could also lead to slight cooling or be very weak. Thus, in glacial climate simulations, the ice-sheet-induced cooling in the North Atlantic and a large area of the NH would be weakened (like in group one) or with no obvious change and even be slightly reinforced (like in group two) if the effect of the Hudson Bay closure is considered, depending on background climate conditions. For example, at 133 ka BP, the cooling in the Labrador Sea would be significantly decreased under the combined effect of NH ice sheets and Hudson Bay closure, as compared to the individual effect of NH ice sheets (Figure 4.8).

4.5 Conclusions

In this study, the effect of Hudson Bay closure on AMOC and on global and local climate during different glacial times is investigated using the model LOVECLIM1.3. The model results show that, at 133 ka BP (other dates in group one show similar results), the Hudson Bay closure could lead to an intensification of the AMOC mainly due to the increased evaporation minus precipitation over the Labrador Sea which leads to saltier water and stronger deep convection in the Labrador Sea. The intensification of AMOC in turn leads to a warming in the NH especially in the Labrador Sea and northeast North Atlantic, a cooling in the SH, and a northward shift of the ITCZ. However, the effect of the Hudson Bay closure on AMOC and on global climate depends to some degree on background climate conditions. For example, its effect is opposite at 424 ka BP as compared to that at 133 ka BP.

In addition to the large-scale climate changes related to the variations of AMOC, the closure of Hudson Bay also leads to notable local cooling in all the experiments. The change of the Hudson Bay from ocean to ice-covered land causes a strong cooling over the Hudson Bay region due to the modifications of surface properties and elevation. It also leads to a cooling to the southeast of Greenland due to more sea ice export from the Arctic driven by northeasterly wind anomaly.

The large-scale climate response to the NH ice sheets in our model is similar to the results obtained in other models. As compared to the effect of the NH ice sheets that existed during the studied glacial times, the effect of the Hudson Bay closure also could be very significant, especially in the northern North Atlantic and the surrounding continents. In glacial climate simulations, the ice-sheet-induced cooling in the North Atlantic and in the NH would be weakened or even be slightly enhanced if the effect of the Hudson Bay closure is considered, depending on background climate conditions.

Our simulated results show that the effect of Hudson Bay closure could be significant especially at regional scale in the Hudson Bay and North Atlantic regions. However, we also note that the LOVECLIM1.3 model has a relatively coarse resolution and it has only one grid in the Strait between the Hudson Bay and the Labrador Sea, which could be a limitation in resolving well the currents in the Strait and thus the exchanges between the Baffin Bay and the Labrador Sea. Higher resolution ocean models including more detailed processes could be used to test the effect of the Hudson Bay closure.

Chapter 5 Hemisphere differences in response of sea ice and sea surface temperature to astronomical parameters, CO_2 and Northern Hemisphere ice sheets

5.1 Introduction

As mentioned in Chapter 3 Section 3.1, both geological records and numerical simulations show that the climate in the two hemispheres seems to respond differently to astronomical parameters, CO_2 and ice sheets. However, systematic study is rare and the mechanisms remain not very well understood. In Chapter 3, the hemisphere differences in the response of sea ice and SST to precession and obliquity has been investigated based on a transient simulation with only varied insolation from 511 to 417 ka BP using the model LOVECLIM1.2 (T511_Orb experiment, see Chapter 2). This Chapter 5 focuses on investigating the effects of CO_2 and NH ice sheets on the climate of the two hemispheres, but also briefly includes some results on the response to astronomical forcing using new simulations with LOVECLIM1.3. Three sets of transient simulations are performed during MIS-13 (T538_Orb, T538_OrbGHG and T538_OrbGHGICE experiments) and MIS-11 (T424_Orb, T424_OrbGHG and T424_OrbGHGICE experiments) (see Chapter 2 for experiment description). In the Orb experiments, only astronomical parameters (Berger and Loutre, 1991) vary with time, the GHG concentrations and ice sheets being fixed at the pre-industrial values; in the OrbGHG experiments, the influence of GHG concentrations (Lüthi et al., 2008; Loulergue et al., 2008; Schilt et al., 2010) is additionally considered; in the OrbGHGICE experiments, the influence of NH ice sheets (Ganopolski and Calov, 2011) is additionally considered. The effects of CO_2 and NH ice sheets are depicted based on the difference between the OrbGHG and Orb experiments, and between the OrbGHGICE and OrbGHG experiments respectively.

These two interglacials are chosen here mainly due to the reasons below. In terms of the different external drivers, the different astronomical configurations lead to different insolation changes during MIS-13 and MIS-11. Eccentricity is large, leading to large amplitude variation of precession during MIS-13, while the amplitude variation of precession is small during MIS-11 due to its small eccentricity (Berger and Loutre, 1991). On the other hand, the amplitude variation of obliquity is larger during MIS-11 than during MIS-13 (Berger and Loutre, 1991). The CO_2 concentration is higher (280 ppmv VS 240 ppmv) but its amplitude variation is smaller during MIS-11 than during MIS-13 (Lüthi et al., 2008), and the amplitude variation of the NH ice volume is larger during MIS-13 than MIS-11 (Ganopolski and Calov, 2011). Therefore, MIS-13 and MIS-11 show significant differences in forcings and they contain different background climate conditions. In addition, MIS-11 is one of the longest and warmest interglacials during the last million years (e.g. Lang and Wolff, 2011; Dutton et al., 2015) and it has been regarded as a possible analogue of our present interglacial (MIS-1) due to its similar astronomical configurations and CO_2 concentration (e.g. Berger and Loutre, 2002, 2003; Tzedakis, 2010; Yin and Berger, 2015). MIS-13 is a special interglacial at least over the last million years with extremely asymmetrical hemispheric climate (e.g. Yin and Guo, 2008; Yin et al., 2008, 2009; Guo et al., 2009; Shi et al., 2020). Both of them have received much attention in paleoclimate study.

5.2 Influence of astronomical parameters on sea ice and SST

Figure 5.1 shows the variabilities of the annual mean Arctic and Southern Ocean sea ice area during MIS-13 and MIS-11 in response to astronomical parameters alone. During MIS-13, the variability of the annual mean Arctic sea ice area is dominated by precession, while the variability of the annual mean Southern Ocean sea ice area is dominated by obliquity (Figure 5.1, left). During MIS-11, the variabilities of the annual mean sea ice in both Arctic and Southern Ocean are dominated by obliquity (Figure 5.1, right). However, precession still plays a more important role in the Arctic than in the

Southern Ocean, and obliquity is more important in the Southern Ocean than in the Arctic (Figure 5.1, right).

For the SST, Figure 5.2 shows that, during MIS-13, the variabilities of the annual mean SST at low latitudes of both hemispheres are dominated by precession, while they are dominated by obliquity at SH mid and high latitudes, and they are dominated by both obliquity and precession at NH mid and high latitudes (Figure 5.2, left). During MIS-11, the variabilities of the SST at low latitudes of both hemispheres are still dominated by precession (Figure 5.2, right), and obliquity plays a dominant role at mid and high latitudes.

The relative importance of precession and obliquity on the annual mean Arctic and Southern Ocean sea ice and SST at different latitudinal bands in LOVECLIM1.3 are well consistent with those in LOVECLIM1.2 (Chapter 3, Wu et al., 2020). The internal climate processes and feedbacks are also similar and as they have been explained in Chapter 3, they are not repeated here.

In addition to orbital timescale variations which well follow the variations of precession and obliquity, the Arctic and Southern Ocean sea ice and the SST at different latitudinal bands also show some abrupt and millennial changes. These changes are related to abrupt and millennial AMOC changes triggered by insolation threshold as shown in Yin et al. (2021).

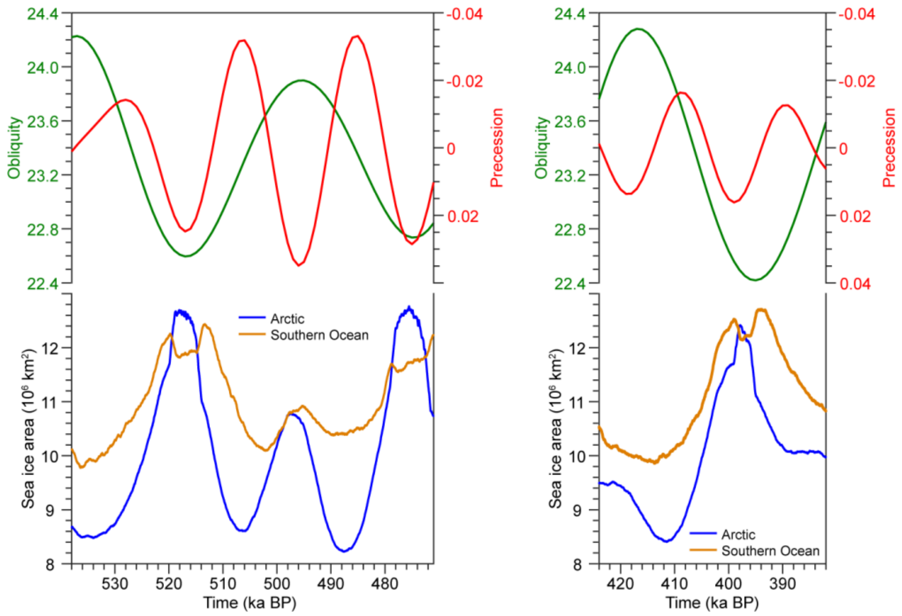

Figure 5.1 Comparisons of the simulated annual mean Arctic and Southern Ocean sea ice area with precession and obliquity (Berger and Loutre, 1991) during MIS-13 (left) and MIS-11 (right). The simulations, T538_Orb and T424_Orb, are driven by insolation change only. A 1000-year running mean is performed on the curves of the sea ice area to reduce the high-frequency fluctuations.

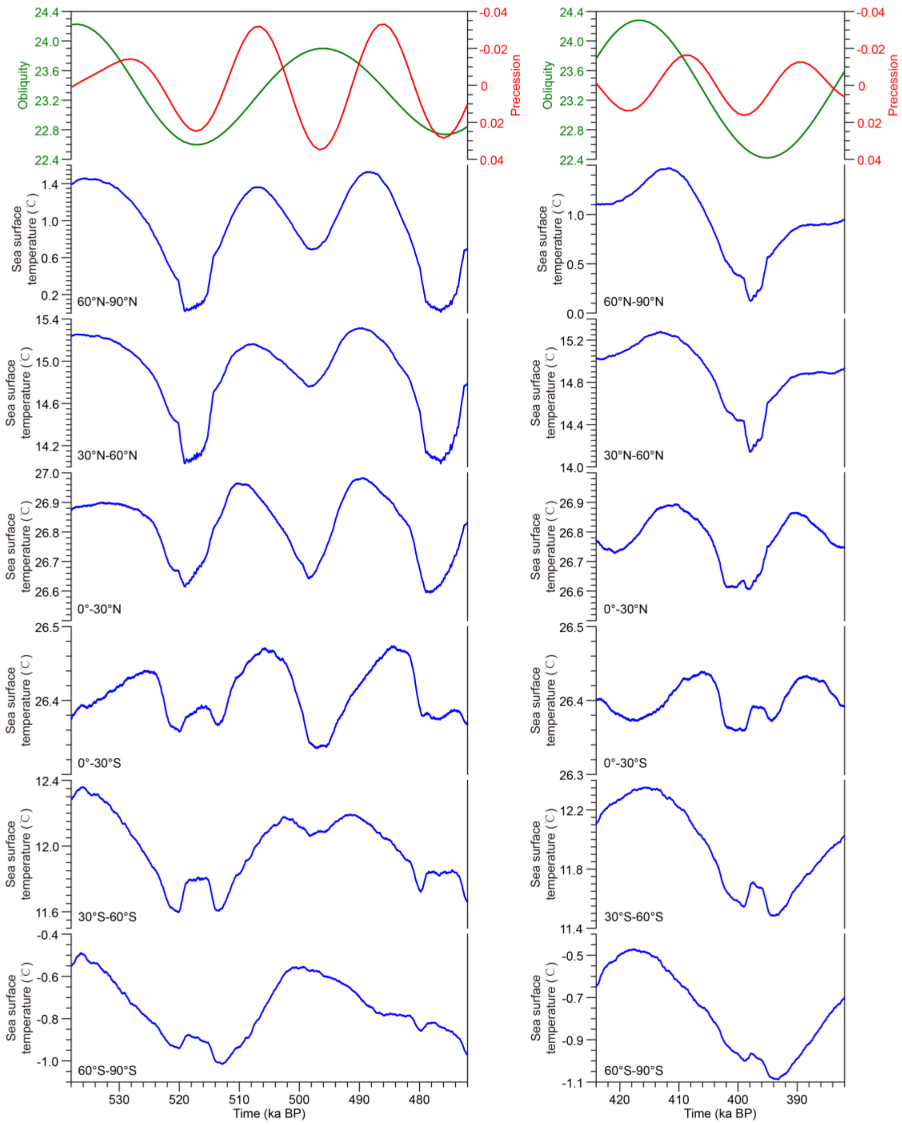

Figure 5.2 Comparisons of the simulated annual mean SST at different latitudinal bands with precession and obliquity (Berger and Loutre, 1991) during MIS-13 (left) and MIS-11 (right). The simulations, T538_Orb and T424_Orb, are driven by insolation change only. A 1000-year running mean is performed on the curves of the SST to reduce the high-frequency fluctuations.

5.3 Impacts of CO_2 on sea ice and SST

Figure 5.3 shows the impacts of CO_2 on the annual mean Arctic and Southern Ocean sea ice. During MIS-13, the CO_2 forcing induced changes of the annual mean Arctic and Southern Ocean sea ice areas both are near out-of-phase with the CO_2 forcing. As expected, increased CO_2 concentration leads to a warming in both the Arctic and Southern Ocean, which finally reduces the sea ice area (Figure 5.3). In addition, the amplitude of variation of the annual mean sea ice area in the Southern Ocean is larger than in the Arctic (Figure 5.4), and the variation of CO_2 has a higher correlation with the annual mean sea ice area change in the Southern Ocean (correlation coefficient R^2=0.92) than in the Arctic (correlation coefficient R^2=0.69), showing that CO_2 plays a more important role in the annual mean sea ice area in the Southern Ocean. This is in agreement with previous results obtained from the snapshot experiments for the last nine interglacials using LOVECLIM1.2 (Yin and Berger, 2012). To investigate the impacts of CO_2 on the annual mean Arctic and Southern Ocean sea ice, the results of the Orb and OrbGHG experiments at 531.7 ka BP are analyzed, because they have the largest difference in CO_2 concentration (280 ppmv VS 191 ppmv) during the MIS-13 simulation period. The results (Figure 5.4) show that as compared to the high CO_2 concentration, the SST decreases and sea ice concentration increases in both the Arctic and Southern Ocean when the CO_2 concentration is low. In addition, the changes of both the SST and sea ice concentration are larger in the Southern Ocean than in the Arctic (Figure 5.4).

As compared to MIS-13, the amplitude of variations of the Arctic and Southern Ocean sea ice area changes are smaller during MIS-11, which are quite expected due to the smaller amplitude variation of CO_2 during MIS-11 (Figure 5.3). Nevertheless, the amplitude variation of the sea ice area change is still larger in the Southern Ocean than in the Arctic (Figure 5.3), and CO_2 still has a larger correlation with the Southern Ocean sea ice area difference (correlation coefficient R^2=0.93) than with the Arctic sea ice area difference (correlation coefficient R^2=0.78) during MIS-11.

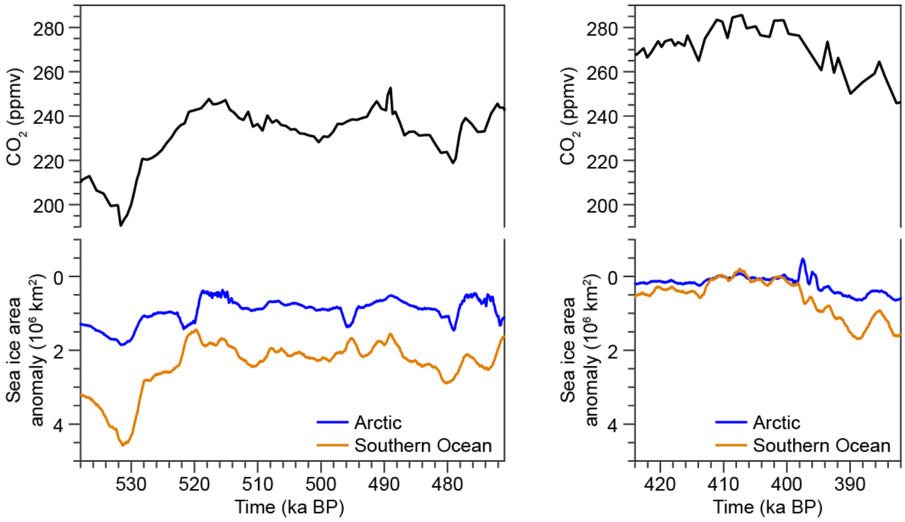

Figure 5.3 The impacts of CO_2 on the annual mean Arctic and Southern Ocean sea ice area during MIS-13 (left) and MIS-11 (right). The sea ice area anomaly represents the sea ice area difference between the OrbGHG and Orb experiments.

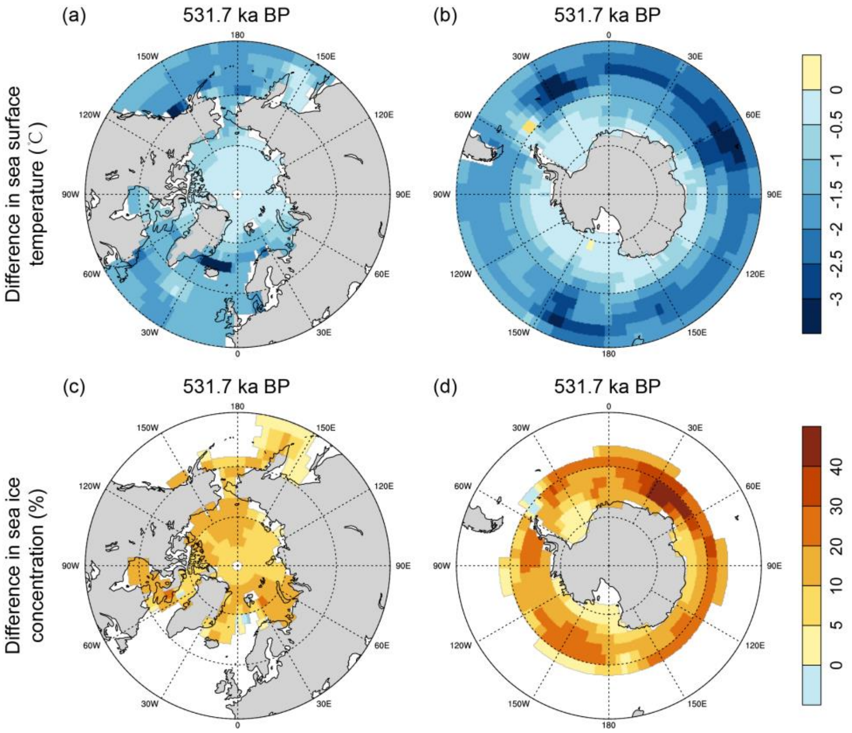

Figure 5.4 The impacts of CO_2 on the annual mean SST and sea ice concentration. Difference in SST and sea ice concentration in the Arctic (a, c) and Southern Ocean (b, d) at 531.7 ka BP between OrbGHG and Orb experiments.

Figure 5.5 shows the impacts of CO_2 on SST at different latitudinal bands of both hemispheres. During MIS-13, the CO_2 forcing induced changes of SST at all latitudinal bands are near in-phase with the CO_2 forcing. The amplitude of variations of SST at mid-high latitudes are larger than at low latitudes of both the NH and SH, and the variation of CO_2 has a higher correlation with the SST changes at SH mid-high latitudes (correlation coefficient R^2=0.95) than at NH mid-high latitudes (correlation coefficient R^2=0.78), showing that CO_2 plays a more important in the SST at SH mid-high latitudes than at NH mid-high latitudes, which is similar with the results of sea ice area. As compared to MIS-13, the amplitude of variations of the SST at all latitudinal bands are smaller during MIS-11, which is due to its weaker variation of CO_2 (Figure 5.5). The amplitude of variations of

SST are still larger at mid-high latitudes than at low latitudes of both hemispheres, and the variation of CO_2 always has high correlations with the SST changes at SH mid-high latitudes (correlation coefficient R^2=0.95) and at NH mid-high latitudes (correlation coefficient R^2=0.86) (Figure 5.5).

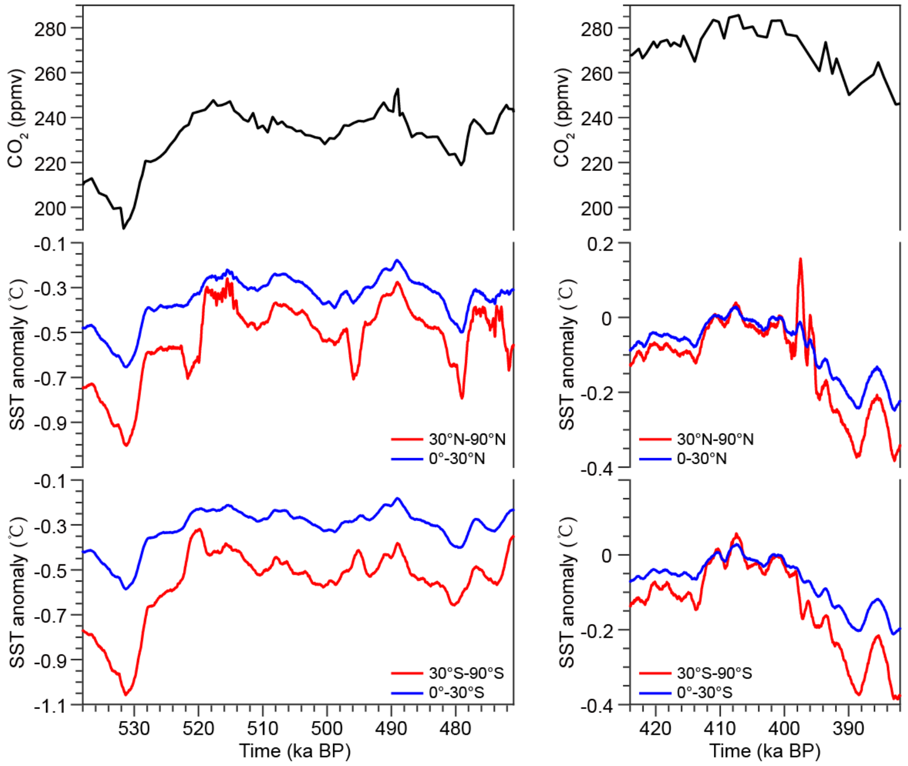

Figure 5.5 The impacts of CO_2 on the annual mean SST at different latitudinal bands during MIS-13 (left) and MIS-11 (right). The SST anomaly represents the SST difference between the OrbGHG and Orb experiments.

In addition to the changes which well fellow the variations of CO_2, both the sea ice and SST also show some abrupt and millennial changes, especially in the NH. For example, the sea ice and SST changes at about 523-514 ka BP, 497-494 ka BP and 480-471 ka BP during MIS-13 and 399-395 ka BP during MIS-11 do not follow the variations of CO_2, but show obvious abrupt and millennial changes (Figure 5.3 and Figure 5.5). These could be explained by the modulated effect of CO_2 on the abrupt and millennial climate changes triggered by the insolation threshold, which lead to some differences in the start and end time of the abrupt climate changes, as well as the amplitude and periodicities of the millennial climate changes between the OrbGHG and Orb experiments (Yin et al., 2021).

5.4 Effect of NH ice sheets on sea ice and SST

In our experiments, the NH ice sheets affect the climate system mainly via the changes in topography, albedo and land surface, as well as the changes of the Hudson Bay (Wu et al., 2023), but the potential effect of fresh water induced by ice melting is not included. Normally, the high albedo of the ice sheets would have a cooling effect, but the ice sheet topography could lead to a warming in some land regions and over the surrounding oceans, like in the North Pacific (Yin et al., 2009; Muri et al., 2012; Ullman et al., 2014; Lyu and Yin, 2022; Wu et al., 2023). The effect of the Hudson Bay also depends on the background climate conditions (Chapter 4, Wu et al., 2023).

Figure 5.6 shows the effect of NH ice sheets on the Arctic and Southern Ocean sea ice. During MIS-13, the relationship between the Arctic sea ice change and the NH ice volume seems quite complex and nonlinear. Previous studies have shown that the influence of NH ice sheets on the climate system especially the Asian monsoon depends on their size, shape and location, as well as the NH summer insolation (Yin et al., 2008, 2009; Lyu and Yin, 2022). In order to further investigate the influence of NH ice sheets on the Arctic sea ice, four time periods (531, 520, 503, 490 ka BP) characterized by different combinations of ice sheets and insolation are selected.

At 531 ka BP, the NH ice volume anomaly relative to PI is about 18 million km^3 (49% of the LGM one), with relatively large North American and Eurasian ice sheets (Figure 5.7a), and the NH summer insolation reaches a maximum. The North Pacific becomes warmer due to the topography effect of the North American ice sheet (Figure 5.8a, 5.8b), which leads to less sea ice there (Figure 5.7e). In response to the large ice sheets at 531 ka, the AMOC gets intensified (Figure 5.9a), which could, together with the topography effect of the ice sheets, contribute to the warming to the east of Greenland (Figure 5.8a, 5.8b) and thus less sea ice there (Figure 5.7e). On the other hand, the high albedo of the ice sheets contributes to a cooling in the Arctic and North Atlantic (Figure 5.8a, 5.8b) and therefore more sea ice (Figure 5.7e).

At 520 ka BP, the NH ice volume anomaly relative to PI is about 23 million km^3 (60% of the LGM one), also with large North American and Eurasian ice sheets (Figure 5.7b) like at 531 ka BP, but the NH summer insolation is low. As compared to 531 ka BP, the topography effect of the North American ice sheet is much stronger under the low summer insolation condition of 520 ka BP, leading to a stronger warming and thus much less sea ice in the North Pacific (Figure 5.8c, 5.8d, 5.7f). The ice-sheet-induced AMOC intensification is also stronger at 520 ka BP (Figure 5.9b), which leads to a warming in the Labrador Sea and Greenland-Iceland-Norwegian (GIN) Seas (Figure 5.8c, 5.8d) and thus less sea ice there (Figure 5.7f).

At 503 ka BP, the NH ice volume anomaly relative to PI is only about 3 million km^3, with a very small North American ice sheet and almost no Eurasian ice sheet (Figure 5.7c), and the NH summer insolation is relatively high. The change of ice sheets leads to a warming and thus less sea ice in the Arctic, North Pacific and Labrador Sea, but a cooling and more sea ice in the North Atlantic (Figure 5.8e. 5.8f, Figure 5.7g). At 490 ka BP, the total NH ice volume is almost the same as at 503 ka BP, and the NH summer insolation is also relatively high, but the ice sheet is mainly concentrated on Eurasia (Figure 5.7d). These lead to a warming and less sea ice in the Labrador Sea, but a cooling and more sea ice in other regions (Figure 5.8g, 5.8h, Figure 5.7h).

The results at these four dates clearly show that the effect of the NH ice sheets on the Arctic sea ice is nonlinear, which depends on the size and location of the ice sheets, as well as the NH summer insolation.

As compared to the Arctic, the response of the Southern Ocean sea ice to the NH ice volume change is more linear. It follows well the variations of the NH ice volume (Figure 5.6) with a high correlation (correlation coefficient R^2=0.94). A larger NH ice volume leads to a stronger cooling and more sea ice in the Southern Ocean. The cooling in the Southern Ocean induced by the NH ice sheets has also been reported in Ganopolski and Roche (2009) and Roberts and Valdes (2017). Their results suggested that a stronger northward oceanic heat transport is responsible for the cooling in the SH, which is in line with our results. At 520 ka BP, the large NH ice sheets lead to a strong intensification of the AMOC (Figure 5.9b) and a strong northward oceanic heat transport (the oceanic heat transport across 30°S in the Atlantic is enhanced about 0.14 Pw (70%)). While at 490 ka BP, in response to the small NH ice sheets, the change of AMOC is small (Figure 5.9d) and the oceanic heat transport across 30°S in the Atlantic is only 0.02 Pw. Moreover, the cooling in the Southern Ocean could be amplified by sea ice feedbacks, like what has also been found for the LGM (Sherriff-Tadano and Abe-Ouchi, 2020).

During MIS-11, the effect of NH ice sheets on the Arctic and Southern Ocean sea ice is similar with that during MIS-13, but the amplitudes of both the Arctic and Southern Ocean sea ice area changes are smaller than theose during MIS-13 due to its smaller amplitude of variation of NH ice volume (Figure 5.6).

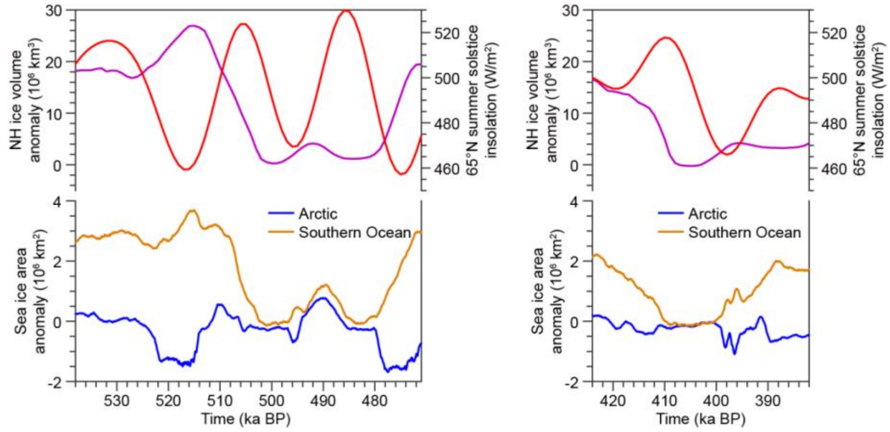

Figure 5.6 The effect of NH ice sheets on the annual mean Arctic and Southern Ocean sea ice area during MIS-13 (left) and MIS-11 (right). The sea ice area anomaly represents the sea ice area difference between the OrbGHGICE and OrbGHG experiments.

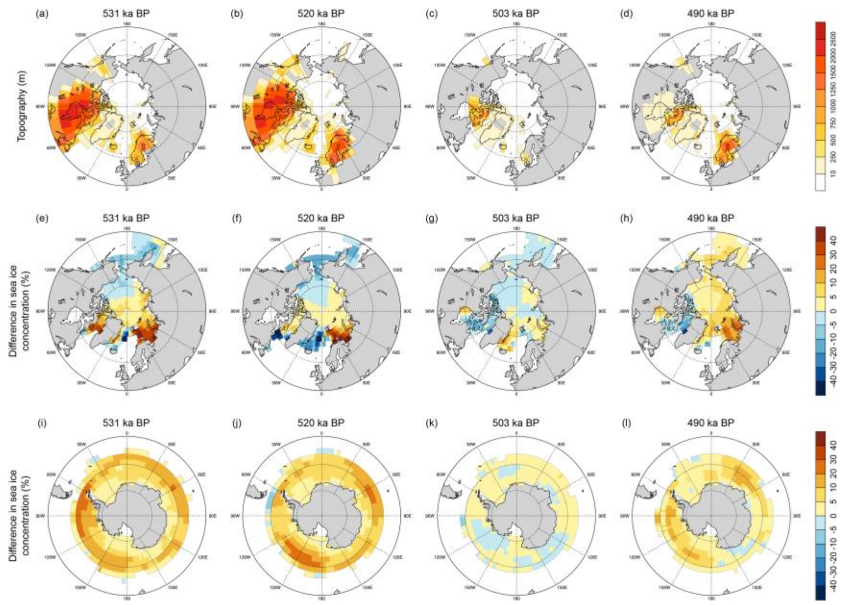

Figure 5.7 The effect of NH ice sheets on the annual mean Arctic and Southern Ocean sea ice concentration. The topography anomaly is relative to the PI and the difference in sea ice concentration is between the OrbGHGICE and OrbGHG experiments at 531 ka BP (a, e, i), 520 ka BP (b, f, j), 503 ka BP (c, g, k) and 490 ka BP (d, h, l).

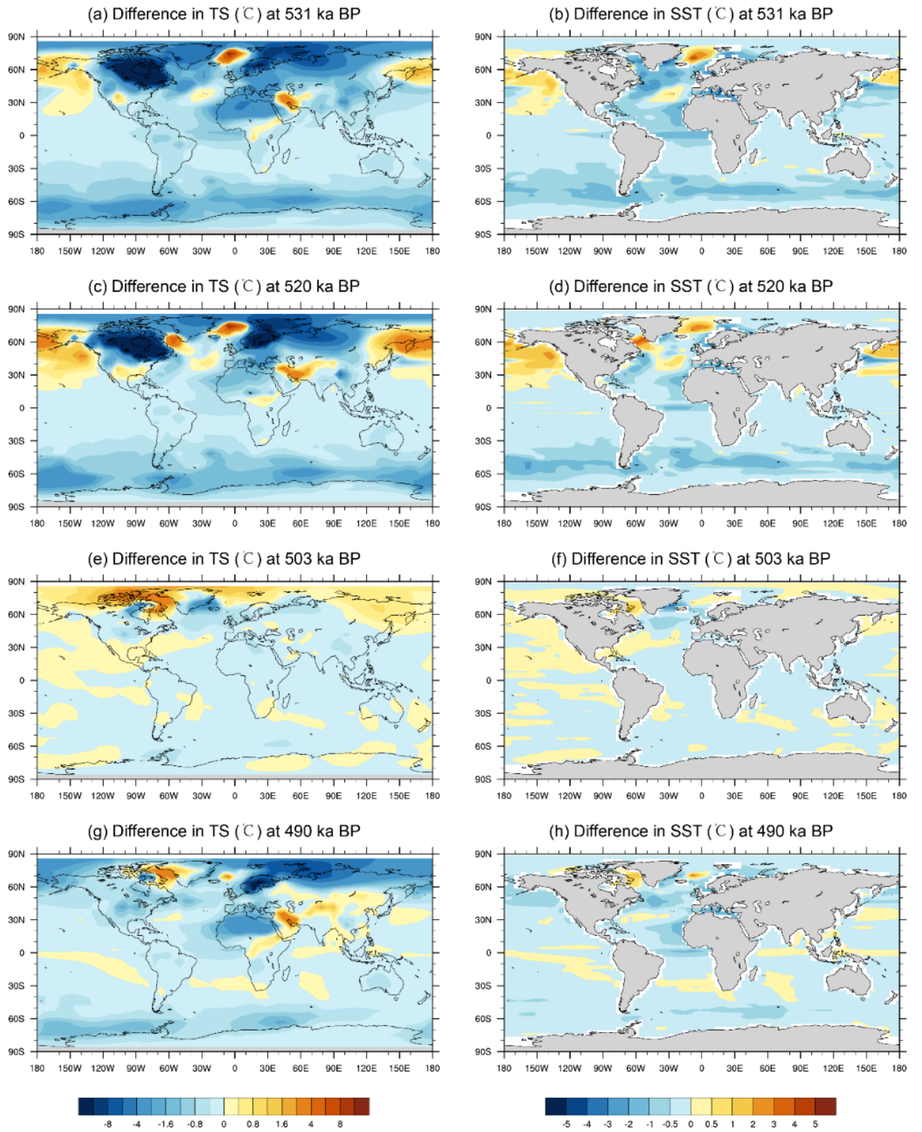

Figure 5.8 The effect of the NH ice sheets on the annual mean TS (left) and SST (right). The difference in TS and SST between the OrbGHGICE and OrbGHG experiments are shown for 531 ka BP (a, b), 520 ka BP (c, d), 503 ka BP (e, f) and 490 ka BP (g, h).

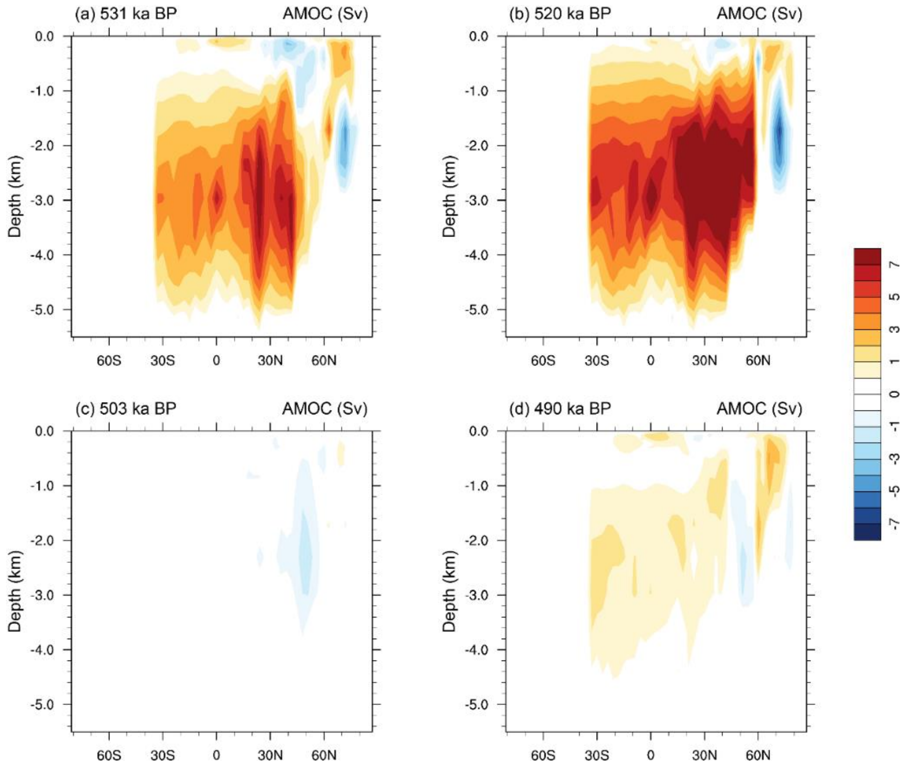

Figure 5.9 The effect of the NH ice sheets on the Atlantic meridional streamfunction. The difference between the OrbGHGICE and OrbGHG experiments are shown for 531 ka BP (a), 520 ka BP (b), 503 ka BP (c) and 490 ka BP (d).

Figure 5.10 shows the effect of NH ice sheets on SST at different latitudinal bands of both hemispheres. During MIS-13, the variations of the SST at the NH mid-high latitudes are nearly opposite to the variations of the Arctic sea ice area, so their relationship with the NH ice volume also appears complex and nonlinear, while the SST changes at the SH mid-high latitudes are highly and negatively correlated with the NH ice volume, like what has been observed for the sea ice. The SST response at low latitudes is similar to that in the mid-high latitudes of the same hemisphere, but their amplitude is smaller (Figure 5.10).

In order to discuss the effect of the NH ice sheets on the spatial changes of SST, the four selected dates mentioned above are also used to analyze the SST changes. The results (Figure 5.8) show that the SST changes over the Arctic are well negatively correlated with the Arctic sea ice changes, with higher SST corresponding to less sea ice. In general, the NH ice sheets lead to a cooling in the SH mid-high latitudes, and the strength of the cooling is positively correlated with the NH ice volume. For example, the cooling in the SH mid-high latitudes is stronger at 531and 520 ka BP than at 503 and 490 ka BP (Figure 5.8) due to the larger NH ice volume in the former dates. The spatial response of SST at low latitudes are more complex (Figure 5.8), and is probably related not only to the direct influence of ice sheets but also to the ice sheet-induced changes in the tropical precipitation which could also affect SST. This will be further investigated in future study especially with the help of sensitivity experiments using a more complex GCM.

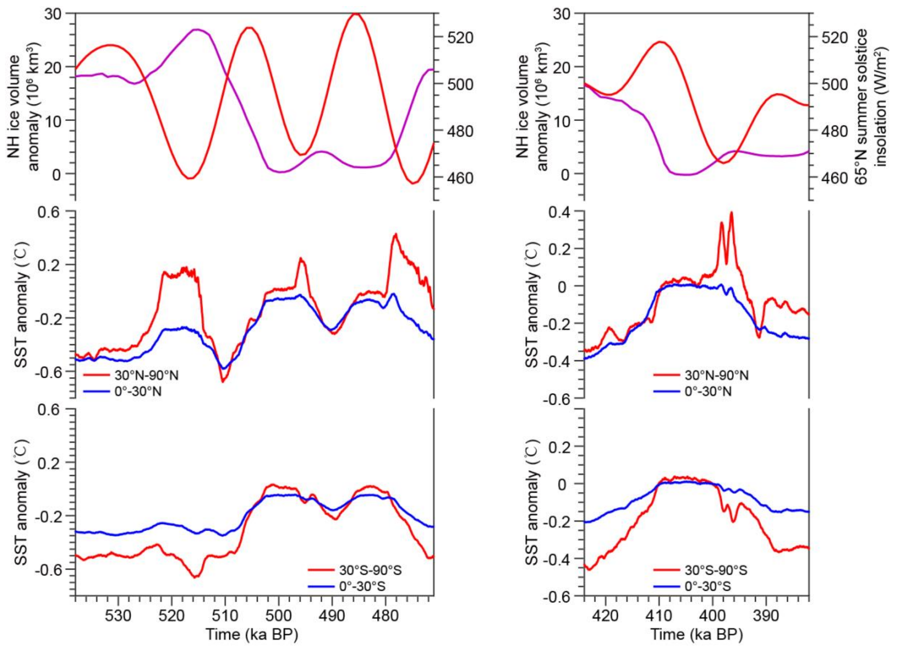

Figure 5.10 The effect of NH ice sheets on the annual mean SST at different latitudinal bands during MIS-13 (left) and MIS-11 (right). The SST anomaly represents the SST difference between the OrbGHGICE and OrbGHG experiments.

5.5 The relative importance of insolation, CO_2 and NH ice sheets on sea ice and SST

To investigate the relative importance of insolation, CO_2 and NH ice sheets on sea ice, the results of OrbGHGICE experiments which reflect the total effect of insolation, CO_2 and NH ice sheets, are compared with the results of Orb experiments which reflect the effect of insolation alone, with the effect of CO_2 (OrbGHG - Orb), and with the effect of NH ice sheets (OrbGHGICE - OrbGHG) (Figure 5.11). For the Arctic sea ice area, the result of Orb experiment is the most similar with the result of OrbGHGICE experiment during MIS-13 (correlation coefficient R^2=0.79), showing that insolation plays a primary role on the variability of the Arctic sea ice area. For the Southern Ocean sea ice area, the effect of NH ice sheets is the most similar with the result of OrbGHGICE experiment during MIS-13 (Figure 5.11) (correlation coefficient R^2=0.91), showing that NH ice sheets play a dominant role on the variability of the Southern Ocean sea ice area. Similar results are found for MIS-11 (Figure 5.11). These results are in good agreement with the proxy records that the variations of Arctic sea ice show strong precession cycles and they are dominated by insolation (Lo et al., 2018; Cronin et al., 2013), and the variations of Southern Ocean sea ice show strong glacial-interglacial cycles (Wolff et al., 2006).

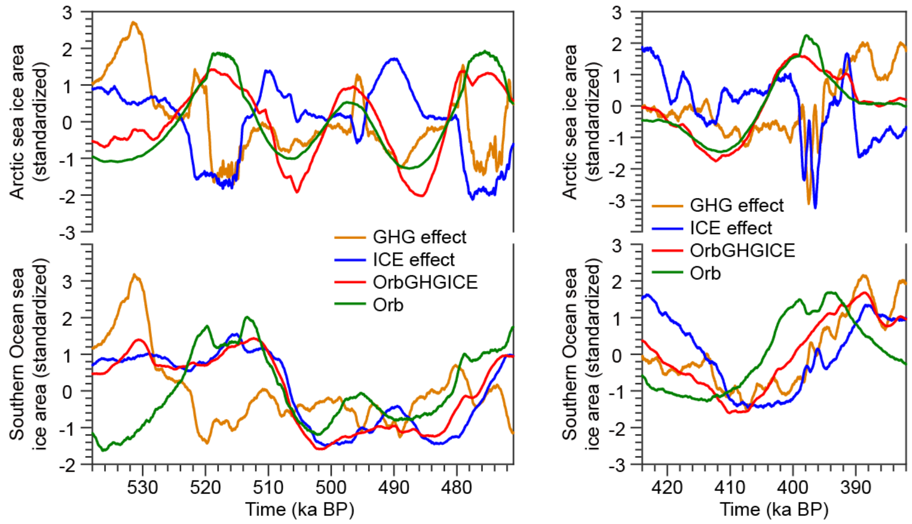

Figure 5.11 The individual and combined effects of insolation, CO_2 and NH ice sheets on the Arctic and Southern Ocean sea ice area during MIS-13 (left) and MIS-11 (right). The red lines are the results of the OrbGHGICE experiments and reflect the total effect of insolation, CO_2 and NH ice sheets; the green lines are the results of the Orb experiments and reflect the effect of insolation alone; the yellow lines are the difference between the OrbGHG and Orb experiments and reflect the effect of CO_2; and the blue lines are the difference between the OrbGHGICE and OrbGHG experiments and reflect the effect of NH ice sheets.

For the SST at the NH mid-high latitudes, the result of the Orb experiment is the most similar with the result of the OrbGHGICE experiment during MIS-13 (Figure 5.12) (correlation coefficient R^2=0.57), showing that insolation plays a primary role on the variations of SST at the NH mid-high latitudes, which are similar with the results of the Arctic sea ice area. For the SST at low latitudes of both hemispheres, both the effect of CO_2 and the effect of NH ice sheets are similar with the result of OrbGHGICE experiment (Figure 5.12), showing that both CO_2 and NH ice sheets play an important role in the variations of SST at low latitudes. For the SST at the SH mid-high latitudes, the effect of NH ice sheets is the most similar with the result of the OrbGHGICE experiment (Figure 5.12) (correlation coefficient R^2=0.86), showing that NH ice sheets play a dominant role on the variations of SST at the SH mid-high latitudes, similar to what is observed for the Southern Ocean sea ice area. During MIS-11, the results of the relative importance of insolation, CO_2 and NH ice sheets on SST at different latitudinal bands are similar with the results during MIS-13.

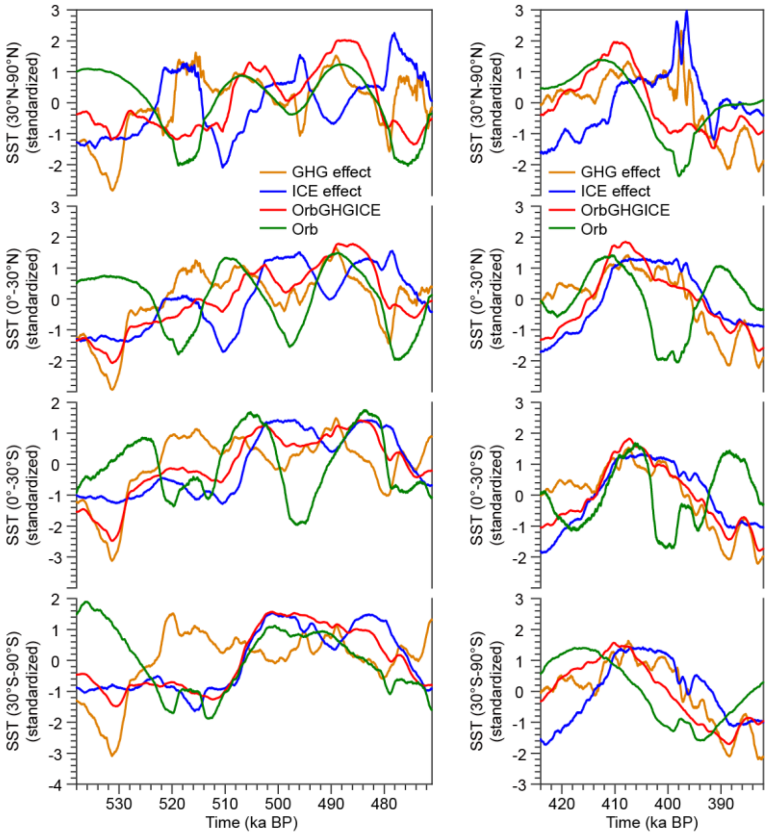

Figure 5.12 The individual and combined effects of insolation, CO_2 and NH ice sheets on the SST at different latitudinal bands during MIS-13 (left) and MIS-11 (right). The red lines are the results of the OrbGHGICE experiments and reflect the total effect of insolation, CO_2 and NH ice sheets; the green lines are the results of the Orb experiments and reflect the effect of insolation alone; the yellow lines are the difference between the OrbGHG and Orb experiments and reflect the effect of CO_2; and the blue lines are the difference between the OrbGHGICE and OrbGHG experiments and reflect the effect of NH ice sheets.

5.6 Comparison between simulated sea ice and SST with proxy records

To evaluate the simulated results, the simulated sea ice and SST of the OrbGHGICE experiments are compared with geological records. As the reconstructed Arctic sea ice is usually of short-duration and low-resolution, it is hard to find suitable proxy records to compare with the simulated Arctic sea ice of the last nine interglacials. The sea ice reconstruction in the central Okhotsk Sea over the last 130 ka show that it is dominated by precession (Lo et al., 2018), which is in line with our simulated results. The reconstructed Southern Ocean sea ice based on the ssNa flux from Antarctic ice core spanning last eight glacial cycles (Wolff et al., 2006) is also used here to compare with our simulated Southern Ocean sea ice. The results show that this comparison is quite good over the last eight simulated periods (Figure 5.13), showing the good ability of LOVECLIM in simulating the Southern Ocean sea ice at orbital timescale.

As far as SST is concerned, four high-resolution proxy records from low latitudes, NH mid-high latitudes and SH mid-high latitudes are compared with our simulated results (Figure 5.14). In terms of the variation pattern, the reconstruced and simulated SST have a good consistence, especially over the last 400 ka. However, the magnitude of SST changes in our simulations is lower than in the reconstructions. There are also other discrepancies. For example, the simulated SST at SH mid-high latitudes show stronger precession signals than the reconstruction. These discrepancies between the simulations and reconstructions could be related to uncertainties in both simulations and proxy records and will be better investigated in the future.

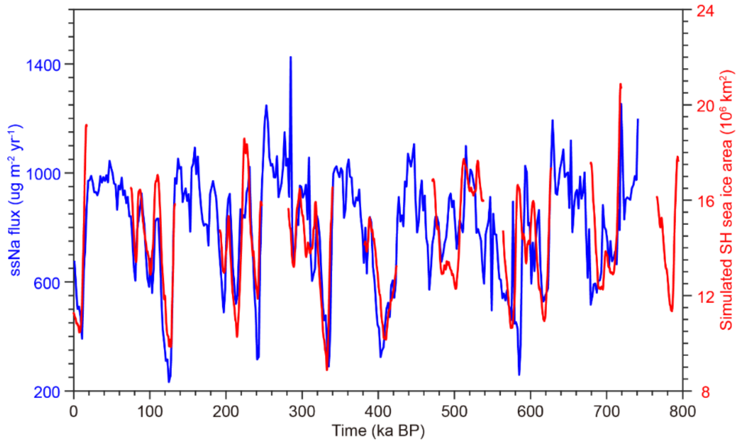

Figure 5.13 Comparison of simulated Southern Ocean sea ice of the OrbGHGICE experiments (red lines) with the reconstruction (blue lines) based on the ssNa flux from Antarctic ice core (Wolff et al., 2006).

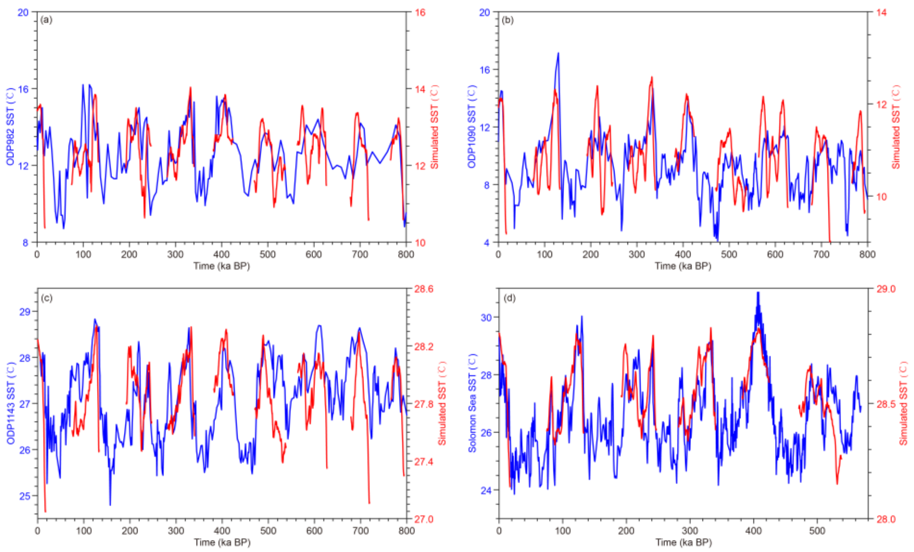

Figure 5.14 Comparison of simulated SST of the OrbGHGICE experiments (red lines) with proxy-reconstructed SST (blue lines) (a) at ODP 982 (57.5°N, 15.9°W, Lawrence et al., 2009), (b) at ODP 1090 (42.9°S, 8.9°E, Martínez-Garcia et al., 2010), (c) at ODP 1143 (9.4°N, 113.3°E, Li et al., 2011) and (d) in the Solomon Sea (9.3°S, 151°E, Lo et al., 2022).

5.7 Conclusions

In this chapter, three transient simulations were performed for each of MIS-13 and MIS-11 to investigate the different response of sea ice and SST to astronomical parameters, CO_2 and NH ice sheets.

The results show that the response of sea ice and SST is different between the two hemispheres. Under the combined effect of insolation, CO_2 and NH ice sheets, the variations of the Arctic sea ice area are dominated by insolation, while the NH ice sheets play a dominant role in the variations of the Southern Ocean sea ice area. In terms of the astronomical parameters, precession is more important role in the Arctic sea ice area, while obliquity is more important in the Southern Ocean sea ice area. CO_2 plays a more important role in the Southern Ocean sea ice area than in the Arctic sea ice area. When the effect of NH ice sheets is considered, the response of the Southern Ocean sea ice is highly and positively correlated with the variations of the NH ice volume, but the response of the Arctic sea ice to NH ice sheets is more complex and appears nonlinear. It depends on the NH summer insolation as well as the ice sheet size and distribution.

The response of SST at mid-high latitudes in the NH and SH to astronomical parameters, CO_2 and NH ice sheets is very similar with the results of the Arctic and Southern Ocean sea ice area respectively. The annual SST at low latitudes of the two hemispheres is mainly controlled by CO_2 and the NH ice sheets. In terms of the astronomical parameters, it is dominated by precession.

Chapter 6 The half-precession signals during the Quaternary

6.1 Introduction

Earth's climate has experienced co-evolution and interactions of orbital and sub-orbital timescale climate variations during the Quaternary based on numerous proxy records and numerical simulations (e.g. Rutherford and D'Hondt, 2000; Guo et al., 2012; Cheng et al., 2016; Hodell et al., 2015; Sun et al., 2021a; Yin et al., 2021). Sub-orbital timescale climate variations have received increasing attention, including their forcing mechanisms, internal processes and feedbacks, due to their more direct linkage with our future (e.g. Tzedakis et al., 2018; Galaasen et al., 2020). However, the understanding about the climate variations on sub-orbital timescale is far less than those on orbital timescale, which is partly due to the lack of linear forcing mechanisms to directly explain these sub-orbital timescale climate variations (Tuenter et al., 2007).

Among different sub-orbital timescale climate variations, the variations characterized by a periodicity near ~10 ka, also called the half-precession cycle, receive more attention. This is mainly because: (1) the climate variations with half-precession cycles could be directly linked with the maximum insolation near the Equator (Berger and Loutre, 1997; Berger et al., 2006); (2) the Dansgaard-Oeschger (DO) events are amplitude-modulated by half-precession cycles (Hinnov et al., 2002; Deng et al., 2018); (3) both proxy records and numerical simulations suggested that half-precession cycles play a critical role in explaining the high amplitude variations of the "100-kyr world" (Rutherford and D'Hondt, 2000; Le Treut and Ghil, 1983; Berger et al., 2006); (4) the half-precession signals are normally originated from the tropics (Berger et al., 2006; Ashkenazy and Gildor, 2008) and can be transported to mid and high latitudes through atmospheric and oceanic circulations (Hernández-Almeida et al., 2012; Ferretti et al., 2010, 2015). Therefore, a better understanding of the climate variations with half-precession cycles would be the first step to investigate the sub-orbital timescale climate variations, and is helpful for disentangling other climate events like DO oscillations and mid-Pleistocene climate transition, and could provide a more comprehensive picture of the role of low latitudes in the global climate changes and the interaction between high and low latitudes (Wang et al., 2014, 2017).

The half-precession cycles have been found in different proxy records, like marine sediments (Weirauch et al., 2008; Billups and Scheinwald, 2014), lake sediments (Trauth et al., 2003; Ulfers et al., 2022), ice cores (Guo et al., 2012), loess (Sun and Huang, 2006) and vegetation (Turney et al., 2004). However, the spatial and temporal characteristics of the half-precession cycles are still unclear, due to the lack of a compilation for the global half-precession signals. On the other hand, four possible forcing mechanisms have been proposed to explain the half-precession signals: (1) the maximum insolation near the Equator; (2) the bi-hemisphere insolation in the low latitudes; (3) the combination tones of the orbital cycles due to a nonlinear climatic oscillator; and (4) the internal processes and feedbacks in response to precession. However, they are often not easy to be distinguished mainly due to the interactions of different climate components. For example, different mechanisms, either the maximum equatorial insolation or the bi-hemispheric insolation, have been proposed by different researchers to explain the half-precession cycles in the hydrological changes in equatorial East Africa (Trauth et al., 2003; Verschuren et al., 2009) and in the CH_4 concentration recorded in the ice cores (Delmote et al., 2004; Guo et al., 2012). The half-precession cycles found in the mid and high latitudes have been proposed by some researchers to be related to the maximum equatorial insolation either via its more direct control on oceanic and atmospheric circulations (Ferretti et al., 2010, 2015) or via its indirect influence on the polar ice sheets (Hernández-Almeida et al., 2012), while they are also proposed to originate from the high latitudes themselves (Wara et al., 2000; Hodell and Channell, 2016). Moreover, the conditions that are favorable for the half-precession cycles could vary between proxy records. Therefore, the forcing mechanisms of the half-precession cycles and internal processes and feedbacks involved are still controversial.

To have a better understanding about the half-precession cycles, this Chapter intends to comprehensively and systematically investigate the half-precession signals based on both proxy records and numerical simulations. In order to investigate the spatial and temporal characteristics of the half-precession signals, a compilation of available published Quaternary proxy records which contain clear half-precession cycles has been completed, and seven classic proxy records of high resolution and long duration over the last 800 ka are analyzed using our method. In addition, some forcing mechanisms of the half-precession signals, as well as the effect of the astronomical parameters, GHG and NH ice sheets on the half-precession signals, are investigated with the LOVECLIM1.3 simulations. All the time series analysis performed in this study is made by using the Morlet software package (Melice and Servain, 2003).

6.2 The first compilation of the half-precession signals during the Quaternary

To investigate the spatial characteristics of the half-precession signals during the Quaternary, we compiled as many as possible available proxy records from publications where the authors have clearly identified the half-precession signals (Figure 6.1). Based on the different forcing mechanisms mentioned above, these records are divided into five groups, and each group is described as below.

6.2.1 Maximum insolation near the Equator

In the inter-tropical regions, the Sun passes overhead twice a year at each latitude. Particularly at the Equator, the Sun culminates at the zenith at both equinoxes. Therefore, the Earth can receive the maximum insolation twice during one precession cycle when both spring and autumn equinoxes occur at the perihelion (Berger and Loutre, 1997; Berger et al., 2006; Ashkenazy and Gildor, 2008). If the climatic proxies directly or indirectly respond to the maximum insolation, the half-precession signals could be recorded in them. Moreover, the half-precession signals could be transported from tropics to mid and high latitudes by atmospheric and oceanic circulations (Hernández-Almeida et al., 2012; Ferretti et al., 2010, 2015).

In response to the maximum insolation in the inter-tropics, the half-precession signals have been recorded in a number of proxy records, from low to high latitudes (red dots in Figure 6.1). In equatorial East Africa, the hydrological changes well followed maximum equatorial insolation in March or September, with half-precession cycles (Trauth et al., 2003). The hydrological changes with half-precession cycles were recorded in the precipitation variations (Ologa et al., 2000; Duesing et al., 2021a, 2021b; Trauth et al., 2021) and in the lake-level fluctuations (Thevenon et al., 2004; Trauth et al., 2003). The El Niño-Southern Oscillation (ENSO) is a significant feature in the tropical air-sea interaction, and it has a great effect on the global climate changes. The long-term ENSO variability is mainly controlled by the timing of the perihelion, the 'warm' ENSO events are expected to occur with a half-precession cycle when the perihelion is in either the boreal spring or autumn (Turney et al., 2004). The half-precession signals in the paleo-ENSO variations have been confirmed by many proxy records from tropics (Thevenon et al., 2004; Turney et al., 2004; Li et al., 2011; Tang et al., 2013). In addition, South China Sea (SCS) is another critical region to investigate the role of low-latitude processes in global climate changes (Wang et al., 2003) and the evolution of tropical monsoons (Tian and Wang, 2006). Under the influence of the maximum equatorial insolation, the tropical monsoon also varies with strong half-precession cycles (Tian and Wang, 2006). The half-precession signals in the tropical monsoon have been detected in various proxy records in the SCS (Tian et al., 2004; Sun et al., 2003; Luo et al., 2005; Wei et al., 2006, 2007; Liu et al., 2007; Chen et al., 2008). Adjacent to the SCS, the half-precession signals have also been found in many proxy records which reflect the East Asian monsoon variations (Wang et al., 2021; Sun and Huang, 2005; Beaufort et al., 2003).

The Atlantic is one of the most important regions in the global climate changes due to its role in the redistribution of global heat and water (Clark et al., 2002). In response to the maximum equatorial insolation, the half-precession signals have been recorded in numerous proxy records in the equatorial Atlantic (Pokras and Mix, 1987; McIntyre and Molfino, 1996; Berger and Loutre, 1997; Venancio et al., 2018; Nascimento et al., 2021). The half-precession signals can also be transported to mid and high latitudes in the Atlantic Basin through atmospheric or/and oceanic circulations (Ferretti et al., 2010, 2015; Emanuele et al., 2015; Amore et al., 2012; Palumbo et al., 2013, 2019; Martínez-Sánchez et al., 2019; Hernández-Almeida et al., 2012; Martínez-Sánchez et al., 2019). Beside the Atlantic, the half-precession signals have also been found in the Indian Ocean (Bolton et al., 2013) and in the Pacific Ocean (Haneda et al., 2020), as well as in the Antarctic Vostok ice core (Delmotte et al., 2004).

Not only proxy records, numerical simulations also support that the half-precession signals could be recorded in the surface air temperature (SAT), SST, precipitation and vegetation in the tropics in response to the maximum equatorial insolation by various models (Short et al., 1991; Laepple and Lohmann, 2009; Wu et al., 2020; Su et al., 2022).

6.2.2 Bi-hemispheric insolation in the low latitudes

Apart from the maximum insolation near the Equator, another way to produce half-precession signals is the combined effect of insolation at low latitudes of Northern and Southern Hemispheres (bi-hemispheric insolation at low latitudes) (Rutherford and D’Hondt, 2000; Guo et al., 2012). The daily insolation in the low latitudes is mainly controlled by precession, and their local summer insolation are anti-phase in the two hemispheres in relation to precession (Berger, 1978). If the climatic proxies are under the effect of the bi-hemisphere insolation in the low latitudes, the half-precession signals could be recorded in them (blue dots in Figure 6.1).

Under the influence of the bi-hemisphere insolation in the low latitudes, the half-precession signals have been recorded in various proxy records in the Atlantic and Pacific Ocean (Hagelberg et al., 1994; Chapman and Shackleton, 1998; Jian et al., 2020). Differing from the forcing mechanism of the maximum equatorial insolation as discussed above, some studies proposed that the half-precession signals in the proxy records which reflect the tropical monsoon variations, are originated from the bi-hemisphere insolation in the low latitudes (Verschuren et al., 2009; Ivory et al., 2016; Lupien et al., 2021; Guo et al., 2012). Actually, these two forcing mechanisms for the half-precession signals discussed above are not easy to be distinguished, because both of them are originated from low latitudes and the age uncertainty of the proxy records is usually too large to allow distinguish the two mechanisms (Rutherford and D’Hondt, 2000). Therefore, some studies only deduced that the half-precession signals in their proxy records (green dots in Figure 6.1) are resulted from low latitudes, either the maximum equatorial insolation or the bi-hemisphere insolation in the low latitudes (Chaisson et al., 2002; Grützner et al., 2002; Hall and Becker, 2007; Weirauch et al., 2008; Billups and Scheinwald, 2014; Billups et al., 2016; Grützner et al., 2002; Billups et al., 2011; Rutherford and D’Hondt, 2000).

6.2.3 Combination tones of the orbital cycles--a nonlinear climatic oscillator

Besides the tropical forcing mechanisms discussed above, the half-precession signals can also be explained by the combination tones of the orbital cycles due to a nonlinear climatic oscillator (Berger and Loutre, 1997). Due to the phase difference in different components of the climate system, such as insolation and ice sheets, a large number of different periodic signals can be produced under the combined effect of different climate system components, including the half-precession signals (Guo et al., 2012). These half-precession signals can be originated from high latitudes themselves or from the interactions between high and low latitudes. If the climatic proxies are sensitive to the influence of different climate components with phase difference, the half-precession signals may be recorded in them (yellow dots in Figure 6.1, Pestiaux et al., 1988; Mommersteeg et al., 1995; Ortiz et al., 1999; Wara et al., 2000; Hodell et al., 2013; Hodell and Channell, 2016; Zhao et al., 2020; Lindberg et al., 2021). In addition, numerical simulations also support that the half-precession signals could be originated from the combination tones of the orbital cycles (Le Treut et al., 1988; Thomas et al., 2016).

6.2.4 Internal processes and feedbacks in response to precession

In addition to external forcings, the half-precession signals could also be produced by the internal processes and feedbacks. For example, if the climatic proxies are sensitive to both precession minimum and precession maximum, the half-precession signals could be recorded in them (purple dots in Figure 6.1; Heinrich, 1988). In addition, numerical simulations also shown that the half-precession signals could be produced in response to precession due to the internal processes and feedbacks, for instance, the ocean-atmosphere and vegetation feedbacks (Clement et al., 2001; Tuenter et al., 2007).

6.2.5 The forcing mechanisms are not clear

Although some possible forcing mechanisms have been proposed to explain the half-precession signals in the proxy records, the half-precession signals are still not well understood. Some studies detected the half-precession signals, but they could not provide any explanation (grey dots in Figure 6.1; van den Heuvel, 1966; Yiou et al., 1995; Mayewski et al., 1997; Gupta, 2002, 2003; Yu and Ding, 2003; Sümegi et al., 2019; Han et al., 2003, 2009; Hopley et al., 2007; Dang et al., 2020). Actually, these proxy records are normally of low-resolution and large age uncertainty. Thus, the half-precession signals in these proxy records should be considered with caution.

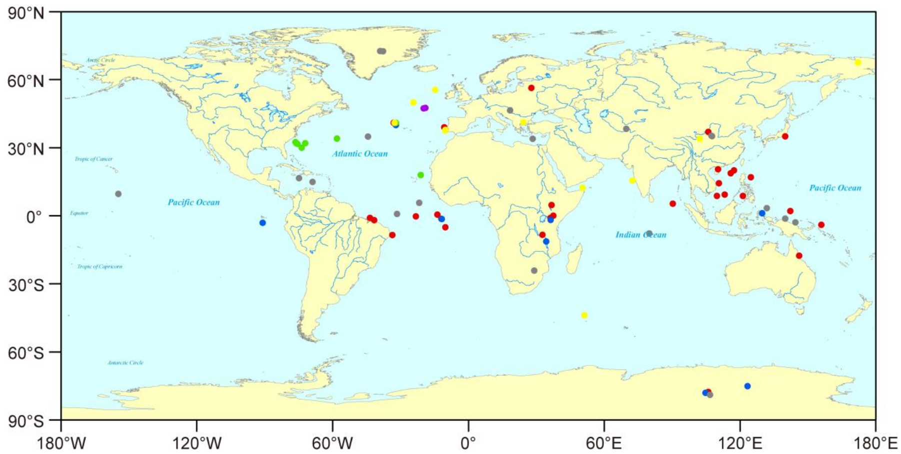

Figure 6.1 The compilation of the proxy records which contain clear half-precession signals. Based on different forcing mechanisms proposed by the authors above, they are divided into several groups. Red dots: maximum insolation near the Equator; blue dots: bi-hemispheric insolation in the low latitudes; green dots: the forcing mechanisms might be same as the red dots or blue dots; yellow dots: combination tones of orbital cycles--a nonlinear climatic oscillator; purple dots: internal processes and feedbacks response to precession; grey dots: the forcing mechanisms are not clear.

As discussed above and shown in Figure 6.1, the proxy records with half-precession signals are mainly concentrated in the tropics and Atlantic (about 90%). This partly reflects the important role of tropical insolation in explaining the half-precession signals recorded in proxy records, and also because the Atlantic is one of the focuses in paleoclimate study. Very few records have been found in the Indian Ocean, Eastern Pacific, Southern Ocean and Antarctic (less than five records for each region, totally less than 10%). This is most probably due to less study sites in general in these regions, but it can not exclude the possibility that half-precession signal is weak in these regions. More data and analyses would be needed for a better view, and on the other hand it also shows the necessity to explore the half-precession cycles with model simulations.

6.3 The half-precession signals over the past 800 ka

To further investigate whether the half-precession signals are persistent over the last 800 ka, we reanalyze seven published high-resolution climatic records. These seven proxy records are selected due to their high resolution (<0.4 ka), long duration (≥600 ka), and distributed from Greenland to Antarctica. From north to south, the information of these seven proxy records is briefly given below:

(1) GL_T_syn is an 800 ka synthetic record ($\delta^{18}O$) of Greenland climate variability based on the thermal bipolar seesaw model. Its average temporal resolution is 0.05 ka (Barker et al., 2011), and it could be used to represent temperature.
(2) IODP Site U1308 (49.88°N, 24.23°W) is located near the centre of the North Atlantic IRD belt. The average temporal resolution of the log(Si/Sr) ratio over the past 800 ka is about 0.16 ka (Hodell and Channell, 2016), and it could represent the relative content of detrital silicate minerals (IRD proxy).
(3) Lake Ohrid (41.03°N, 20.72°E) is located in the Mediterranean climate zone. The average temporal resolution of the Ca/K ratio over the past 800 ka is about 0.06 ka (Vogel et al., 2010), and it could represent the hydrological variations.
(4) IODP Site U1385 (37.57°N, 10.13°W) is located on the southwest Iberian margin. The average temporal resolution of the log(Ca/Ti) ratio over the past 800 ka is about 0.09 ka (Hodell et al., 2015), and it could represent the relative proportion of biogenic carbonate and detrital clay (precipitation or marine productivity).
(5) LGS640, a 640 ka loess grain-size stack, is generated by compositing three mean grain-size time series from the western Chinese Loess Plateau (CLP)--Gulang (GL, 37.49°N, 102.88°E), Linxia (LX, 35.15°N, 103.63°E) and Jingyuan (JY, 36.35°N, 104.62°E) sections. Its average temporal resolution is 0.10 ka (Sun et al., 2021b), and it could represent East Asian winter monsoon.
(6) The stalagmite $\delta^{18}O$ record over the last 640 ka are composited from three caves in eastern China--Sanbao Cave (31.67°N, 110.43°E), Hulu Cave (32.5°N, 119.17°E), and Dongge Cave (25.28°N,

108.08°E). Its average temporal resolution is about 0.08 ka (Cheng et al., 2016), and it could represent East Asian summer monsson.
(7) The CH_4 (Loulergue et al., 2008) record is reconstructed from the EDC ice core in Antarctica (75.1°S, 123.35°E). Its average temporal resolution is about 0.38 ka, and it could reflect a combined effect of glacial-interglacial cycles, monsoons in both hemispheres and the late Holocene human intervention (Guo et al., 2012).

Figure S6.1 shows the variations of these seven proxy records and their continuous wavelet transform results. In addition to the orbital cycles, all of them show abundant sub-orbital cycles, including the half-precession signals. However, we should keep in mind that these sub-orbital cycles could be affected by spectral artifacts which could be related to the following: 1) Windowing effects: when a finite-length window is applied to a signal prior to computing the power spectrum, it can cause leakage of energy from one frequency bin to another. This effect is known as spectral leakage and can result in the appearance of artificial peaks in the power spectrum. 2) Non-stationarity: power spectrum analysis assumes that the signal is stationary, meaning that its statistical properties are constant over time. If the signal is non-stationary, then the power spectrum may not accurately represent the frequency content of the signal. 3) Aliasing: aliasing occurs when a signal is sampled at too low a frequency, resulting in high-frequency content being aliased into lower frequency components. 4) Overfitting: power spectrum analysis can be sensitive to noise and can lead to overfitting if too many frequency components are included in the analysis. On the other hand, the seven selected records were widely used to investigate the sub-orbital timescale climate variations and half-precession cycles have been identified by the authors. For example, Guo et al. (2012) reanalyzed the CH_4 record over the last 800 ka using Singular Spectrum Analysis (SSA) and found the half-precession cycles. Zeng et al. (2019) reanalyzed the stalagmite $\delta^{18}O$ record over the last 640 ka and also found the half-precession cycles.

In order to better discuss the half-precession signals, a high-pass filter (<14 ka) is applied to remove the orbital signals in these records. After the orbital signals are removed, the residuals of these records show very strong half-precession signals (Figure 6.2, grey line). In addition, a band-pass filter (9-11 ka) was applied to extract the half-precession signals of their original data (Figure 6.2, blue line), and the filter results have a good coherence with the residuals of these records. Therefore, we deduce that the half-precession signals are real and robust in these records. However, the conditions that are favorable for the half-precession cycles could vary between proxy records. Strong half-precession cycles could occur mainly in interglacials for some records, but in both glacials and interglacials for the others (Figure 6.2), indicating different driving mechanisms. Indeed, the half-precession signals in Lake Ohrid were proposed to originate from the maximum equatorial insolation (Ulfers et al., 2022). The half-precession signals in the composited stalagmite $\delta^{18}O$ and in the CH_4 from the EDC ice core, both were thought to be linked with tropical monsoon variations, could be a response to bi-hemispheric insolation changes (Guo et al., 2012; Zeng et al., 2019). The half-precession signals in the bulk carbonate $\delta^{18}O$ from North Atlantic core IODP U1308 were proposed to result from the combination tones of the orbital cycles (Hodell and Channell, 2016), and the Si/Sr ratio in the same core may have the same origination.

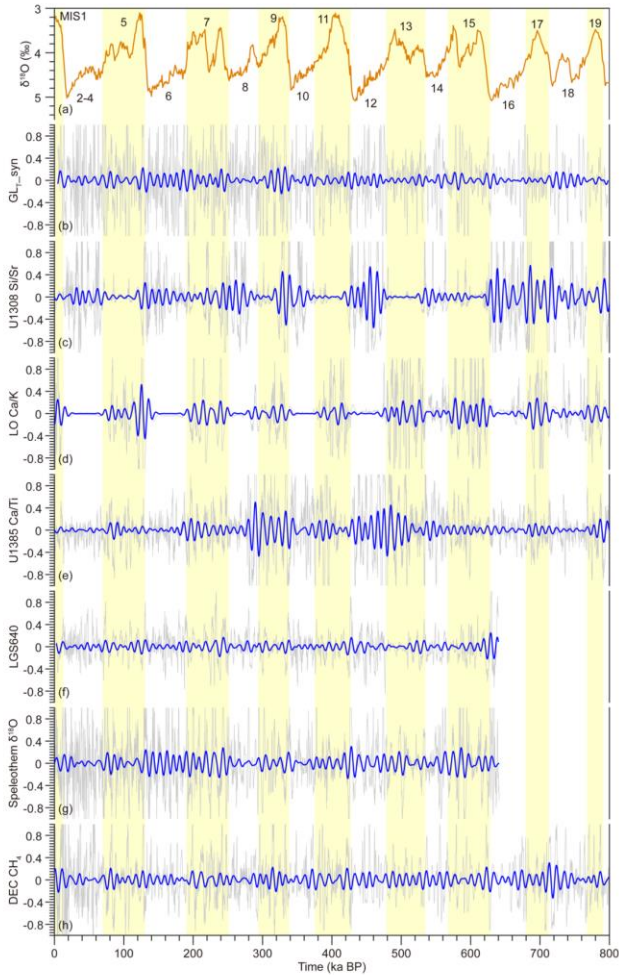

Figure 6.2 Variations of the seven selected high-resolution proxy records. (a) The benthic $\delta^{18}O$ record indicating the glacial-interglacial cycles (Lisiecki and Raymo, 2005). The numbers of MIS stages are indicated; the yellow shaded vertical bars indicate interglacial periods and non-shaded bars indicate glacial periods; (b) the Greenland synthetic $\delta^{18}O$ (Barker et al., 2011); (c) Si/Sr of IODP U1308 (Hodell et al., 2008); (d) Ca/K of Lake Ohrid sediment (Vogel et al., 2010); (e) Ca/Ti of IODP U1385 (Hodell et al., 2015); (f) loess grain-size stack (Sun et al., 2021b); (g) composited stalagmite $\delta^{18}O$ (Cheng et al., 2016); (h) DEC CH_4 (Loulergue et al., 2008). Grey lines represent the high-pass filter (<14 ka) results and the blue lines represent the band-pass filter (9-11 ka) results.

6.4 Simulated half-precession signals in LOVECLIM1.3

To further investigate the half-precession signals, especially their forcing mechanisms, we analyze the simulated results of three interglacials (MIS-11, MIS-13 and MIS-19) performed using the model LOVECLIM1.3. As discussed in Chapter 2, the simulated time periods actually include the part of the transitions of the glacial termination and inception before and after each interglacial. This leads to large amplitude variations of both CO_2 and ice sheets. For example, the CO_2 concentration varied between 190 ppmv and 253 ppmv (Lüthi et al., 2008), and the NH ice volume varied between 4.46 million km^3 to 30.12 million km^3 during MIS-13 (Ganopolski and Calov, 2011). In addition, in terms of the astronomical parameters, the amplitude variations of both precession and obliquity are large during MIS-13 and small during MIS-19, and the amplitude variation of precession is small while the amplitude variation of obliquity is large during MIS-11 (Berger and Loutre, 1991). Therefore, these allow to investigate the half-precession signals under a large range of astronomical parameters, CO_2 and NH ice sheets and under different background climate conditions.

As discussed in Section 6.2, the half-precession signals are mainly related to insolation and precession forcing, we first analyze the results of the simulation considering only varying insolation (the Orb experiment) during MIS-13. In order to investigate the effect of precession and obliquity on the half-precession signals, the results of the Orb experiments during MIS-19 and MIS-11 are also analyzed and compared with the results during MIS-13. To investigate the effects of GHG and NH ice sheets on the half-precession signals, the results of the OrbGHG and OrbGHGICE experiments of MIS-13 are also analyzed and compared with the results of the Orb experiment.

6.4.1 The half-precession signals in response to maximum equatorial insolation

As discussed above, the most popular forcing mechanism of the half-precession signals is the maximum equatorial insolation (Berger et al., 2006), so we first investigate this forcing mechanism in our simulated results. Figure 6.3 shows the variations of our simulated annual mean precipitation, surface air temperature (SAT) and sea surface temperature (SST) near the Equator (10°S-10°N) in the Orb experiment during MIS-13, all of them show clear half-precession cycles based on the results of continuous wavelet transform and even with the naked eyes. In addition, our simulated half-precession signals near the Equator have a good consistence with the proxy records (e.g. Olago et al. 2000; Trauth et al. 2021). In order to better understand these half-precession signals, Gaussian band pass filtering (9-11 ka) was applied to extract them (Figure 6.3c~6.3e, blue lines). The extracted half-precession signals show a good coherence with their original data (Figure 6.3c~6.3e, grey lines), further confirming the reliability and robustness of the half-precession signals. In addition, these half-precession signals are well consistent with the maximum equatorial insolation (Figure 6.3), indicating that they are the direct response to the maximum insolation at the Equator (Berger et al., 2006).

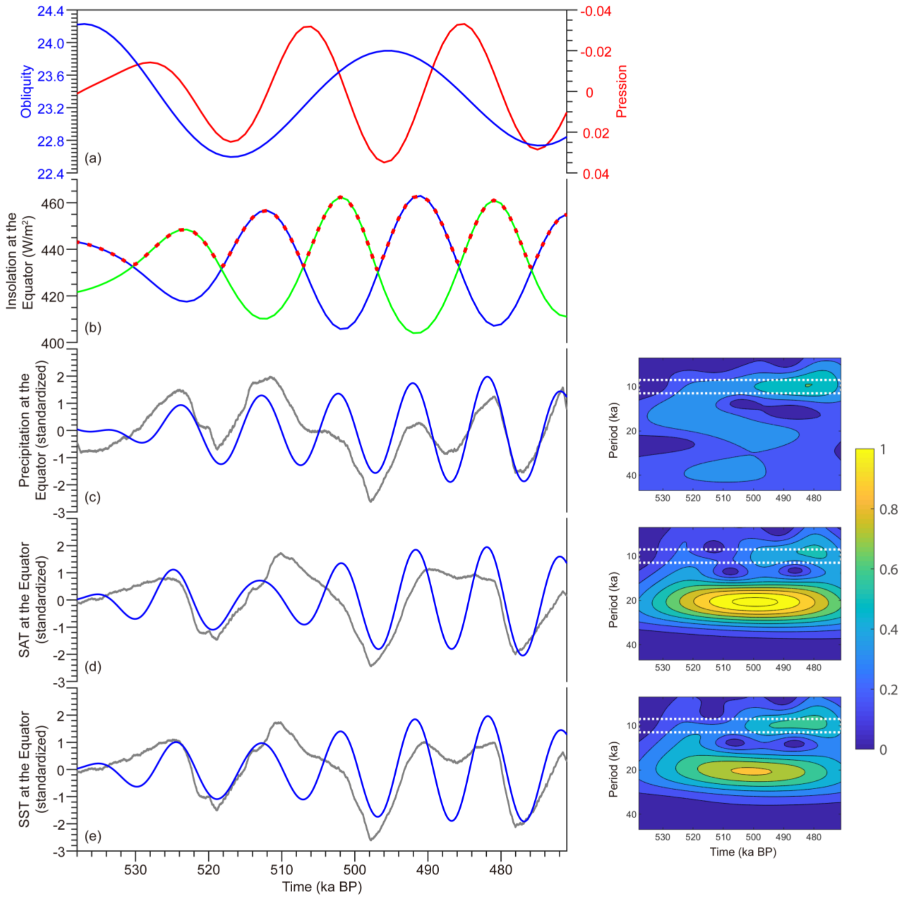

Figure 6.3 Variations of the annual mean precipitation, SAT and SST at the Equator (10°S-10°N) and their continuous wavelet transform results during MIS-13 in the Orb experiment. (a) obliquity (blue line) and precession (red line) (Berger and Loutre, 1991), (b) the maximum insolation at the Equator (blue: daily insolation at March equinox; green: daily insolation at September equinox; red dash: maximum of the March and September insolation) (Berger and Loutre, 1991), (c) annual mean precipitation, (d) annual mean SAT, and (e) annual mean SST. The grey lines represent the origin data (1000-year running mean), and the blue lines are the result of 9-11 ka filter. The figure on the right is the continuous wavelet transform of the origin data.

The half-precession signals in the tropics could also be transported to the mid and high latitudes through atmospheric and oceanic circulations (Hernández-Almeida et al., 2012; Ferretti et al., 2010, 2015). Indeed, our simulated annual mean precipitation, SAT and SST variations in the mid and high latitudes also contain half-precession signals although they are weaker than these in the tropics. If the orbital signals are removed using Gaussian high-pass filtering (<14 ka), the half-precession signals become strong and clear (Figure 6.4, grey lines). We also extract the half-precession signals (Figure 6.4, blue lines) using the Gaussian band-pass filter (9-11 ka) from the original data, and they have a good consistence with the maximum equatorial insolation. In addition, the variations of the annual mean meridional heat transport (MHT) at different latitudes in the Atlantic basin also contain the half-precession signals and they are also in line with the maximum equatorial insolation (Figure 6.5). Therefore, we can deduce that the half-precession signals in the precipitation, SAT and SST in the mid and high latitudes are resulted from the maximum equatorial insolation and transported via oceanic circulations.

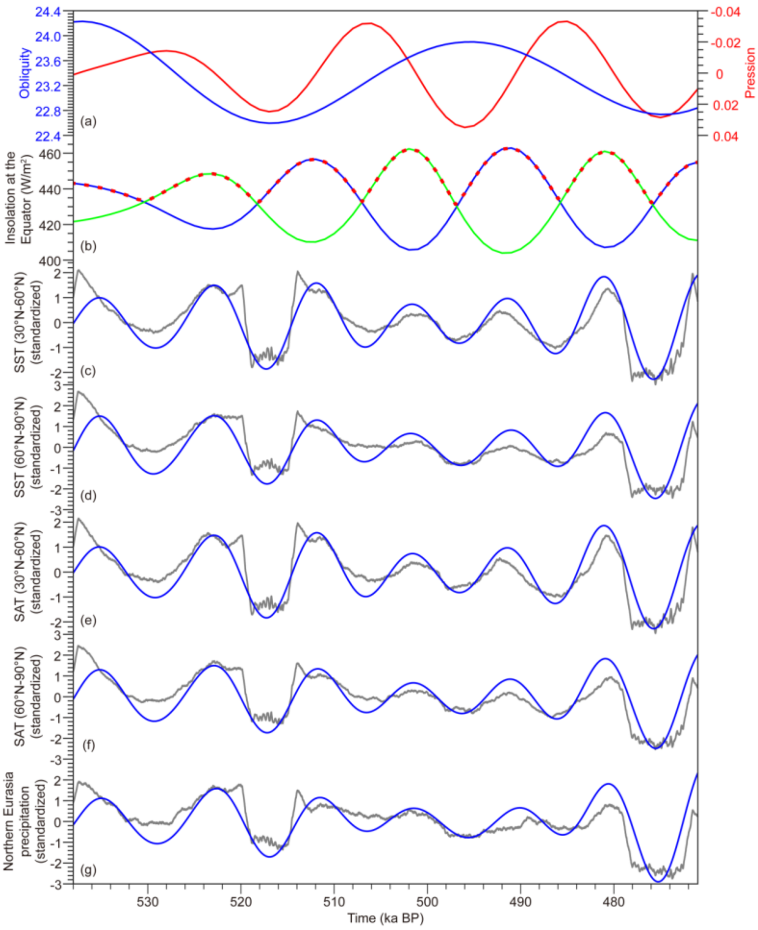

Figure 6.4 Variations of the annual mean precipitation, SAT and SST at mid and high latitudes. (a) Obliquity (blue line) and precession (red line) (Berger and Loutre, 1991), (b) the maximum insolation at the Equator (blue: daily insolation at March equinox; green: daily insolation at September equinox; red dash: maximum of the March and September insolation) (Berger and Loutre, 1991), (c) the annual mean SST at mid latitudes (30°N-60°N), (d) the annual mean SST at high latitudes (60°N-90°N), (e) the annual mean SAT at mid latitudes (30°N-60°N), (f) the annual mean SAT at high latitudes (60°N-90°N), (g) the annual mean precipitation in the Northern Eurasia (60°N-75°N, (0-180°E). The grey lines in (c-g) are the results of high-pass filter (<14 ka) and the blue lines in (c-g) are the results of band-pass filter (9-11 ka) from original data.

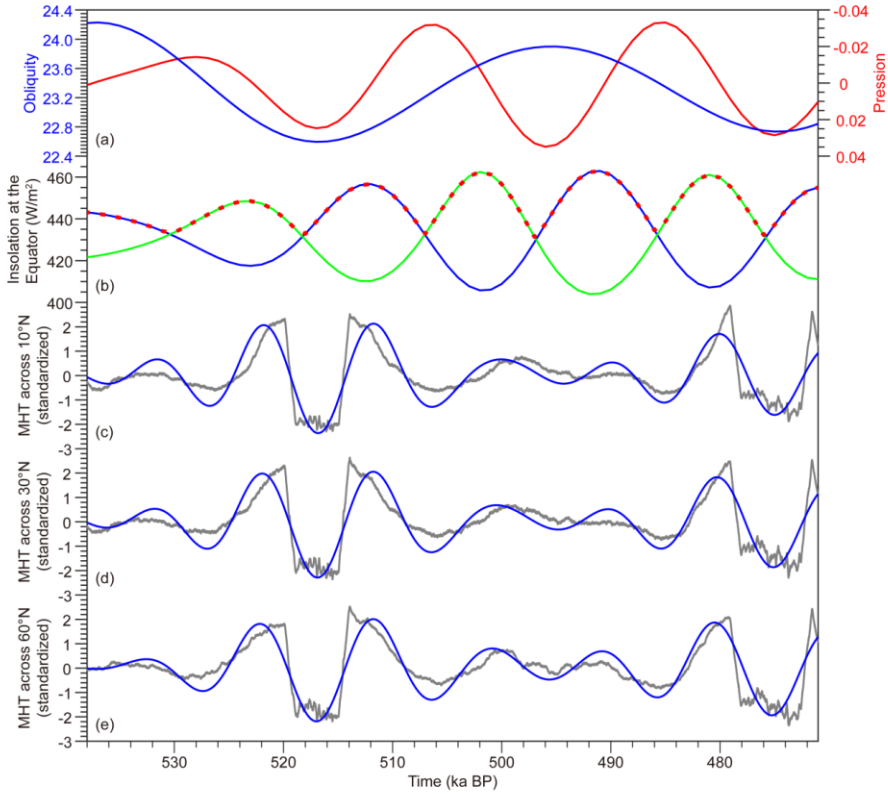

Figure 6.5 Variations of the annual mean MHT in the Atlantic basin. (a) Obliquity (blue line) and precession (red line) (Berger and Loutre, 1991), (b) the maximum insolation at the Equator (blue: daily insolation at March equinox; green: daily insolation at September equinox; red dash: maximum of the March and September insolation) (Berger and Loutre, 1991), the annual mean MHT in the Atlantic basin through (c) 10°N, (d) 30°N and (e) 60°N. The green lines in (c-e) are the results of high-pass filter (<14 ka), and the blue lines in (c-e) are the results of band-pass filter (9-11 ka) from original data.

To investigate the effect of precession and obliquity on the half-precession signals, the variations of the annual mean precipitation, SAT and SST at the Equator during MIS-19 and MIS-11 in the Orb experiments are also analyzed and compared with the results during MIS-13. The results (Figure 6.6) show that the half-precession signals become weaker during MIS-19 and even vanish during MIS-11. This is partly due to the fact that eccentricity is small leading to small variation of precession during MIS-19 and MIS-11, which would lead to a weak impact of precession and therefore a weak half-precession signal in the tropics. The difference of the half-precession signals during MIS-19 and MIS-11 is mainly due to the larger amplitude of variation of obliquity during MIS-11 which further suppresses the effect of precession and therefore the half-precession signals. The difference between these three interglacials shows that the half-precession signals are influenced by both precession and obliquity. Normally, large variation of precession would amplify the half-precession signals, while large variation of obliquity and small variation of precession would suppress the half-precession signals.

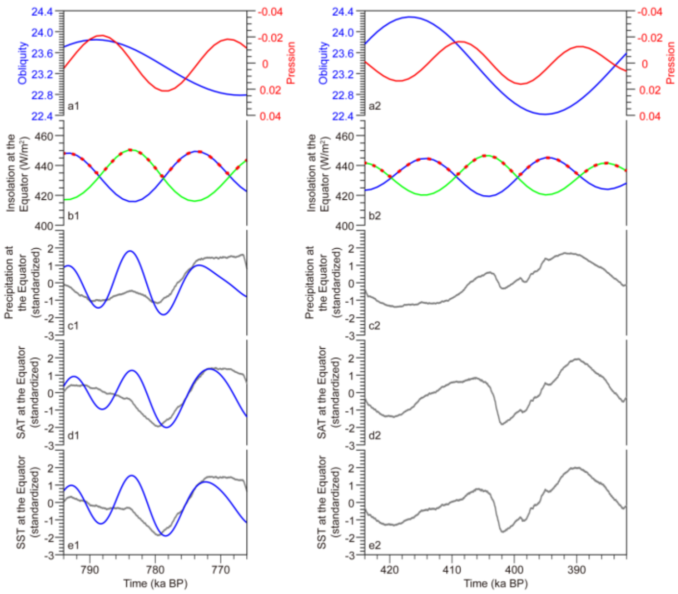

Figure 6.6 Variations of the annual mean precipitation, SAT and SST at the Equator (10°S-10°N) during MIS-19 and MIS-11 in the Orb experiment. (a1, a2) Obliquity (blue line) and precession (red line) (Berger and Loutre, 1991), (b1, b2) the maximum insolation at the Equator (blue: daily insolation at March equinox; green: daily insolation at September equinox; red dash: maximum of the March and September insolation) (Berger and Loutre, 1991), (c1, c2) annual mean precipitation, (d1, d2) annual mean SAT, and (e1, e2) annual mean SST. The grey lines represent the origin data (1000-year running mean), and the blue lines are the result of 9-11 ka filter.

To investigate the effects of GHG and NH ice sheets on the half-precession signals, the results of the OrbGHG and OrbGHGICE experiments during MIS-13 are also analyzed, and compared with the results of the Orb experiment. The results show that the half-precession signals of the annual mean precipitation, SAT and SST at the Equator in the OrbGHG experiment (Figure 6.7 and Figure S6.2) are weaker than those in the Orb experiment, and their relationship with the maximum equatorial insolation is not as good. These are mainly due to the influence of the long periodicity of CO_2, which would suppress the half-precession signals. Furthermore, if the effect of NH ice sheets is additionally taken in account, the half-precession signals are further weakened (Figure 6.7 and Figure S6.2) due to the influence of the long periodicity of NH ice sheets. This could also explain the stronger half-precession signals during interglacials than during glacials observed in some proxy records discussed above.

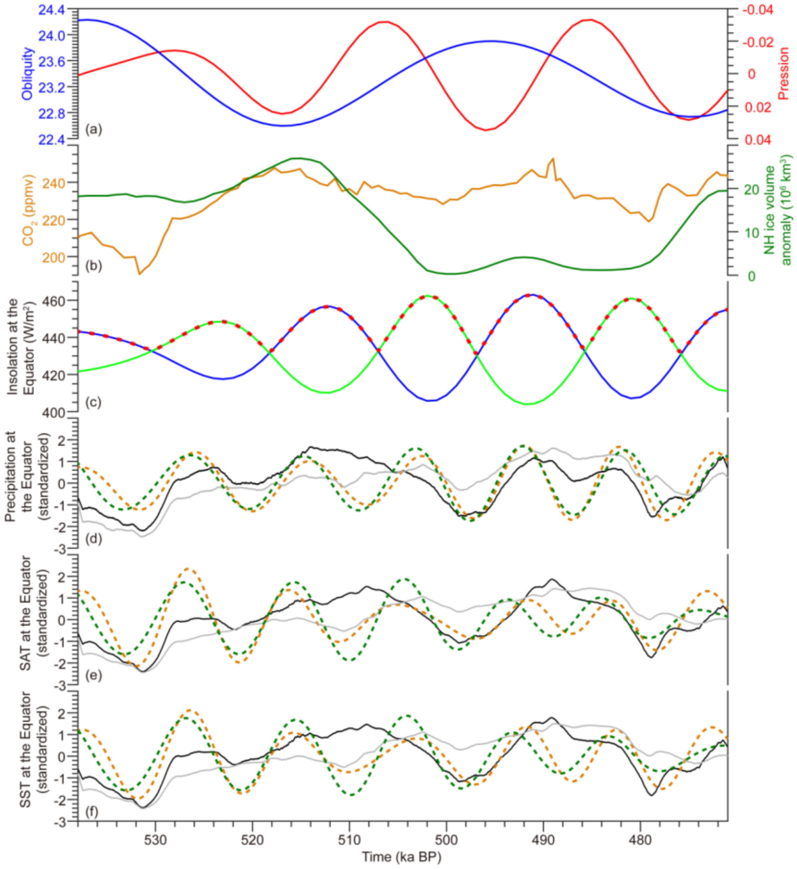

Figure 6.7 Variations of the annual mean precipitation, SAT and SST at the Equator (10°S-10°N) during MIS-13 in the OrbGHG and OrbGHGICE experiments. (a) Obliquity (blue line) and precession (red line) (Berger and Loutre, 1991), (b) the CO_2 concentration (yellow line, Lüthi et al., 2008) and NH ice volume anomaly as compared to the PI (dark green line, Ganopolski and Calov, 2011), (c) the maximum insolation at the Equator (blue: daily insolation at March equinox; green: daily insolation at September equinox; red dash: maximum of the March and September insolation) (Berger and Loutre, 1991), (d) annual mean precipitation, (e) annual mean SAT, and (f) annual mean SST. The black lines represent the origin data (1000-year running mean), and the dashed yellow lines are the result of 9-11 ka filter in the OrbGHG experiment; the grey lines represent the origin data (1000-year running mean), and the dashed dark green lines are the result of 9-11 ka filter in the OrbGHGICE experiment.

6.4.2 The half-precession signals in response to vegetation dynamics

In addition to external forcing mechanisms, the half-precession signals could also originate from the internal processes and feedbacks in response to precession forcing. Here we investigate the half-precession signals in the grass fraction, over the “African” and “Asian” monsoon regions which were defined by Tuenter et al. (2007), in response to vegetation dynamics. The grass fraction variations in these two regions are investigated mainly due to their sensitivity to the forcings, for example, the precipitation variations (Tuenter et al., 2007). Figure 6.8 shows the grass fraction variations in these two regions in the Orb experiment during MIS-13. The results show that both of them have clear half-precession cycles even with naked eyes, and each grass fraction minimum is related to both precession minimum and precession maximum (Figure 6.8). The half-precession signals in the grass fraction variations in these two regions could be explained below. In the low latitudes, the vegetation variations are mainly controlled by precipitation because the temperature is sufficiently high (Yin and Berger, 2012; Su et al., 2022). When precession is minimum (high NH summer insolation), it leads to more precipitation via strengthened monsoons, which enhances the development of trees at the expense of grass, so a precession minimum leads to a grass minimum; while when precession is maximum (low NH summer insolation), precipitation decreases due to weakened monsoons, which leads to desert expansion and the grass fraction is also reduced, so a precession maximum also leads to a grass minimum. These explain the half-precession cycles in the simulated grass variations. If the effects of precession and obliquity are considered, the results show that the half-precession signals in the grass fraction variations become weaker during MIS-19 and almost disappear during MIS-11 (Figure S6.3). In addition, if the effects of CO_2 and NH ice sheets are taken into account, the half-precession signals in the grass fraction would also be weakened due to the influence of their long periodicities (Figure S6.4). The effects of precession, obliquity, CO_2 and NH ice sheets on the half-precession signals in the grass fraction variations in these two regions are similar with their effects on the half-precession signals at the Equator as discussed in 6.4.1.

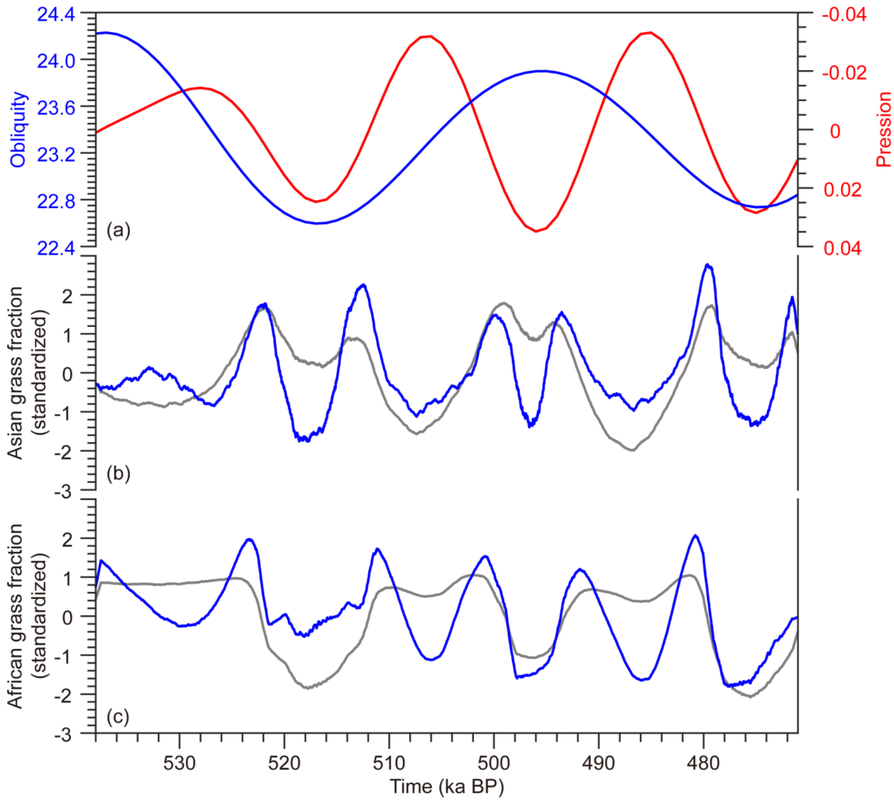

Figure 6.8 Variations of the annual mean grass fraction in the “Asian” and “African” monsoon regions in the Orb experiment during MIS-13. (a) obliquity (blue line) and precession (red line) (Berger and Loutre, 1991), (b) the annual mean grass fraction variations in the “Asian” monsoon region; the grey line is the origin data (1000-year running mean), and the blue line is the result of the high-pass filter (<14 ka), (c) is the same as (b), but for the “African” monsoon region.

6.5 Conclusions

In this study, the half-precession signals during the Quaternary are comprehensively and systematically studied based on both proxy records and transient simulations using the model LOVECLIM1.3.

To investigate the spatial and temporal characteristics of the half-precession signals, a first compilation of the half-precession signals during the Quaternary has been made. The results show that the proxy records that contain clear half-precession signals are mainly concentrated on the tropics and North Atlantic, and the most popular forcing mechanism is the maximum equatorial insolation. In addition, based on the reanalyzed results of seven high-resolution and long-duration records from Arctic to Antarctic, we further confirm that the half-precession signals are persistent at least over the last 800 ka, although they show some differences between different time periods and different climatic variables in different regions.

Our simulated results show that, in response to maximum equatorial insolation, the half-precession signals could be recorded in different climatic variables near the Equator, like precipitation, SAT and SST. In addition, the half-precession signals in the low latitudes can be transported to mid and high latitudes through atmospheric and oceanic circulations. Besides the external forcing mechanisms, the half-precession signals could also result from the internal processes and feedbacks, like the vegetation dynamics. It is worth noting that our simulated SST and subsurface sea temperature in the western equatorial Pacific also contain clear half-precession cycles. As these temperatures are strongly linked with ENSO, we might expect half-precession cycles also in ENSO, which could be tested with suitable ENSO proxies and climate models which have a good representation of ENSO.

In terms of the effects of different forcings on the half-precession signals, large variation of precession would amplify the half-precession signals, while large variation of obliquity would suppress them. In addition, the half-precession signals would be suppressed if the effects of GHG and ice sheets are taken into account due to the influence of their long periodicities. As mentioned earlier in this chapter, four forcing mechanisms were proposed by different authors for the half-precession cycles. Two, the maximum equatorial insolation and vegetation feedback, have been confirmed by our simulated results. To further better understand the half-precession signals, more high-resolution proxy records and transient simulations including ice sheet dynamics would be needed.

Chapter 7 Comparison of Arctic and Southern Ocean sea ice between the last nine interglacials and the future[3]

7.1 Introduction

Sea ice is an important component of the polar and global climate system, in part, due to its high albedo and low thermal conductivity, which are associated with the temperature-albedo feedback and the thermal insulation effect. It normally amplifies the climate variability at high latitudes, often known as polar amplification (e.g. Serreze and Barry, 2011). In addition, the melting and formation of sea ice can change the oceanic salinity structure. When sea ice forms, brine is rejected towards the ocean, supplying dense and well ventilated water to the global intermediate/deep water circulation, while it causes stratification between near-surface and deeper water during sea ice melts (Goosse et al., 2013). Sea ice also impacts the thermosteric sea level (e.g. sea level rise due to thermal expansion of the ocean) and the barystatic sea level (e.g. sea level rise due to fresh water input into the ocean) (Hobbs et al., 2016). Changes in sea ice extent not only affect the surface mass balance of the ice sheets (Krinner et al., 2007), but also shift the latitude of the mid-latitude storm tract belt (Kidston et al., 2011). Moreover, sea ice may influence the structure and function of high-latitude ecosystems and biogeochemical cycles (Delille et al., 2014), such as control the light and the distribution of phototrophic organisms, polar bear and penguin species (Ducklow et al., 2013). It has also been shown that the Arctic sea ice plays a critical role in abrupt climate changes in the past (Yin et al., 2021).

Rapid sea ice changes in the Arctic and Southern Ocean are observed not only during the recent decades (e.g. Serreze et al., 2016; Turner et

[3] This chapter is published in Wu Z.P., Yin Q.Z., Guo Z.T., Berger, A., 2022. Comparison of Arctic and Southern Ocean sea ice between the last nine interglacials and the future. Climate Dynamics, 59, 519-529.

al., 2013), but also during past interglacials (e.g. Cronin et al., 2013; Wolff et al., 2006). Based on paleo sea ice proxies, Bennike (2004) found that there was more sea ice in Greenland than at present during the early-mid Holocene and less sea ice during late Holocene. Stein et al. (2017) suggested lower sea ice cover in the Arctic Ocean during the last interglacial relative to today. Due to the lack of suitable, high-resolution proxies and limitation in dating technique, most sea ice reconstructions focus on the very recent interglacials, such as Holocene (e.g. Vare et al., 2009; de Vernal et al., 2020) and the last interglacial (e.g. Stein et al., 2017). A few long sea ice reconstructions covering several glacial-interglacial cycles have been established using paleoclimate records in the Arctic (Polyak et al., 2010; Cronin et al., 2010, 2013, 2017) and in the Southern Ocean (Wolff et al., 2006). These studies show that a major shift towards perennial sea ice in western Arctic Ocean occurred after MIS-11 (Cronin et al., 2017), and most of the Arctic Ocean might have been free of summer ice cover during the last interglacial which were mainly attributed to high insolation intensity (Polyak et al., 2010; Cronin et al., 2013). Spectral analyses indicate that the Arctic sea ice variations contain strong precession and obliquity cycles, and with precession signals dominating (Cronin et al., 2013; Lo et al., 2018). In the Southern Ocean, proxy record indicates that the maximum sea ice extent occurred during MIS-13 and the minimum sea ice extent during the last interglacial, and that the sea ice variations show very strong 100 ka cycles (Wolff et al., 2006). Climate modeling has also been used to understand the sea ice variations during past interglacials, for instance, during the Holocene (Goosse et al., 2013; Otto-Bliesner et al., 2020), the last interglacial (Guarino et al., 2020; Otto-Bliesner et al., 2020, 2021; Kageyama et al., 2021), the MIS-13 (Wu et al., 2020) and the last nine interglacials (Yin and Berger, 2012). These studies reveal that the Arctic and Southern Ocean sea ice variations show different characteristics under different interglacial conditions, and the dominating forcing mechanisms might be different.

Past interglacials, as the most recent warm periods in the Earth's history, play an important role in paleoclimate researches because they provide a basis for better understanding our present-day warm climate and its future evolution (Tzedakis et al., 2009; Past Interglacials Working Group of PAGES, 2016). They are useful to better understand climate internal processes and related feedbacks during warm intervals, and to discuss the effect of different external drivers, such as insolation and atmospheric CO_2 concentration. In addition, past interglacials might provide analogues of the future climate under natural warm climate variability, and help to improve our estimate of the sensitivity of the climate system to different forcings. When the sea ice variations are concerned, questions can be raised on (1) what are the differences between interglacials and between Arctic and Southern Ocean sea ice variations during these warm periods, (2) what are the controlling forcing and mechanisms, and (3) how are the past interglacials different from the present and the future?

A preliminary investigation of the individual and combined effect of insolation and CO_2 on the climate of the last nine interglacials has been performed by Yin and Berger (2012) using model simulations and factor separation analysis. Based on the simulations performed in their study, here we make an in-depth analysis of the internal processes that control the interglacial sea ice variability, and focus on the inter-comparison between individual interglacials as well as their differences from the present and future. The study of this Chapter is based on the nine snapshot experiments (f11) of the last nine interglacials performed in Yin and Berger (2012) and three new experiments of the future and future climate: PI, PD and Double_CO_2 (see Chapter 2).

7.2 Sea ice difference between interglacials and the impact of insolation and CO_2

Figure 7.1a shows the simulated annual and seasonal Arctic sea ice area over the last nine interglacials in response to the combined effect of insolation and CO_2. MIS-15, MIS-9 and MIS-5 have the smallest annual mean sea ice area, and MIS-13 has the largest one. The simulated winter Arctic sea ice area shows very small variation between the interglacials, and the variation in the annual mean is mainly explained by the variation in summer, which is similar to the recent observation (Titchner and Rayner, 2014). Previous study showed that the variation of the Arctic sea ice in summer is dominated by local summer insolation (Yin and Berger, 2012). Although the ECS of LOVECLIM is relatively small compared to many models, the sensitivity of the temperature response in the Arctic region in LOVECLIM is at the middle level of the multi-model range. Moreover, proxy records show that the Arctic sea ice varied mainly at precessional frequency (e.g. Cronin et al., 2013; Lo et al., 2018), which indicates the dominant effect of insolation. Therefore, the importance of insolation in the Arctic region compared to CO_2 should be a robust result, not due to the relatively small ECS of LOVECLIM. MIS-15, MIS-9 and MIS-5 have the highest summer insolation (Figure 7.2a), explaining their smallest sea ice area. On the contrary, MIS-13, MIS-7 and MIS-11 have the lowest summer insolation (Figure 7.2a), explaining their largest sea ice area, while the large annual mean Arctic sea ice area at MIS-17 could probably be related to its lowest CO_2 concentration and moderate local summer insolation (Figure 7.2b).

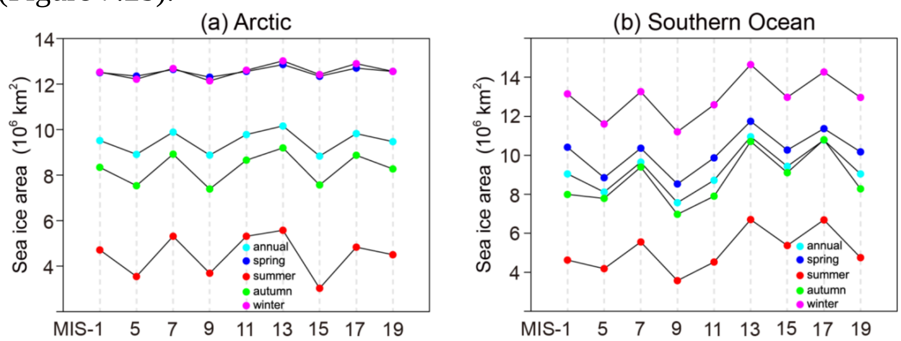

Figure 7.1 Simulated annual and seasonal sea ice area during the nine interglacials in the (a) Arctic and (b) Southern Ocean. The seasons refer to the local seasons.

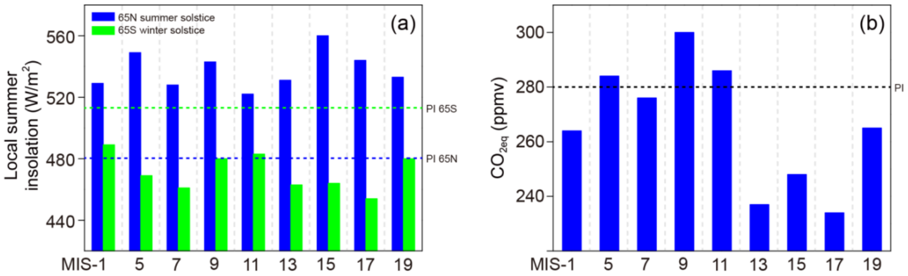

Figure 7.2 Local summer insolation at 65°N and 65°S (Berger, 1978) (a) and the CO_{2eq} concentrations (b) during the nine interglacials and the PI. The dash horizontal lines indicate the PI level.

In the Southern Ocean, MIS-5, MIS-9 and MIS-11 have the smallest annual mean sea ice area, and MIS-13 and MIS-17 have the largest one (Figure 7.1b). Both the simulated local summer and local winter sea ice area in the Southern Ocean show significant variations between the interglacials with the amplitude being larger in summer (Figure 7.1b). Previous study showed that, in the Southern Ocean, CO_2 plays a dominant role in the sea ice variation in local winter, whereas both insolation and CO_2 play an important role on the sea ice in local summer (Yin and Berger, 2012). This leads to a dominant role of CO_2 in the variation of the annual mean sea ice area in the Southern Ocean, but with a non-negligible role of insolation. The smallest annual mean Southern Ocean sea ice at MIS-5, MIS-9 and MIS-11 are explained by the highest CO_2 concentration (Figure 7.2b) during these interglacials and a moderate local summer insolation (Figure 7.2a). The largest annual mean Southern Ocean sea ice area at MIS-13 and MIS-17 are explained by the lowest CO_2 concentration (Figure 7.2b) combined with low local summer insolation (Figure 7.2a). Our results show that both the annual mean Arctic and Southern Ocean sea ice area at MIS-19 is the closest to that at MIS-1 and is followed by MIS-11 (Figure 7.1), which is in line with the proposition that MIS-19 is a better analogue for MIS-1 than MIS-11 (Tzekadis et al., 2012; Yin and Berger, 2012, 2015).

Our results show that the Mid-Brunhes Event (MBE) (Yin and Berger, 2010) appears to be significant in the Southern Ocean sea ice, which is characterized by less sea ice in MIS-1, -5, -7, -9 and -11 than in MIS-13, -15, -17 and -19, but it is not obvious in the Arctic sea ice (Figure 7.1). This can be explained by the fact that the Southern Ocean sea ice is mainly dominated by CO_2 which itself shows a clear MBE, while the Arctic sea ice is mainly dominated by local summer insolation which does not have clear MBE (Yin and Berger, 2012).

The sea ice reconstruction in the Southern Ocean of Wolff et al. (2006) is one of the very few long sea ice reconstructions covering many glacial-interglacial cycles. Their results have a great consistency with our simulated results. Both the reconstructions and simulations show that MIS-13 and MIS-17 have the largest annual mean Southern Ocean sea ice and MIS-5 and MIS-9 have the smallest one (Figure 7.3). A notable difference is in MIS-15 which has the second least sea ice in the reconstructions while it has a relatively large sea ice area in the simulations. This difference could originate from the uncertainty in both our model and the reconstructions. More model simulations and reconstructions would be helpful to understand better this model-data discrepancy.

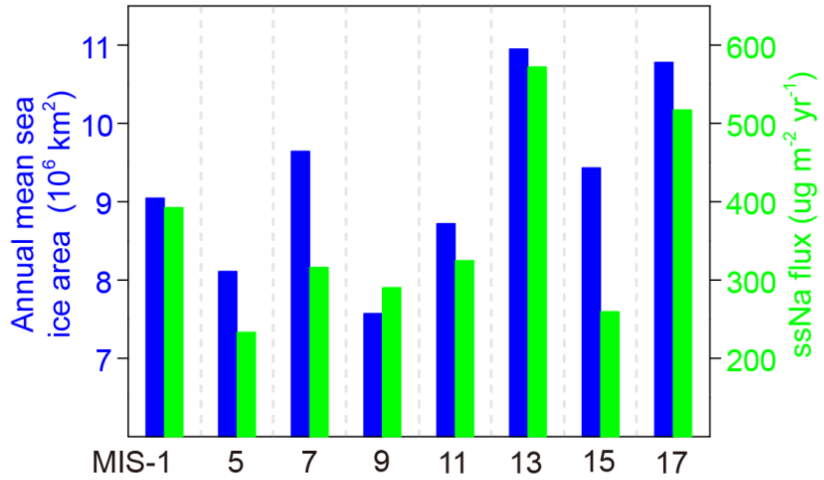

Figure 7.3 Simulated annual mean Southern Ocean sea ice area (blue bars) in comparison to the EPICA Dome C sea salt flux (Wolff et al., 2006) (green bars). The minimum values of the EPICA Dome C sea salt flux for each interglacial are used.

The sea ice variation during the interglacials is strongly coupled with the sea surface temperature and the surface energy budget over the polar oceans (Figure 7.4). High surface energy budget leads to warmer sea surface temperature and less sea ice, and vice versa. In both the Arctic and Southern Ocean, the highest surface energy budget at MIS-9 and MIS-5 are explained by their relatively high local summer insolation (Figure 7.2a) and high CO_2 concentration (Figure 7.2b), which lead to low sea ice area; while the lowest surface energy budget at MIS-13 can be explained by low local summer insolation (Figure 7.2a) and low CO_2 concentration (Figure 7.2b), which leads to high sea ice area. The Arctic and Southern Ocean sea ice conditions are also influenced by the variation in the poleward oceanic meridional heat transport across 60°N and 60°S respectively, although the variations of northward oceanic meridional heat transport across 60°N are relatively small between interglacials (Goosse and Renssen, 2001; Yin and Berger, 2012). The largest southward global oceanic meridional heat transport across 60°S at MIS-5 and MIS-9 could also have contributed to the lowest Southern Ocean sea ice area during these two interglacials (Figure 7.1b).

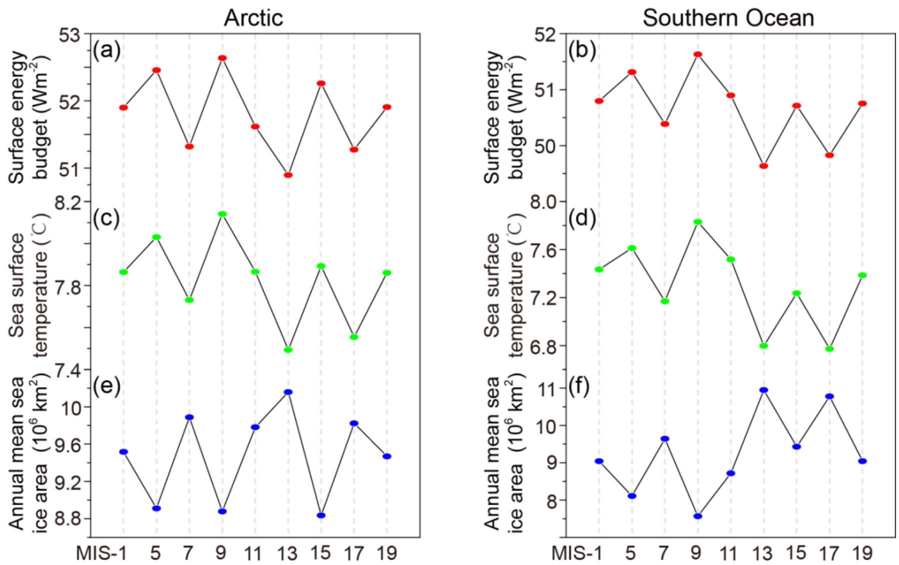

Figure 7.4 Annual mean sea ice area, sea surface temperature and surface energy budget over the Arctic (40°N-90°N) and Southern Ocean (40°S-90°S).

7.3 Comparison of sea ice between the past interglacials and the present

Figure 7.5a and Figure 7.5b show the annual and seasonal sea ice area anomaly of the last nine interglacials as compared to the PI. In the Arctic, the interglacials all have less annual mean sea ice than the PI, with the maximum sea ice decrease of about 22% at MIS-15 and the minimum decrease of about 11% at MIS-13 (Figure 7.5a). For each interglacial, the four seasons all have less sea ice, and the sea ice decrease in summer is much larger than in other seasons. As has been discussed in Section 7.2, most variation of the summer Arctic sea ice can be explained by insolation. Moreover, the CO_2eq difference between the interglacials and the PI is relatively small, ranging from 4 to 46 ppmv (Figure 7.2b). The much less summer sea ice during the interglacials is therefore mainly due to the much higher summer insolation during the past interglacials as compared to the PI (Figure 7.2a). Figure 7.6 shows the detailed spatial comparison of the summer Arctic sea ice concentration between MIS-15, MIS-13 and the PI. As compared to the PI, the sea ice in the Barents Sea, North Greenland Sea, Labrador Sea and Beaufort Sea totally melts, and the sea ice concentration in the central Arctic largely decreases in MIS-15. The sea ice extent at MIS-13 is larger than that at MIS-15, but it still retreats in the Barents Sea and North Greenland Sea when compared to the PI. In the Paleoclimate Modelling Intercomparison Project (PMIP) simulations of the middle Holocene and the last interglacial, most models have also simulated less Arctic sea ice as compared to the PI due to the intensified summer insolation in the Arctic, and the sea ice anomaly simulated by LOVECLIM is at the middle value among the PMIP simulations (Kageyama et al., 2020; Otto-Bliesner et al., 2021).

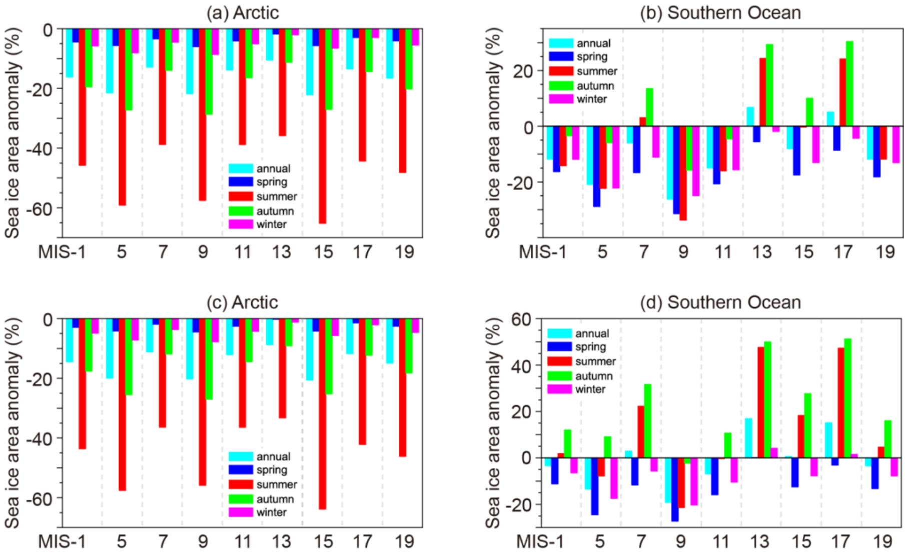

Figure 7.5 Annual and local seasonal sea ice area anomaly during the last nine interglacials in the Arctic and Southern Ocean, relative to the PI experiment (a, b) and PD experiment (c, d).

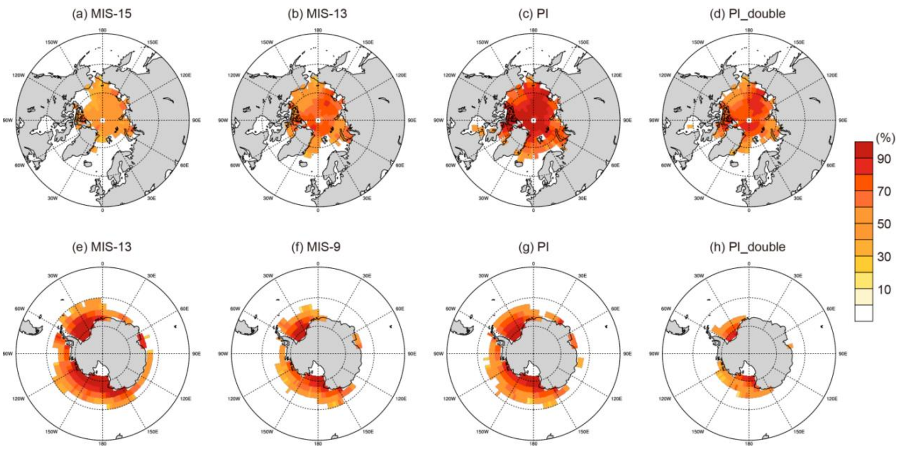

Figure 7.6 Simulated summer Arctic sea ice concentration at (a) MIS-15, (b) MIS-13, (c) PI, (d) $2xCO_2$ and summer Southern Ocean sea ice concentration at (e) MIS-13, (f) MIS-9, (g) PI, (h) $2xCO_2$.

In the Southern Ocean, most interglacials have less sea ice than the PI (Figure 7.5b), except MIS-13 and MIS-17 which have about 25%-30% more sea ice during local summer and autumn, leading to more annual sea ice. As has been discussed in Section 7.2, both insolation and CO_2 play an important role in the summer Southern Ocean sea ice. The increased summer sea ice at MIS-13 and MIS-17 is due to their relatively low CO_2 concentration (Figure 7.2b) and low local summer insolation (Figure 7.2a). On the contrary, due to high CO_2 concentration (Figure 7.2b) and high local summer insolation (Figure 7.2a), the sea ice area at MIS-9 is about 25%-30% less than the PI (Figure 7.5b). As compared to the PI, the summer Southern Ocean sea ice at MIS-13 noticeably advanced, especially in the west Southern Ocean, which extended to 60°S (Figure 7.6). However, the summer Southern Ocean sea ice significantly retreated at MIS-9, and this retreat is also obvious in the west Southern Ocean (Figure 7.6).

As compared to the PI which has a similar CO_2 concentration to many interglacials, the CO_2 concentration of the PD is much larger with an increase of 66 ppmv above the PI level. However, in terms of the comparison with the past interglacials, this larger amount of CO_2 does not make significant difference between the PD ($3.71*10^6$ km^2) and the PI ($3.79*10^6$ km^2) in the Arctic sea ice. This is because the variation of the Arctic sea ice area is mainly controlled by summer insolation as explained in Section 7.2, which is assumed to be the same between the PI and the PD. In the Southern Ocean, the sea ice area in the PD ($3.12*10^6$ km^2) is about 10% less than in the PI ($3.42*10^6$ km^2) due to the increase of CO_2. As a consequence, the sea ice area at MIS-17 and MIS-13, which is already well above the PI level, is even larger when compared to the PD, with an increase of about 50% in local summer and autumn (Figure 7.6d). The positive sea ice anomaly at MIS-7 and MIS-15 is also more pronounced when compared to the PD (Figure 7.5c). Compared to the PD, the warm interglacials MIS-5 and MIS-9 still have much less sea ice in the Southern Ocean, with a reduction of about 15% and 20% in the annual mean (Figure 7.5d).

7.4 Comparison of sea ice between interglacials and the future

As compared to the PI, the annual mean Arctic sea ice decreases by about $1.8*10^6$ km^2 in the $2xCO_2$ experiment, a value which is at the low level among the PMIP simulations, and the south boundary of the sea ice in the North Atlantic largely shifts northward and the sea ice concentration in the central Arctic largely decreases (Figure 7.6). In the Southern Ocean, the annual mean sea ice in the $2xCO_2$ experiment decreases by about $5.6*10^6$ km^2 as compared to the PI which is at the high level among the PMIP simulations. In addition, the sea ice is mainly constrained around the Weddell sea and Ross sea in the $2xCO_2$ experiment due to the significant decrease (Figure 7.6).

It is shown in Section 7.3 that as compared to the present-day, all the nine interglacials have much less sea ice in the Arctic and many also have less sea ice in the Southern Ocean. Figure 7.7a shows that, as compared to the $2xCO_2$ experiment, in the Arctic, all the interglacials still have significantly less sea ice in summer due to much higher summer insolation, with the maximum decrease at MIS-15 and minimum decrease at MIS-13. At MIS-15, the sea ice south boundary in the North Atlantic retreats to the north of 75°N, and sea ice in the Beaufort Sea totally melts when compared to the $2xCO_2$ (Figure 7.6). The sea ice extent at MIS-13 is generally similar to the $2xCO_2$, but the sea ice concentration in the central Arctic is significantly less (Figure 7.6). On the other hand, there is more sea ice in other seasons for most interglacials due to their much lower CO_2 concentration. In the annual mean, the sea ice area in MIS-5, MIS-9 and MIS-15, which have the highest summer insolation in the northern high latitudes, is still smaller than the future by about 7%, whereas MIS-7, MIS-11, MIS-13 and MIS-17 have more annual sea ice than the future. The annual sea ice area of MIS-1 and MIS-19 is very close to that of the future, which means that in terms of annual sea ice area in the Arctic, the effect of a CO_2 increase of about 295 ppmv is balanced by the effect of an increase of summer insolation at 65°N by 50 W/m^2.

In the Southern Ocean, the interglacials all have much more annual mean sea ice than the future (Figure 7.7b), with the MIS-13 maximum annual mean sea ice being about 134% larger and the MIS-9 minimum about 62%. These are consistent with SST changes in the southern high latitudes (40°S-90°S), this SST of the 2xCO_2 experiment being 2.23°C higher than MIS-13 and 1.20°C higher than MIS-9. In addition, the meridional ocean heat transport across 60°S in the 2xCO_2 experiment is increased by about 28% and 11% as compared to that in MIS-13 and in MIS-9 respectively. The substantial increase of the meridional ocean heat transport implies that the impact of the tropical oceans on Antarctica climate would be stronger in the future than the past interglacials due to increased CO_2 concentration. For each interglacial, the four seasons all have more sea ice, and the sea ice increase in summer is the largest (Figure 7.7b). This is due to the dominant role of CO_2 on the Southern Ocean sea ice, and the much lower CO_2 concentration during the interglacials than the future.

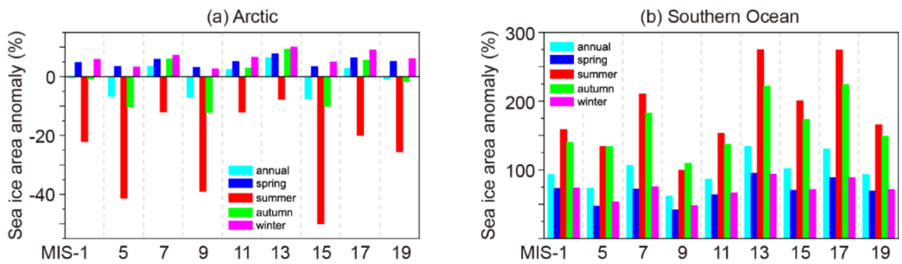

Figure 7.7 Annual and local seasonal sea ice area anomaly during the last nine interglacials in the (a) Arctic and (b) Southern Ocean, relative to 2xCO_2 experiment.

7.5 Conclusions

In this study, the sea ice of the last nine interglacials, as well as their differences from the present and future are investigated through simulations with the LOVECLIM model. Our results show that the sea ice variations between the interglacials are different between the Arctic and Southern Ocean. In the Arctic, MIS-15, MIS-9 and MIS-5 have the smallest annual mean sea ice area, and MIS-13 has the largest one. The annual mean Arctic sea ice area variation is dominated by the variation in summer, which is mainly controlled by local summer insolation. Thus, the annual mean Arctic sea ice variation is mainly explained by summer insolation. However, in the Southern Ocean, the annual mean sea ice variation is mainly explained by the CO_2 concentration, but the effect of insolation can't be ignored. MIS-13 and MIS-17 have the largest annual mean Southern Ocean sea ice area, which is mainly explained by their lowest CO_2 concentration combined with low local summer insolation.

It has been shown in Section 2.2 that LOVECLIM1.2 belongs to high-sensitivity models in terms of temperature and sea ice response to $2xCO_2$ in the SH while it belongs to low-sensitivity models in the NH. It could be argued that this could be responsible for our finding that the Arctic sea ice variation during the past intergalcials is dominated by local summer insolation whereas the Southern Ocean sea ice variation is dominated by CO_2. However, we would like to note and stress that our simulated variations of Arctic and Southern Ocean sea ice are in good consistency with the sea ice reconstructions based on proxy records. For example, the sea ice record in the central Okhotsk Sea show that the Arctic sea ice is dominated by precession over the last 130 ka (Lo et al., 2018), whereas the sea ice reconstruction from Southern Ocean shows strong glacial-interglacial cycles like in the CO_2 record (Wolff et al., 2006). These are in line with our simulated results, showing the robustness of our finding on the interglacial climates.

As compared to the present (both the PI and PD experiments), the interglacials all have less annual mean Arctic sea ice, which is explained by the much higher summer insolation in the Arctic during the interglacials. As compared to the future, in the Arctic, all the interglacials still have significantly less sea ice in summer due to much higher summer insolation, with the maximum sea ice decrease of about 50% at MIS-15. But there is more sea ice in other seasons for most interglacials due to their much lower CO_2 concentration. In the Southern Ocean, the interglacials all have much more sea ice than the future due to their much lower CO_2 concentration, with the maximum annual mean sea ice increase of about 134% at MIS-13.

In terms of the potential analogue of our present interglacial, our results show that MIS-19 is the closest to MIS-1 in terms of the Arctic and Southern Ocean sea ice. However, when compared with the present condition (the PI or PD), the last nine interglacials all show significant differences in the Arctic and Southern Ocean sea ice and in particular show greater seasonal differences. These differences are mainly due to the different seasonal insolation distribution between the intergalcials and the present. Therefore, in the search of potential analogue of the present or future climate, the seasonal climate variations deserve to be considered. Our results show that, compared to the $2xCO_2$ experiment, the last nine interglacials all have much reduced sea ice in the Arctic due to much higher summer insolation. Thus, in terms of the changes of Arctic sea ice and related processes and feedbacks, the past interglacials could possibly be considered as analogue for the future, although the major cause is different, i.e. insolation for the interglacials and CO_2 for the future. However, it is hard to consider the interglacials as analogue for the future in terms of the Southern Ocean sea ice, because all the interglacials have much more sea ice than the $2xCO_2$ experiment in the Southern Ocean due to their much lower CO_2 concentration.

Chapter 8 Conclusions and perspectives

8.1 Conclusions

Understanding the response of the climate system to astronomical parameters, GHG and ice sheets, as well as the half-precession cycles during the past warm periods is an important topic in paleoclimate study. It is not only fundamental research, but could also help better understand our present warm climate and its future evolution. This thesis aims at investigating the response of different climatic variables at different regions to astronomical parameters, GHG and NH ice sheets, as well as the half-precession signals during the nine interglacials of the last 800 ka based on both snapshot and transient simulations using the model LOVECLIM. With the two versions of LOVECLIM, LOVECLIM1.2 and LOVECLIM1.3, 28 long transient simulations without acceleration and more than 40 snapshot simulations are performed.

The individual effect of astronomical parameters, CO_2 and NH ice sheets is first investigated. In terms of the astronomical parameters, the annual mean Arctic sea ice is dominated by precession, while the annual mean Southern Ocean sea ice is dominated by obliquity. The annual mean Arctic sea ice is dominated by its variation in summer, which is mainly controlled by the local summer insolation that in turn is mainly a function of precession. It is also influenced by the northward oceanic heat transports which is also dominated by precession. While in the Southern Ocean, the annual mean sea ice variations are more equally influenced by the variations in the four seasons with the amplitude being slightly larger in local summer, and the summer Southern Ocean sea ice variation is also dominated by obliquity. These lead to that obliquity is more important in the Southern Ocean sea ice. The effect of obliquity on the annual mean Southern Ocean sea ice is mainly through its influence on the local insolation and also on the SH westerly winds. For the SST at low latitudes of both hemispheres, precession plays a dominant role. For the SST in the mid and high latitudes, precession is more important in the NH, while obliquity is more important in the SH. Our results also show that when eccentricity is small, which leads to small variation of precession, obliquity could play a more important role than precession. If the effect of CO_2 is considered, our results show that it is more important in the SST at mid-high latitudes and sea ice in the SH than in the NH, and the amplitude of variation of SST at low latitudes is smaller than at mid-high latitudes.

Our sensitivity experiments show that the closure of the Hudson Bay could lead to a strengthening of the AMOC, which in turn leads to a warming in the NH with the notable warming in the Labrador Sea and northeast North Atlantic, a cooling in the SH and a northward shift of the ITCZ. The sea ice declines obviously in the Labrador Sea due to the largest warming there, while the sea ice increases in the southeast Greenland due to the sea ice export, and it leads to a cooling in the east Greenland due to the sea ice-temperature feedback. On the other hand, there is an obvious cooling over the Hudson Bay, which can be explained by the land ice albedo and topography effect when the Hudson Bay is closed. In addition, there are more precipitation in the Labrador Sea and northeast North Atlantic and less precipitation in the Hudson Bay and east Greenland, which is induced by the vertical motion anomaly caused by the different warming and cooling in these regions. However, the effect of the Hudson Bay closure depends on background climate conditions, and it could weaken or slightly reinforce the effect of the ice sheets for different astronomical configurations. As compared to the effect of NH ice sheets, the effect of Hudson Bay closure could be significant especially in the regions of Labrador Sea, Hudson Bay and North Atlantic. Our results suggest that it is better to consider the changes of the Hudson Bay in the simulations with large North American ice sheet. However, due to the coarse resolution of LOVECLIM, the effect of Hudson Bay needs to be tested and confirmed with high-resolution ocean models.

If the individual influence of the NH ice sheets is considered, both the Southern Ocean sea ice and the SST at SH mid-high latitudes have a high correlation with the NH ice volume. A high NH ice volume leads to a cooling at SH mid-high latitudes and more Southern Ocean sea ice. While the relationships between the NH ice sheets and the Arctic sea ice and the NH mid-high latitude SST appear more complex and non-linear. The effect of the NH ice sheets depends on their size, location and the NH summer insolation. Insolation plays a dominant role on the Arctic sea ice and the SST at NH mid-high latitudes, while NH ice sheets play a dominant role on the Southern Ocean sea ice and the SST at SH mid-high latitudes. The SST at low latitudes of both hemispheres is dominated by CO_2 and NH ice sheets. These model results are in line with proxy records which show strong precession cycles in the Arctic sea ice variations but strong 100-ka glacial-interglacial cycles in the Southern Ocean sea ice. It is worth noting that in our transient simulations with varied NH ice sheets, the sea level change is not considered. Some model results show that changes of sea level could have a great effect on global and regional climate (Zhang et al., 2023). A more complete study of the effect of ice sheets should also consider sea level changes.

Both proxy records and model simulations are used to systematically investigate the half-precession cycles. A compilation of the half-precession signals during the Quaternary has been made based on published records containing clear half-precession cycles. The results show that the half-precession cycles are mainly concentrated in the tropics and North Atlantic. The reanalysis of seven long, high-resolution proxy records shows that the half-precession signals vary with time and between different records. The LOVECLIM model results show that the half-precession signals could result from both external forcing and internal feedbacks. For example, in response to maximum equatorial insolation, the half-precession signals could be recorded in the different climatic variables near the Equator, such as precipitation, SAT and SST. Our model results also show that the half-precession signals at low latitudes could be transported to mid and high latitudes via atmospheric and oceanic circulations, confirming the hypothesis made from proxy records. In addition, the half-precession signals could be recorded in the grass fraction in the

Asian and African monsoon regions due to vegetation feedbacks. The half-precession signals in these climatic variables are influenced by different forcing factors. High eccentricity (and therefore large variation of precession) and small variation of obliquity would amplify the half-precession signals, and vice versa. GHG and ice sheets tend to weaken the half-precession signals. The half-precession cycles have been recorded in many proxy records, but most climate models failed to capture the half-precession cycles. In our simulated results, we have found the half-precession cycles in major climate variables in different latitudes. The reason that the half-precession cycles could not be reproduced in many other models is probably because 100 times acceleration is often used in the GCM simulations (Lu et al., 2019).

Finally, the sea ice of the past interglacials is compared with the sea ice of the present-day and the future. Our results show that insolation is more important in the Arctic sea ice, while CO_2 is more important in the Southern Ocean sea ice. Due to the effect of high summer insolation during the last nine interglacials, they all have much less annual and seasonal Arctic sea ice as compared to the present-day, and they also have much less summer Arctic sea ice as compared to the future. For the Southern Ocean, the simulated future sea ice is much reduced as compared to the past interglacials due to much higher CO_2 concentration, which questions the possibility of using past interglacials as analogue for the future at least as far as the Southern Ocean is concerned.

8.2 Perspectives

This thesis investigates the climate response to astronomical parameters, CO_2 and NH ice sheets, as well as the half-precession cycles during selected glacial-interglacial periods over the past 800 ka, including the forcing mechanisms, internal climate processes and feedbacks. However, some limitations can still be found in the current study and could be improved in the future.

First, it has been shown that LOVECLIM has a weak representation in the tropical regions. To have a better understanding of the tropical climate and the low-high latitude interactions, more complex GCMs could be used to perform sensitivity experiments and to test the results obtained in this thesis.

Second, although part of the transitions of the glacial termination and inception before and after each interglacial are included in the simulation periods, this thesis focuses on the interglacials over the past 800 ka. To have a larger view especially on the effect of GHG and ice sheets, longer simulations covering full glacial-interglacial cycles would be helpful.

Third, this thesis focuses on the response of sea ice and SST on different latitudinal bands. Paleoclimate records show that the climate response to different forcings is very diverse at regional scale. Therefore, the spatial diversity of more climate variables will be investigated in future studies.

Fourth, the NH ice sheets used in this study are those simulated by Ganopolski and Calov (2011). In the future, more scenarios of ice sheets including the SH ice sheets could also be considered to test the robustness of the results obtained in this thesis. Sensitivity experiments could also be performed to investigate the individual effect of the size and location of the ice sheets under different background climate conditions (e.g. high and low summer insolation and CO_2 concentration).

Fifth, the land-sea mask (expect over the Hudson Bay) and sea level are fixed in our simulations. Their effects could be considered in future studies. In addition, transient simulations including ice sheet dynamics would be needed to have a better understanding of the climate response to astronomical forcing especially the half-precession cycles.

Finally, more high-resolution proxy records with clearly defined climate signals and good chronology would be needed. This would help to reduce the uncertainties in the paleoclimate interpretation of the proxy records and their chronology, and to improve proxy-model comparison.

Supplement to Chapter 3

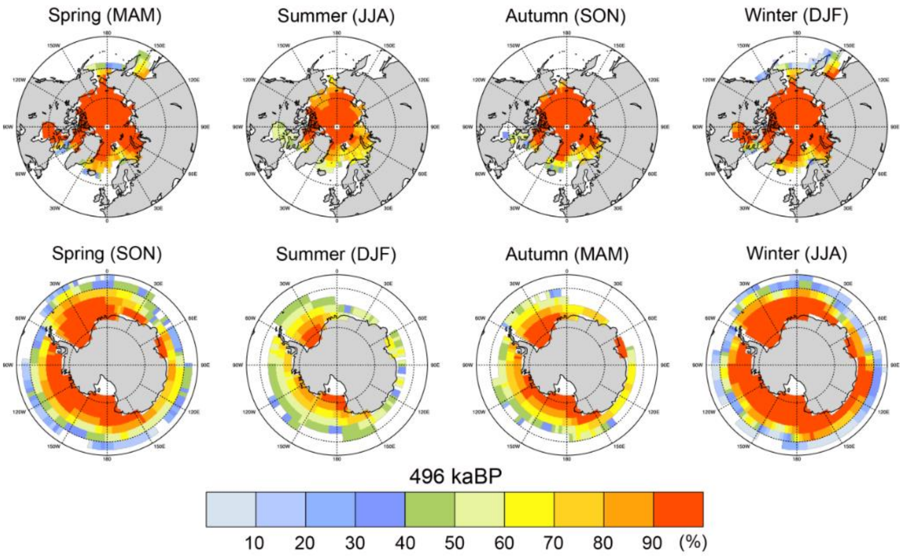

Figure S3.1 The seasonal (local seasons are used) geographical distribution of the Arctic and Southern Ocean sea ice at a precession maximum (496 ka BP).

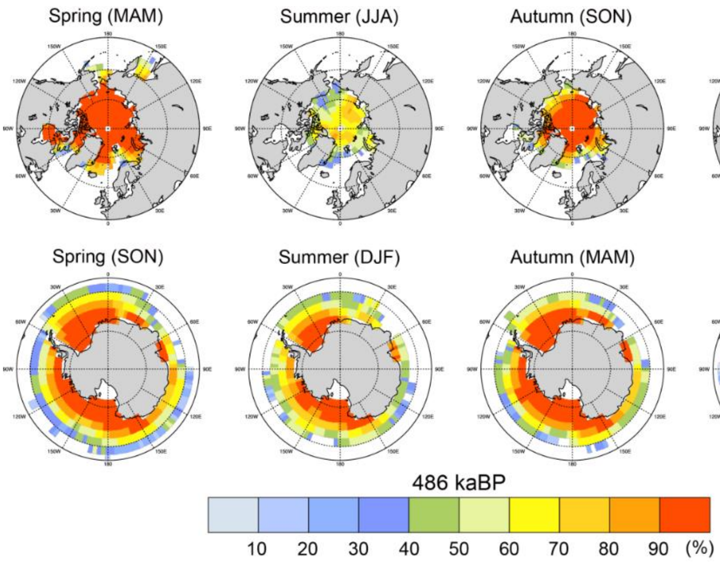

Figure S3.2 The seasonal (local seasons are used) geographical distribution of the Arctic and Southern Ocean sea ice at a precession minimum (486 ka BP).

Table S3.1 Regression coefficients of a linear multiple regression between the insolation-induced climatic variables (the predictand) and E (eccentricity), O (obliquity) and P (precession) (the predictors). The calculation is based on the data of the simulation period between 511 and 460 ka BP. The variables are annual mean sea ice fraction and sea surface temperature. All the values have been standardized to have the regression coefficients representing comparable weights of the predictors on the predictand.

	sea ice fraction		sea surface temperature (SST)						
	Arctic	Southern Ocean	60°S-90°S	30°S-60°S	10°S-30°S	10°S-10°N	10°N-30°N	30°N-60°N	60°N-90°N
R^2	0.81	0.49	0.71	0.87	0.39	0.17	0.44	0.51	0.79
E	-0.04	-0.06	0.07	0.13	0.26	-0.12	0.08	0.08	0.04
O	-0.24	-0.62	0.83	0.87	0.41	-0.33	0.01	0.44	0.34
P	0.88	-0.28	-0.05	-0.33	-0.44	-0.17	-0.68	-0.57	-0.84

Table S3.2 Regression coefficients of a linear multiple regression between the insolation-induced climatic variables (the predictand) and E (eccentricity), O (obliquity) and P (precession) (the predictors). The calculation is based on the data of the simulation period between 460 and 417 ka BP. The variables are annual mean sea ice fraction and sea surface temperature. All the values have been standardized to have the regression coefficients representing comparable weights of the predictors on the predictand.

	sea ice fraction		sea surface temperature (SST)						
	Arctic	Southern Ocean	60°S-90°S	30°S-60°S	10°S-30°S	10°S-10°N	10°N-30°N	30°N-60°N	60°N-90°N
R^2	0.63	0.70	0.93	0.94	0.24	0.28	0.13	0.72	0.65
E	-0.10	-0.30	0.22	0.16	0.01	-0.71	-0.59	0.14	0.01
O	-0.61	-0.98	0.79	0.88	0.53	-0.14	0.65	0.73	0.72
P	0.33	-0.13	-0.05	-0.11	-0.14	0.24	-0.24	-0.32	-0.36

Table S3.3 Regression coefficients of a linear multiple regression between the surface energy budget (the predictand) and E (eccentricity), O (obliquity) and P (precession) (the predictors). The calculation is based on the data of the simulation period between 511 and 460 ka BP. The surface energy budget has been standardized to have the regression coefficients representing comparable weights of the predictors on the predictand.

	surface energy budget			
	40°N-90°N	40°S-90°S	60°N-90°N	60°S-90°S
R^2	0.90	0.72	0.86	0.66
E	0.07	0.19	0.07	0.11
O	0.43	0.74	0.42	0.78
P	-0.86	-0.39	-0.84	-0.21

Table S3.4 Regression coefficients of a linear multiple regression between the surface energy budget (the predictand) and E (eccentricity), O (obliquity) and P (precession) (the predictors). The calculation is based on the data of the simulation period between 460 and 417 ka BP. The surface energy budget has been standardized to have the regression coefficients representing comparable weights of the predictors on the predictand.

	surface energy budget			
	40°N-90°N	40°S-90°S	60°N-90°N	60°S-90°S
R^2	0.92	0.89	0.87	0.92
E	-0.02	0.11	-0.14	0.09
O	0.91	0.98	0.95	0.99
P	-0.36	-0.17	-0.32	-0.14

Supplement to Chapter 6

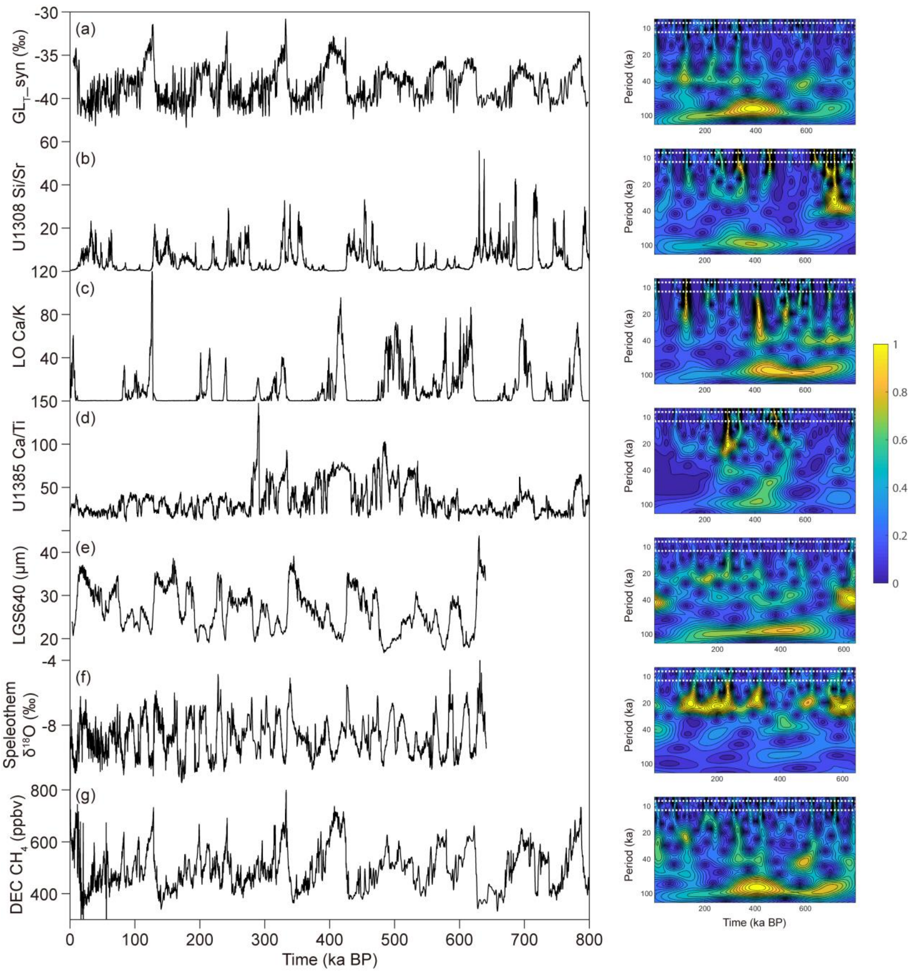

Figure S6.1 Variations of the seven high-resolution proxy records (left) and their wavelet transform results (right). (a) the Greenland synthetic $\delta^{18}O$ (Barker et al., 2011); (b) Si/Sr of IODP U1308 (Hodell et al., 2008); (c) Ca/K of Lake Ohrid sediment (Vogel et al., 2010); (d) Ca/Ti of IODP U1385 (Hodell et al., 2015); (e) loess grain-size stack (Sun et al., 2021b); (f) composited stalagmite $\delta^{18}O$ (Cheng et al., 2016); (g) DEC CH_4 (Loulergue et al., 2008).

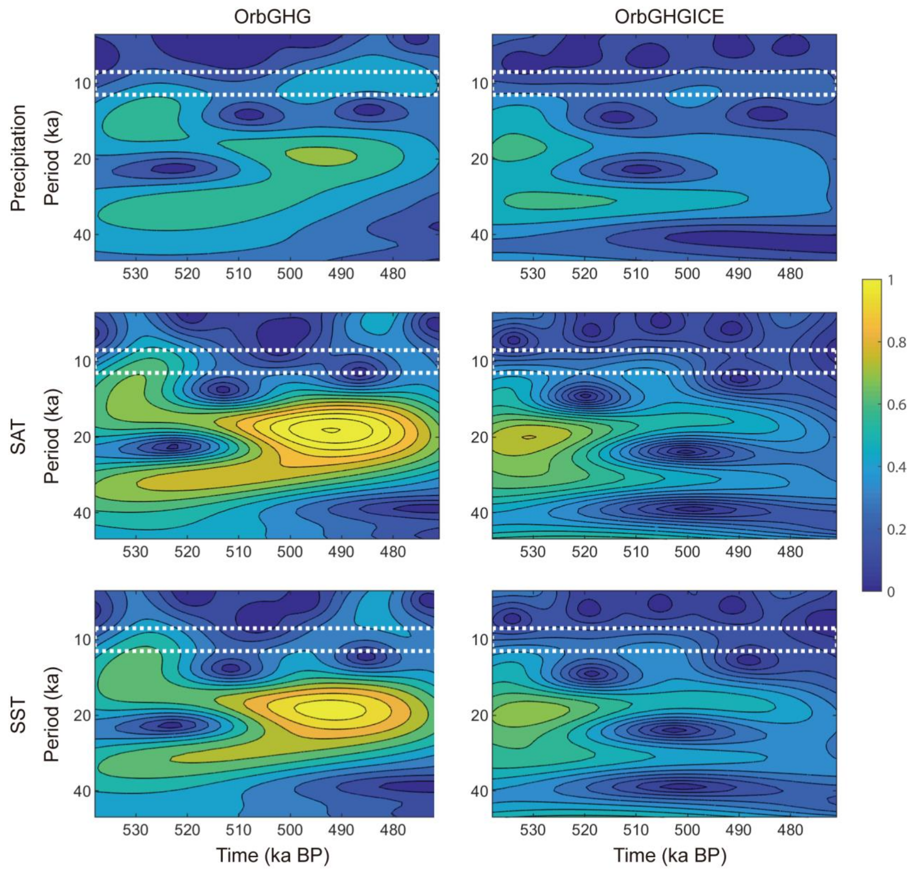

Figure S6.2 The continuous wavelet transform results of the precipitation, SAT and SST at the Equator (10°S-10°N) in the OrbGHG and OrbGHGICE experiments during MIS-13.

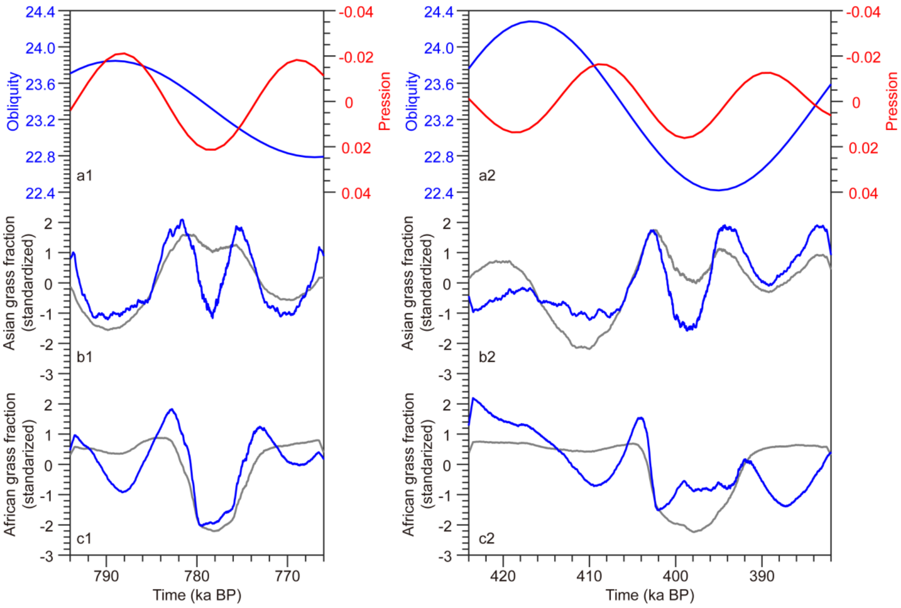

Figure S6.3 Variations of the annual mean grass fraction in the "Asian" and "African" monsoon regions in the Orb experiments during MIS-19 and MIS-11. (a1, a2) obliquity (blue line) and precession (red line) (Berger and Loutre, 1991), (b1, b2) the annual mean grass fraction variations in the "Asian" monsoon region, the grey lines are the origin data (1000-year running mean), and the blue lines are the result of the high-pass filter (<14 ka), (c1, c2) are the same as (b1, b2), but for the "African" monsoon region.

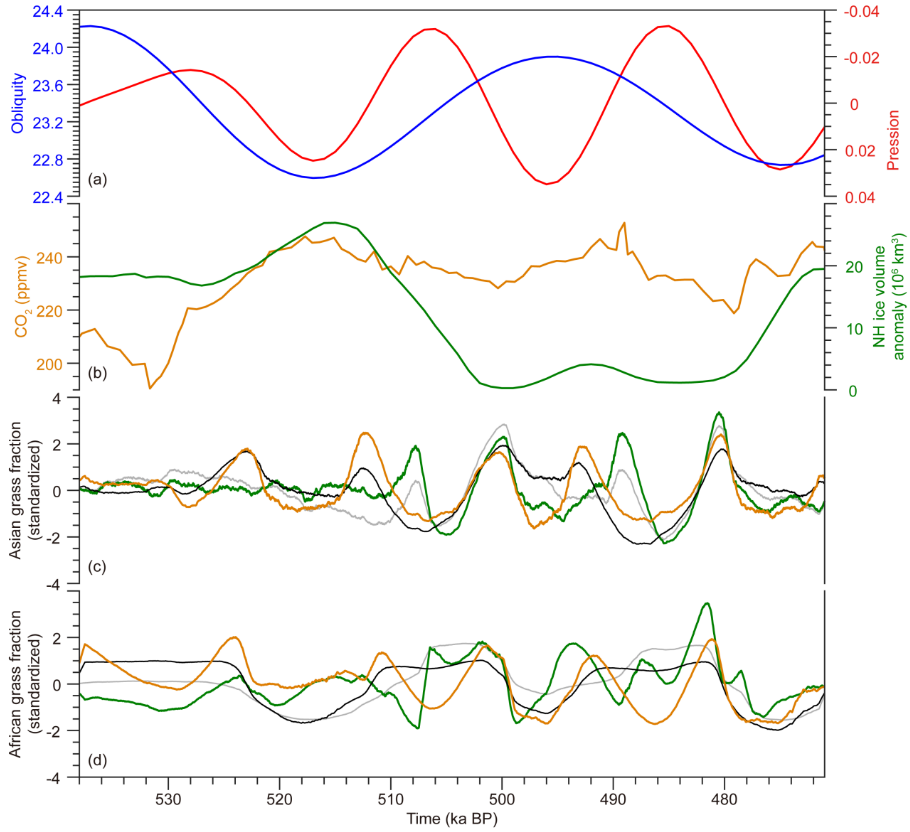

Figure S6.4 Variatins of the annual mean grass fraction in the "Asian" and "African" monsoon regions in the OrbGHG and OrbGHGICE experiments during MIS-13. (a) obliquity (blue line) and precession (red line) (Berger and Loutre, 1991), (b) the CO_2 concentration (yellow line, Lüthi et al., 2008) and NH ice volume anomaly as compared to the PI (dark green line, Ganopolski and Calov, 2011), (c) the annual mean grass fraction variations in the "Asian" monsoon region, the black line represents the origin data (1000-year running mean), and the dashed yellow line is the result of 9-11 ka filter in the OrbGHG experiment; the grey line represents the origin data (1000-year running mean), and the dashed dark green line is the result of 9-11 ka filter in the OrbGHGICE experiment. (d) is the same as (c), but for the "African" monsoon region.

References

Adler, R.F., Sapiano, M.R., Huffman, G.J., Wang, J.J., Gu, G., Bolvin, D., et al., 2018. The Global Precipitation Climatology Project (GPCP) monthly analysis (new version 2.3) and a review of 2017 global precipitation. Atmosphere 9(4), 9040138.

Amore, F.O., Flores, J.A., Voelker, A.H.L., Lebreiro, S.M., Palumbo, E., Sierro, F.J., 2012. A Middle Pleistocene Northeast Atlantic coccolithophore record: Paleoclimatology and paleoproductivity aspects. Marine Micropaleontology 90, 44-59.

Asami, R., Iryu, Y., Hanawa, K., Miwa, T., Holden, P., Shinjo, R., et al., 2013. MIS 7 interglacial sea-surface temperature and salinity reconstructions from a southwestern subtropical Pacific coral. Quaternary Research 80(3), 575-585.

Ashkenazy, Y., Gildor, H., 2008. Timing and significance of maximum and minimum equatorial insolation. Paleoceanography 23(1), PA1206.

Bard, E., Rickaby, R.E., 2009. Migration of the subtropical front as a modulator of glacial climate. Nature 460(7253), 380-384.

Barker, S., Knorr, G., Edwards, R.L., Parrenin, F., Putnam, A.E., Skinner, L.C., et al., 2011. 800,000 years of abrupt climate variability. Science 334(6054), 347-351.

Barker, S., Starr, A., van der Lubbe, J., Doughty, A., Knorr, G., Conn, S., et al., 2022. Persistent influence of precession on northern ice sheet variability since the early Pleistocene. Science 376(6596), 961-967.

Barthélemy, A., Goosse, H., Mathiot, P., Fichefet, T., 2012. Inclusion of a katabatic wind correction in a coarse-resolution global coupled climate model. Ocean Modelling 48, 45-54.

Beaufort, L.D., de Garidel-Thoron, T., Linsley, B., Oppo, D., Buchet, N., 2003. Biomass burning and oceanic primary production estimates in the Sulu Sea area over the last 380 kyr and the East Asian monsoon dynamics. Marine Geology 201(1-3), 53-65.

Bell, B., Hersbach, H., Simmons, A., Berrisford, P., Dahlgren, P., Horányi, A., et al., 2021. The ERA5 global reanalysis: Preliminary extension to 1950. Quarterly Journal of the Royal Meteorological Society 147(741), 4186-4227.

Bennike, O., 2004. Holocene sea-ice variations in Greenland: onshore evidence. Holocene 14(4), 607-613.

Berger, A., 1976. Obliquity and precession for the last 5000000 years. Astronomy and Astrophysics 51, 127-135.

Berger, A., 1978. Long-term variations of daily insolation and Quaternary climatic changes. Journal of Atmospheric Sciences 35(12), 2362-2367.

Berger, A., 1988. Milankovitch theory and climate. Reviews of geophysics 26(4), 624-657.

Berger, A., Loutre, M.F., 1991. Insolation values for the climate of the last 10 million years. Quaternary Science Reviews 10(4), 297-317.

Berger, A., Loutre, M.F., 1997. Intertropical latitudes and precessional and half-precessional cycles. Science 278(5342), 1476-1478.

Berger, A., Loutre, M.F., 2002. An exceptionally long interglacial ahead?. Science 297(5585), 1287-1288.

Berger, A., Loutre, M. F., 2003. Climate 400,000 years ago, a key to the future?. Geophysical Monograph-American Geophysical Union 137, 17-26.

Berger, A., Loutre, M.F., Mélice, J.L., 2006. Equatorial insolation: from precession harmonics to eccentricity frequencies. Climate of the Past 2(2), 131-136.

Berger, A., Loutre, M.F., Yin, Q., 2010. Total irradiation during any time interval of the year using elliptic integrals. Quaternary Science Reviews 29(17-18), 1968-1982.

Berger, A., Pestiaux, P., 1984. Accuracy and stability of the Quaternary terrestrial insolation, In Milankovitch and climate: understanding the response to astronomical forcing (p.83).

Berger, A., Yin, Q.Z., 2012. Modeling the interglacials of the last one million years. In: "Climate change at the eve of the second decade of the century. Inferences from paleoclimates and regional aspects". Milankovitch 130th Anniversary Symposium, A. Berger, F. Mesinger, D. Sijacki (eds), Springer, pp 57-64.

Billups, K., Hudson, C., Kunz, H., Rew, I., 2016. Exploring Globorotalia truncatulinoides coiling ratios as a proxy for subtropical gyre dynamics in the northwestern Atlantic Ocean during late Pleistocene Ice Ages. Paleoceanography 31(5), 553-563.

Billups, K., Rabideaux, N., Stoffel, J., 2011. Suborbital-scale surface and deep water records in the subtropical North Atlantic: implications on thermohaline overturn. Quaternary Science Reviews 30(21-22), 2976-2987.

Billups, K., Scheinwald, A., 2014. Origin of millennial-scale climate signals in the subtropical North Atlantic. Paleoceanography 29(6), 612-627.

Bolton, C.T., Chang, L., Clemens, S.C., Kodama, K., Ikehara, M., Medina-Elizalde, M., et al., 2013. A 500,000 year record of Indian summer monsoon dynamics recorded by eastern equatorial Indian Ocean upper water-column structure. Quaternary Science Reviews 77, 167-180.

Brovkin, V., Bendtsen, J., Claussen, M., Ganopolski, A., Kubatzki, C., Petoukhov, V., et al., 2002. Carbon cycle, vegetation, and climate dynamics in the Holocene: Experiments with the CLIMBER-2 model. Global Biogeochemical Cycles 16(4), 86-1.

Brovkin, V., Ganopolski, A., Svirezhev, Y., 1997. A continuous climate-vegetation classification for use in climate-biosphere studies. Ecological Modelling 101(2-3), 251-261.

Campin, J.M., Goosse, H., 1999. Parameterization of density-driven downsloping flow for a coarse-resolution ocean model in z-coordinate. Tellus A 51(3), 412-430.

CAPE-Last Interglacial Project Members, 2006. Last Interglacial Arctic warmth confirms polar amplification of climate change. Quaternary Science Reviews 25(13-14), 1383-1400.

Chaisson, W.P., Poli, M.S., Thunell, R.C., 2002. Gulf stream and western boundary undercurrent variations during MIS 10-12 at site 1056, Blake-Bahama Outer Ridge. Marine Geology 189(1-2), 79-105.

Chapman, M.R., Shackleton, N.J., 1998. Millennial-scale fluctuations in North Atlantic heat flux during the last 150,000 years. Earth and Planetary Science Letters 159(1-2), 57-70.

Chen, G., Zheng, H., Li, J., Xie, X., Mei, X., 2008. Dynamic control on grain-size distribution of terrigenous sediments in the western South China Sea: Implication for East Asian monsoon evolution. Chinese Science Bulletin 53(10), 1533-1543.

Cheng, H., Edwards, R.L., Sinha, A., Spötl, C., Yi, L., Chen, S.T., et al., 2016. The Asian monsoon over the past 640,000 years and ice age terminations. Nature 534(7609), 640-646.

Clark, P.U., Alley, R.B., Pollard, D., 1999. Northern Hemisphere Ice-Sheet Influences on Global Climate Change. Science 286, 1104-1111.

Clark, P.U., Pisias, N.G., Stocker, T.F., Weaver, A.J., 2002. The role of the thermohaline circulation in abrupt climate change. Nature 415(6874), 863-869.

Claussen, M., Fohlmeister, J., Ganopolski, A., Brovkin, V., 2006. Vegetation dynamics amplifies precessional forcing. Geophysical Research Letters 33, L09709.

Clement, A.C., Cane, M.A., Seager, R., 2001. An orbitally driven tropical source for abrupt climate change. Journal of Climate 14(11), 2369-2375.

Cox, P.M., Huntingford, C., Williamson, M.S., 2018. Emergent constraint on equilibrium climate sensitivity from global temperature variability. Nature 553(7688), 319-322.

Cramer, W., Bondeau, A., Woodward, F.I., Prentice, I.C., Betts, R.A., Brovkin, V., et al., 2001. Global response of terrestrial ecosystem structure and function to CO_2 and climate change: results from six dynamic global vegetation models. Global Change Biology 7(4), 357-373.

Cronin, T.M., Dwyer, G.S., Caverly, E.K., Farmer, J., DeNinno, L.H., Rodriguez-Lazaro, J., et al., 2017. Enhanced Arctic amplification began at the Mid-Brunhes Event ~400,000 years ago. Scientific Reports 7(1), 1-7.

Cronin, T.M., Gemery, L., Briggs, JrWM., Jakobsson, M., Polyak, L., Brouwers, E.M., 2010. Quaternary Sea-ice history in the Arctic Ocean based on a new Ostracode sea-ice proxy. Quaternary Science Reviews 29(25-26), 3415-3429.

Cronin, T.M., Polyak, L., Reed, D., Kandiano, E.S., Marzen, R.E., Council, E.A., 2013. A 600-ka Arctic sea-ice record from Mendeleev Ridge based on ostracodes. Quaternary Science Reviews 79, 157-167.

Crucifix, M., Loutre, M.F., Tulkens, P., Fichefet, T., Berger, A., 2002. Climate evolution during the Holocene: A study with an earth system model of intermediate complexity. Climate Dynamics 19(1), 43-60.

Dang, H., Wu, J., Xiong, Z., Qiao, P., Li, T., Jian, Z., 2020. Orbital and sea-level changes regulate the iron-associated sediment supplies from Papua New Guinea to the equatorial Pacific. Quaternary Science Reviews 239, 106361.

de Garidel-Thoron, T., Rosenthal, Y., Bassinot, F., Beaufort, L., 2005. Stable sea surface temperatures in the western Pacific warm pool over the past 1.75 million years. Nature 433(7023), 294-298.

de Vernal, A., Hillaire-Marcel, C., Le Duc, C., Roberge, P., Brice, C., Matthiessen, J., et al., 2020. Natural variability of the Arctic Ocean sea ice during the present interglacial. Proceedings of the National Academy of Sciences 117(42), 26069-26075.

Delille, B., Vancoppenolle, M., Geilfus, N.X., Tilbrook, B., Lannuzel, D., Schoemann, V., et al., 2014. Southern Ocean CO_2 sink: The contribution of the sea ice. Journal of Geophysical Research: Oceans 119(9), 6340-6355.

Delmotte, M., Chappellaz, J., Brook, E., Yiou, P., Barnola, J.M., Goujon, C., et al., 2004. Atmospheric methane during the last four glacial-interglacial cycles: Rapid changes and their link with Antarctic temperature. Journal of Geophysical Research: Atmospheres 109, D12104.

Deng, J., Wu, Z., Zhang, M., Huang, N.E., Wang, S., Qiao, F., 2018. Using Holo-Hilbert spectral analysis to quantify the modulation of Dansgaard-Oeschger events by obliquity. Quaternary Science Reviews 192, 282-299.

Déry, S.J., Mlynowski, T.J., Hernández-Henríquez, M.A., Straneo, F., 2011. Interannual variability and interdecadal trends in Hudson Bay streamflow. Journal of Marine Systems 88(3), 341-351.

dos Santos, R.A.L., Prange, M., Castañeda, I.S., Schefuß, E., Mulitza, S., Schulz, M., et al., 2010. Glacial-interglacial variability in Atlantic meridional overturning circulation and thermocline adjustments in the tropical North Atlantic. Earth and Planetary Science Letters 300(3-4), 407-414.

Ducklow, H., Fraser, W.R., Meredith, M.P., Stammerjohn, S.E., Doney, S.C., Douglas, G., 2013. West Antarctic Peninsula: an ice-dependent coastal marine ecosystem in transition. Oceanography 26(3), 190-203.

Duesing, W., Berner, N., Deino, A.L., Foerster, V., Kraemer, K.H., Marwan, N., et al., 2021a. Multiband Wavelet Age Modeling for a ∼293 m (∼600 kyr) Sediment Core From Chew Bahir Basin, Southern Ethiopian Rift. Frontiers in Earth Science 35.

Duesing, W., Kaboth-Bahr, S., Asrat, A., Cohen, A.S., Foerster, V., Lamb, H.F., et al., 2021b. Changes in the cyclicity and variability of the eastern African paleoclimate over the last 620 kyrs. Quaternary Science Reviews 273, 107219.

Dutton, A., Carlson, A.E., Long, A.J., Milne, G.A., Clark, P.U., DeConto, R., et al., 2015. Sea-level rise due to polar ice-sheet mass loss during past warm periods. Science 349(6244), aaa4019.

Emanuele, D., Ferretti, P., Palumbo, E., Amore, F.O., 2015. Sea-surface dynamics and palaeoenvironmental changes in the North Atlantic Ocean (IODP Site U1313) during Marine Isotope Stage 19 inferred from coccolithophore assemblages. Palaeogeography, Palaeoclimatology, Palaeoecology 430, 104-117.

Fawcett, P.J., Werne, J.P., Anderson, R.S., Heikoop, J.M., Brown, E.T., Berke, M.A., et al., 2011. Extended megadroughts in the southwestern United States during Pleistocene interglacials. Nature 470(7335), 518-521.

Ferretti, P., Crowhurst, S.J., Hall, M.A., Cacho, I., 2010. North Atlantic millennial-scale climate variability 910 to 790 ka and the role of the equatorial insolation forcing. Earth and Planetary Science Letters 293(1-2), 28-41.

Ferretti, P., Crowhurst, S.J., Naafs, B.D.A., Barbante, C., 2015. The Marine Isotope Stage 19 in the mid-latitude North Atlantic Ocean: astronomical signature and intra-interglacial variability. Quaternary Science Reviews 108, 95-110.

Friedrich, T., Timmermann, A., Menviel, L., Timm, O.E., Mouchet, A., Roche, D.M., 2010. The mechanism behind internally generated centennial-to-millennial scale climate variability in an earth system model of intermediate complexity. Geoscientific Model Development 3(2), 377-389.

Galaasen, E.V., Ninnemann, U.S., Kessler, A., Irvalı, N., Rosenthal, Y., Tjiputra, J., et al., 2020. Interglacial instability of North Atlantic deep water ventilation. Science 367(6485), 1485-1489.

Ganopolski, A., Calov, R., 2011. The role of orbital forcing, carbon dioxide and regolith in 100 kyr glacial cycles. Climate of the Past 7, 1415-1425.

Ganopolski, A., Roche, D.M., 2009. On the nature of lead-lag relationships during glacial-interglacial climate transitions. Quaternary Science Reviews 28(27-28), 3361-3378.

Goñi, M.F.S., Ferretti, P., Polanco-Martínez, J.M., Rodrigues, T., Alonso-García, M., Rodríguez-Tovar, F.J., et al., 2019. Pronounced northward shift of the westerlies during MIS 17 leading to the strong 100-kyr ice age cycles. Earth and Planetary Science Letters 511, 117-129.

Goñi, M.F.S., Rodrigues, T., Hodell, D.A., Polanco-Martinez, J.M., Alonso-Garcia, M., Hernandez-Almeida, I., et al., 2016. Tropically-driven climate shifts in southwestern Europe during MIS-19, a low eccentricity interglacial. Earth and Planetary Science Letters 448, 81-93.

Goosse, H., Brovkin, V., Fichefet, T., Haarsma, R., Huybrechts, P., Jongma, J., et al., 2010. Description of the Earth system model of intermediate complexity LOVECLIM version 1.2. Geoscientific Model Development 3, 603-633.

Goosse, H., Fichefet, T., 1999. Importance of ice-ocean interactions for the global ocean circulation: A model study. Journal of Geophysical Research: Oceans 104(C10), 23337-23355.

Goosse, H., Renssen, H., 2001. A two-phase response of the Southern Ocean to an increase in greenhouse gas concentrations. Geophysical Research Letters 28(18), 3469-3472.

Goosse, H., Roche, D.M., Mairesse, A., Berger, M., 2013. Modelling past sea ice changes. Quaternary Science Reviews 79, 191-206.

Goosse, H., Selten, F.M., Haarsma, R.J., Opsteegh, J.D., 2001. Decadal variability in high northern latitudes as simulated by an intermediate-complexity climate model. Annals of Glaciology 33, 525-532.

Grützner, J., Giosan, L., Franz, S.O., Tiedemann, R., Cortijo, E., Chaisson, W.P., et al., 2002. Astronomical age models for Pleistocene drift sediments from the western North Atlantic (ODP Sites 1055-1063). Marine Geology 189(1-2), 5-23.

Guarino, M.V., Sime, L.C., Schröeder, D., Malmierca-Vallet, I., Rosenblum, E., Ringer, M., et al., 2020. Sea-ice-free Arctic during the Last Interglacial supports fast future loss. Nature Climate Change 10(10), 928-932.

Guo, Z., Berger, A., Yin, Q., Qin, L., 2009. Strong asymmetry of hemispheric climates during MIS-13 inferred from correlating China loess and Antarctica ice records. Climate of the Past 5(1), 21-31.

Guo, Z., Liu, T., Fedoroff, N., Wei, L., Ding, Z., Wu, N., et al., 1998. Climate extremes in loess of China coupled with the strength of deep-water formation in the North Atlantic. Global and Planetary Change 18(3-4), 113-128.

Guo, Z., Zhou, X., Wu, H., 2012. Glacial-interglacial water cycle, global monsoon and atmospheric methane changes. Climate Dynamics 39(5), 1073-1092.

Gupta, S. M., 2002. Pyloniid stratigraphy-a new tool to date tropical radiolarian ooze from the central tropical Indian Ocean. Marine Geology 184(1-2), 85-93.

Gupta, S.M., 2003. Orbital frequencies in radiolarian assemblages of the central Indian Ocean: implications on the Indian summer monsoon. Palaeogeography, Palaeoclimatology, Palaeoecology 197(1-2), 97-112.

Hagelberg, T.K., Bond, G., Demenocal, P., 1994. Milankovitch band forcing of sub-Milankovitch climate variability during the Pleistocene. Paleoceanography 9(4), 545-558.

Hall, I.R., Becker, J., 2007. Deep Western Boundary Current variability in the subtropical northwest Atlantic Ocean during marine isotope stages 12-10. Geochemistry, Geophysics, Geosystems 8(6).

Han, X., Jin, X., Yang, S., Fietzke, J., Eisenhauer, A., 2003. Rhythmic growth of Pacific ferromanganese nodules and their Milankovitch climatic origin. Earth and Planetary Science Letters 211(1-2), 143-157.

Han, X., Qiu, Z., Ma, W., Qian, J., 2009. High-resolution dating of Co-rich crusts: A comparative study using the methods of orbital pacing and 230Thex/232Th dating. Science in China Series D: Earth Sciences 52(4), 484-488.

Haneda, Y., Okada, M., Kubota, Y., Suganuma, Y., 2020 Millennial-scale hydrographic changes in the northwestern Pacific during marine isotope stage 19: teleconnections with ice melt in the North Atlantic. Earth and Planetary Science Letters 531, 115936.

Hansen, J., Lacis, A., Rind, D., Russell, G., Stone, P., Fung, I., et al., 1984. Climate sensitivity: analysis of feedback mechanisms. Climate processes and climate sensitivity 5(29), 130-163.

Hao, Q., Wang, L., Oldfield, F., Peng, S., Qin, L., Song, Y., et al., 2012. Delayed build-up of Arctic ice sheets during 400,000-year minima in insolation variability. Nature 490(7420), 393-396.

Heinrich, H., 1988. Origin and consequences of cyclic ice rafting in the northeast Atlantic Ocean during the past 130,000 years. Quaternary research 29(2), 142-152.

Herbert, T.D., Peterson, L.C., Lawrence, K.T., Liu, Z., 2010. Tropical ocean temperatures over the past 3.5 million years. Science 328(5985), 1530-1534.

Hernández-Almeida, I., Sierro, F.J., Cacho, I., Flores, J.A., 2012. Impact of suborbital climate change in the North Atlantic on ice sheet dynamics at the Mid-Pleistocene Transition. Paleoceanography 27, PA3214.

Hinnov, L.A., Schulz, M., Yiou, P., 2002. Interhemispheric space–time attributes of the Dansgaard-Oeschger oscillations between 100 and 0 ka. Quaternary Science Reviews 21(10), 1213-1228.

Hobbs, W.R., Massom, R., Stammerjohn, S., Reid, P., Williams, G., Meier, W., 2016. A review of recent changes in Southern Ocean sea ice, their drivers and forcings. Global and Planetary Change 143, 228-250.

Hodell, D.A., Channell, J.E., 2016. Mode transitions in Northern Hemisphere glaciation: co-evolution of millennial and orbital variability in Quaternary climate. Climate of the Past, 12(9), 1805-1828.

Hodell, D.A., Crowhurst, S., Skinner, L., Tzedakis, P.C., Margari, V., Channell, J.E., et al., 2013. Response of Iberian Margin sediments to orbital and suborbital forcing over the past 420 ka. Paleoceanography 28(1), 185-199.

Hodell, D.A., Lourens, L., Crowhurst, S., Konijnendijk, T., Tjallingii, R., Jiménez-Espejo, F., et al., 2015. A reference time scale for Site U1385 (Shackleton Site) on the SW Iberian Margin. Global and Planetary Change 133, 49-64.

Holden, P.B., Edwards, N.R., Wolff, E.W., Valdes, P.J., Singarayer, J.S., 2011. The Mid-Brunhes Event and West Antarctic ice sheet stability. Journal of Quaternary Science 26(5), 474-477.

Hopley, P.J., Weedon, G.P., Marshall, J.D., Herries, A.I., Latham, A.G., Kuykendall, K.L., 2007. High-and low-latitude orbital forcing of early hominin habitats in South Africa. Earth and Planetary Science Letters 256(3-4), 419-432.

Howard, W.R., Prell, W.L., 1992. Late Quaternary surface circulation of the southern Indian Ocean and its relationship to orbital variations. Paleoceanography 7(1), 79-117.

Huybrechts, P., 2002. Sea-level changes at the LGM from ice-dynamic reconstructions of the Greenland and Antarctic ice sheets during the glacial cycles. Quaternary Science Reviews 21(1-3), 203-231.

IPCC, 2021. Summary for Policymakers. In: Climate Change 2021: The Physical Science Basis. Contribution of Working Group I to the Sixth Assessment Report of the Intergovernmental Panel on Climate Change. Cambridge University Press.

Ivory, S.J., Blome, M.W., King, J.W., McGlue, M.M., Cole, J.E., Cohen, A.S., 2016. Environmental change explains cichlid adaptive radiation at Lake Malawi over the past 1.2 million years. Proceedings of the National Academy of Sciences 113(42), 11895-11900.

Jansen, J.H.F., Kuijpers, A., Troelstra, S.R.A., 1986. Mid-Brunhes climatic event: long-term changes in global atmosphere and ocean circulation. Science 232, 619-622.

Jian, Z., Wang, Y., Dang, H., Lea, D.W., Liu, Z., Jin, H., et al., 2020. Half-precessional cycle of thermocline temperature in the western equatorial Pacific and its bihemispheric dynamics. Proceedings of the National Academy of Sciences 117(13), 7044-7051.

Joannin, S., Bassinot, F., Nebout, N.C., Peyron, O., Beaudouin, C., 2011. Vegetation response to obliquity and precession forcing during the Mid-Pleistocene Transition in Western Mediterranean region (ODP site 976). Quaternary Science Reviews 30(3-4), 280-297.

Jouzel, J., Masson-Delmotte, V., Cattani, O., Dreyfus, G., Falourd, S., Hoffmann, G., et al., 2007. Orbital and millennial antarctic climate variability over the past 800,000 years. Science 317(5839), 793-796.

Jungclaus, J.H., Bard, E., Baroni, M., Braconnot, P., Cao, J., Chini, L.P., et al., 2017. The PMIP4 contribution to CMIP6-Part 3: The last millennium, scientific objective, and experimental design for the PMIP4 past1000 simulations. Geoscientific Model Development 10(11), 4005-4033.

Kageyama, M., Albani, S., Braconnot, P., Harrison, S.P., Hopcroft, P.O., Ivanovic, R.F., et al., 2017. The PMIP4 contribution to CMIP6-Part 4: Scientific objectives and experimental design of the PMIP4-CMIP6 Last Glacial Maximum experiments and PMIP4 sensitivity experiments. Geoscientific Model Development 10(11), 4035-4055.

Kageyama, M., Braconnot, P., Harrison, S.P., Haywood, A.M., Jungclaus, J.H., Otto-Bliesner, B.L., et al., 2018. The PMIP4 contribution to CMIP6–Part 1: Overview and over-arching analysis plan. Geoscientific Model Development 11(3), 1033-1057.

Kageyama, M., Sime, L.C., Sicard, M., Guarino, M.V., de Vernal, A., Stein, R., et al., 2021. A multi-model CMIP6-PMIP4 study of Arctic sea ice at 127 ka: sea ice data compilation and model differences. Climate of the Past 17(1), 37-62.

Kidston, J., Taschetto, A.S., Thompson, D.W.J., England, M.H., 2011. The influence of Southern Hemisphere sea-ice extent on the latitude of the mid-latitude jet stream. Geophysical Research Letters 38(15), 532-560.

Krinner, G., Magand, O., Simmonds, I., Genthon, C., Dufresne, J.L., 2007. Simulated Antarctic precipitation and surface mass balance at the end of the twentieth and twenty-first centuries. Climate Dynamics 28(2-3), 215-230.

Kukla, G., Berger, A., Lotti, R., Brown, J., 1981. Orbital signature of interglacials. Nature 290(5804), 295-300.

Laepple, T., Lohmann, G., 2009. Seasonal cycle as template for climate variability on astronomical timescales. Paleoceanography 24(4), PA4201.

Lang, N., Wolff, E.W., 2011. Interglacial and glacial variability from the last 800 ka in marine, ice and terrestrial archives. Climate of the Past 7(2), 361-380.

Lawrence, K.T., Herbert, T.D., Brown, C.M., Raymo, M.E., Haywood, A.M., 2009. High-amplitude variations in North Atlantic sea surface temperature during the early Pliocene warm period. Paleoceanography 24(2), PA2212.

Le Treut, H., Ghil, M., 1983. Orbital forcing, climatic interactions, and glaciation cycles. Journal of Geophysical Research: Oceans 88(C9), 5167-5190.

Le Treut, H., Portes, J., Jouzel, J., Ghil, M., 1988. Isotopic modeling of climatic oscillations: Implications for a comparative study of marine and ice core records. Journal of Geophysical Research: Atmospheres 93(D8), 9365-9383.

Li, L., Li, Q., Tian, J., Wang, P., Wang, H., Liu, Z., 2011. A 4-Ma record of thermal evolution in the tropical western Pacific and its implications on climate change. Earth and Planetary Science Letters 309(1-2), 10-20.

Li, T., Zhao, J., Nan, Q., Sun, R., Yu, X., 2011. Palaeoproductivity evolution in the centre of the western Pacific warm pool during the last 250 ka. Journal of Quaternary Science 26(5), 478-484.

Liakka, J., Lofverstrom, M., 2018. Arctic warming induced by the Laurentide Ice Sheet topography. Climate of the Past 14(6), 887-900.

Lindberg, K.R., Daniels, W.C., Castañeda, I.S., Brigham-Grette, J., 2022. Biomarker proxy records of Arctic climate change during the Mid-Pleistocene transition from Lake El'gygytgyn (Far East Russia). Climate of the Past 18(3), 559-577.

Lisiecki, L.E., Raymo, M.E., 2005. A Pliocene-Pleistocene stack of 57 globally distributed benthic $\delta^{18}O$ records. Paleoceanography 20(1), PA001071.

Liu, Z., Herbert, T.D., 2004. High-latitude influence on the eastern equatorial Pacific climate in the early Pleistocene epoch. Nature 427(6976), 720-723.

Liu, Z., Zhao, Y., Li, J., Colin, C., 2007. Late Quaternary clay minerals off Middle Vietnam in the western South China Sea: Implications for source analysis and East Asian monsoon evolution. Science in China Series D: Earth Sciences 50(11), 1674-1684.

Lo, L., Belt, S.T., Lattaud, J., Friedrich, T., Zeeden, C., Schouten, S., et al., 2018. Precession and atmospheric CO2 modulated variability of sea ice in the central Okhotsk Sea since 130,000 years ago. Earth and Planetary Science Letters 488, 36-45.

Lo, L., Shen, C., Zeeden, C., Tsai, Y.H., Yin, Q., Yang, C., et al., 2022. Orbital control on the thermocline structure during the past 568 kyr in the Solomon Sea, southwest equatorial Pacific. Quaternary Science Reviews, 295, 107756.

Lochte, A.A., Repschläger, J., Kienast, M., Garbe-Schönberg, D., Andersen, N., Hamann, C., et al., 2019. Labrador Sea freshening at 8.5 ka BP caused by Hudson Bay Ice Saddle collapse. Nature Communications 10(1), 1-9.

Lochte, A.A., Schneider, R., Kienast, M., Repschläger, J., Blanz, T., Garbe-Schönberg, D., et al., 2020. Surface and subsurface Labrador Shelf water mass conditions during the last 6000 years. Climate of the Past 16(4), 1127-1143.

Loulergue, L., Schilt, A., Spahni, R., Masson-Delmotte, V., Blunier, T., Lemieux, B., et al., 2008. Orbital and millennial-scale features of atmospheric CH_4 over the past 800,000 years. Nature 453, 383-386.

Loutre, M. F., Paillard, D., Vimeux, F., Cortijo, E., 2004. Does mean annual insolation have the potential to change the climate?. Earth and Planetary Science Letters 221(1-4), 1-14.

Loutre, M.F., Berger, A., 2003. Marine Isotope Stage 11 as an analogue for the present interglacial. Global and Planetary Change 36(3), 209-217.

Loutre, M.F., Fichefet, T., Goosse, H., Huybrechts, P., Goelzer, H., Capron, E., 2014. Factors controlling the last interglacial climate as simulated by LOVECLIM1.3. Climate of the Past 10(4), 1541-1565.

Lu, Z., Liu, Z., Chen, G., Guan, J., 2019. Prominent precession band variance in ENSO intensity over the last 300,000 years. Geophysical Research Letters 46(16), 9786-9795.

Lunt, D.J., Abe-Ouchi, A., Bakker, P., Berger, A., Braconnot, P., Charbit, S., et al., 2013. A multi-model assessment of last interglacial temperatures. Climate of the Past 9(2), 699-717.

Luo, Y., Sun, X., Jian, Z., 2005. Environmental change during the penultimate glacial cycle: a high-resolution pollen record from ODP Site 1144, South China Sea. Marine Micropaleontology 54(1-2), 107-123.

Lupien, R.L., Russell, J.M., Subramanian, A., Kinyanjui, R., Beverly, E.J., Uno, K.T., et al., 2021. Eastern African environmental variation and its role in the evolution and cultural change of Homo over the last 1 million years. Journal of Human Evolution 157, 103028.

Lüthi, D., Le Floch, M., Bereiter, B., Blunier, T., Barnola, J. M., Siegenthaler, U., et al., 2008. High-resolution carbon dioxide concentration record 650,000-800,000 years before present. Nature 453(7193), 379-382.

Lyu, A., Yin, Q., 2022. The spatial-temporal patterns of East Asian climate in response to insolation, CO_2 and ice sheets during MIS-5. Quaternary Science Reviews 293, 107689.

Manabe, S., Wetherald, R.T., 1967. Thermal equilibrium of the atmosphere with a given distribution of relative humidity. Journal of the Atmospheric Sciences 24(3), 241-259.

Martínez-Garcia, A., Rosell-Melé, A., McClymont, E.L., Gersonde, R., Haug, G.H., 2010. Subpolar link to the emergence of the modern equatorial Pacific cold tongue. Science 328(5985), 1550-1553.

Martinez-Sanchez, M., Flores, J.A., Palumbo, E., Alonso-Garcia, M., Sierro, F.J., Amore, F.O., 2019. Reconstruction of surface water dynamics in the North Atlantic during the Mid-Pleistocene (~540-400 ka), as inferred from coccolithophores and planktonic foraminifera. Marine Micropaleontology 152, 101730.

Martrat, B., Grimalt, J.O., Shackleton, N.J., de Abreu, L., Hutterli, M.A., Stocker, T.F., 2007. Four climate cycles of recurring deep and surface water destabilizations on the Iberian margin. Science 317(5837), 502-507.

Mayewski, P.A., Meeker, L.D., Twickler, M.S., Whitlow, S., Yang, Q., Lyons, W.B., et al., 1997. Major features and forcing of high-latitude northern hemisphere atmospheric circulation using a 110,000-year-long glaciochemical series. Journal of Geophysical Research: Oceans 102(C12), 26345-26366.

McIntyre, A., Molfino, B., 1996. Forcing of Atlantic equatorial and subpolar millennial cycles by precession. Science 274(5294), 1867-1870.

McManus, J., Oppo, D., Cullen, J., Healey, S., 2003. Marine isotope stage 11 (MIS 11): analog for holocene and future climate? In: Droxler, A., Burckle, L., Poore, A. (Eds.), Earth Climate and Orbital Eccentricity: the Marine Isotope Stage 11 Question, Geophysical Monograph, vol. 137. American Geophysical Union, pp. 69-85.

Meccia, V.L., Mikolajewicz, U., 2018. Interactive ocean bathymetry and coastlines for simulating the last deglaciation with the Max Planck Institute Earth System Model (MPI-ESM-v1. 2). Geoscientific Model Development 11(11), 4677-4692.

Medina-Elizalde, M., Lea, D.W., 2005. The mid-Pleistocene transition in the tropical Pacific. Science 310(5750), 1009-1012.

Melice, J.L., Servain, J., 2003. The tropical Atlantic meridional SST gradient index and its relationships with the SOI, NAO and Southern Ocean. Climate Dynamics 20(5), 447-464.

Mellor, G.L., Yamada, T., 1982. Development of a turbulence closure model for geophysical fluid problems. Reviews of Geophysics 20(4), 851-875.

Mommersteeg, H.J.P.M., Loutre, M.F., Young, R., Wijmstra, T.A., Hooghiemstra, H., 1995. Orbital forced frequencies in the 975000 year pollen record from Tenagi Philippon (Greece). Climate Dynamics 11, 4-24.

Mouchet, A., François, L.M., 1996. Sensitivity of a global oceanic carbon cycle model to the circulation and to the fate of organic matter: Preliminary results. Physics and Chemistry of the Earth 21(5-6), 511-516.

Muri, H., Berger, A., Yin, Q., Karami, M.P., Barriat, P.Y., 2013. The climate of the MIS-13 interglacial according to HadCM3. Journal of Climate 26(23), 9696-9712.

Muri, H., Berger, A., Yin, Q., Voldoire, A., Mélia, D.S.Y., Sundaram, S., 2012. SST and ice sheet impacts on the MIS-13 climate. Climate Dynamics 39, 1739-1761.

Myhre, G., Myhre, C.L., Forster, P.M., Shine, K.P., 2017. Halfway to doubling of CO_2 radiative forcing. Nature Geoscience 10(10), 710-711.

Nascimento, R.A., Venancio, I.M., Chiessi, C.M., Ballalai, J.M., Kuhnert, H., Johnstone, H., et al., 2021. Tropical Atlantic stratification response to late Quaternary precessional forcing. Earth and Planetary Science Letters 568, 117030.

NEEM community members, 2013. Eemian interglacial reconstructed from a Greenland folded ice core. Nature 493(7433), 489-494.

Nijsse, F.J.M.M., Cox, P.M., Williamson, M.S., 2020. Emergent constraints on transient climate response (TCR) and equilibrium climate sensitivity (ECS) from historical warming in CMIP5 and CMIP6 models. Earth System Dynamics 11(3), 737-750.

Olago, D.O., Street-Perrott, F.A., Perrott, R.A., Ivanovich, M., Harkness, D.D., Odada, E.O., 2000. Long-term temporal characteristics of palaeomonsoon dynamics in equatorial Africa. Global and Planetary Change 26(1-3), 159-171.

Oliveira, D., Desprat, S., Yin, Q., Naughton, F., Trigo, R., Rodrigues, T., et al., 2018. Unraveling the forcings controlling the vegetation and climate of the best orbital analogues for the present interglacial in SW Europe. Climate Dynamics 51(1-2), 667-686.

Olson, S.L., Hearty, P.J., 2009. A sustained +21 m sea-level highstand during MIS 11 (400 ka): direct fossil and sedimentary evidence from Bermuda. Quaternary Science Reviews 28(3-4), 271-285.

O'Neill, B.C., Tebaldi, C., Vuuren, D.P.V., Eyring, V., Friedlingstein, P., Hurtt, G., et al., 2016. The scenario model intercomparison project (ScenarioMIP) for CMIP6. Geoscientific Model Development 9(9), 3461-3482.

Opsteegh, J.D., Haarsma, R.J., Selten, F.M., Kattenberg, A., 1998. ECBILT: A dynamic alternative to mixed boundary conditions in ocean models. Tellus A: Dynamic Meteorology and Oceanography 50(3), 348-367.

Ortiz, J., Mix, A., Harris, S., O'Connell, S., 1999. Diffuse spectral reflectance as a proxy for percent carbonate content in North Atlantic sediments. Paleoceanography 14(2), 171-186.

Otto-Bliesner, B.L., Brady, E.C., Fasullo, J., Jahn, A., Landrum, L., Stevenson, S., et al., 2016. Climate variability and change since 850 CE: An ensemble approach with the Community Earth System Model. Bulletin of the American Meteorological Society 97(5), 735-754.

Otto-Bliesner, B.L., Brady, E.C., Tomas, R.A., Albani, S., Bartlein, P.J., Mahowald, N.M., et al., 2020. A comparison of the CMIP6 midHolocene and lig127k simulations in CESM2. Paleoceanography and Paleoclimatology 35(11), e2020PA003957.

Otto-Bliesner, B.L., Brady, E.C., Zhao, A., Brierley, C.M., Axford, Y., Capron, E., et al., 2021. Large-scale features of Last Interglacial climate: results from evaluating the lig127k simulations for the Coupled Model Intercomparison Project (CMIP6)-Paleoclimate Modeling Intercomparison Project (PMIP4). Climate of the Past 17(1), 63-94.

Palumbo, E., Flores, J.A., Perugia, C., Petrillo, Z., Voelker, A.H.L., Amore, F.O., 2013. Millennial scale coccolithophore paleoproductivity and surface water changes between 445 and 360 ka (Marine Isotope Stages 12/11) in the Northeast Atlantic. Palaeogeography, Palaeoclimatology, Palaeoecology 383, 27-41.

Palumbo, E., Voelker, A.H., Flores, J.A., Amore, O.F., 2019. Surface-ocean dynamics during eccentricity minima: a comparison between interglacial Marine Isotope Stage (MIS) 1 and MIS 11 on the Iberian Margin. Global and Planetary Change 172, 242-255.

Past Interglacials Working Group of PAGES, 2016. Interglacials of the last 800,000 years. Reviews of Geophysics 54(1), 162-219.

Pestiaux, P., Van der Mersch, I., Berger, A., Duplessy, J.C., 1988. Paleoclimatic variability at frequencies ranging from 1 cycle per 10000 years to 1 cycle per 1000 years: Evidence for nonlinear behaviour of the climate system. Climatic Change 12, 9-37.

Pisias, N.G., Rea, D.K., 1988. Late pleistocene paleoclimatology of the central equatorial pacific: sea surface response to the southeast trade winds. Paleoceanography 3(1), 21-37.

Pokras, E.M., Mix, A.C., 1987. Earth's precession cycle and Quaternary climatic change in tropical Africa. Nature 326(6112), 486-487.

Pol, K., Masson-Delmotte, V., Johnsen, S., Bigler, M., Cattani, O., Durand, G., et al., 2010. New MIS 19 EPICA Dome C high resolution deuterium data: Hints for a problematic preservation of climate variability at sub-millennial scale in the “oldest ice”. Earth and Planetary Science Letters 298(1-2), 95-103.

Polyak. L., Alley, R.B., Andrews, J.T., Grette, J.B., Cronin, T.M., Darby, D.A., et al., 2010. History of sea ice in the Arctic. Quaternary Science Reviews 29(15-16), 1757-1778.

Raymo, M.E., Mitrovica, J.X., 2012. Collapse of polar ice sheets during the stage 11 interglacial. Nature 483(7390), 453-456.

Raynaud, D., Lipenkov, V., Lemieux-Dudon, B., Duval, P., Loutre, M.F., Lhomme, N., 2007. The local insolation signature of air content in Antarctic ice. A new step toward an absolute dating of ice records. Earth and Planetary Science Letters 261(3-4), 337-349.

Rennermalm, A.K., Wood, E.F., Weaver, A.J., Eby, M., Déry, S.J., 2007. Relative sensitivity of the Atlantic meridional overturning circulation to river discharge into Hudson Bay and the Arctic Ocean. Journal of Geophysical Research: Biogeosciences 112(G4).

Renssen, H., Seppä, H., Heiri, O., Roche, D.M., Goosse, H., Fichefet, T., 2009. The spatial and temporal complexity of the Holocene thermal maximum. Nature Geoscience 2(6), 411-414.

Roberts, W.H., Valdes, P.J., 2017. Green Mountains and White Plains: the effect of Northern Hemisphere ice sheets on the global energy budget. Journal of Climate 30(10), 3887-3905.

Rowe, M.P., Wainer, K.A., Bristow, C.S., Thomas, A.L., 2014. Anomalous MIS 7 sea level recorded on Bermuda. Quaternary Science Reviews 90, 47-59.

Ruddiman, W.F., 2007. The early anthropogenic hypothesis: Challenges and responses. Reviews of Geophysics 45(4), RG000207.

Ruddiman, W.F., Raymo, M., Martinson, D.G., Clement, B.M., Backman, J., 1989. Pleistocene evolution: Northern hemisphere ice sheets and North Atlantic Ocean. Paleoceanography 4(4), 353-412.

Rugenstein, M., Bloch-Johnson, J., Gregory, J., Andrews, T., Mauritsen, T., Li, C., et al., 2020. Equilibrium climate sensitivity estimated by equilibrating climate models. Geophysical Research Letters 47(4), e2019GL083898.

Rutherford, S., D'Hondt, S., 2000. Early onset and tropical forcing of 100,000-year Pleistocene glacial cycles. Nature 408(6808), 72-75.

Rzechowski, J., 2020. The Ferdynandowian Interglacial and its stratigraphical position in the Middle Pleistocene of Europe. In The early Middle Pleistocene in Europe (pp. 279-293). CRC Press.

Schaefer, G., Rodger, J.S., Hayward, B.W., Kennett, J.P., Sabaa, A.T., Scott, G.H., 2005. Planktic foraminiferal and sea surface temperature record during the last 1 Myr across the Subtropical Front, Southwest Pacific. Marine Micropaleontology 54(3-4), 191-212.

Schilt, A., Baumgartner, M., Blunier, T., Schwander, J., Spahni, R., Fischer, H., et al., 2010. Glacial-interglacial and millennial-scale variations in the atmospheric nitrous oxide concentration during the last 800,000 years. Quaternary Science Reviews 29(1-2), 182-192.

Serreze, M.C., Barry, R.G., 2011. Processes and impacts of Arctic amplification: A research synthesis. Global and Planetary Change 77(1-2), 85-96.

Serreze, M.C., Stroeve, J., Barrett, A.P., Boisvert, L.N., 2016. Summer atmospheric circulation anomalies over the Arctic Ocean and their influences on September sea ice extent: A cautionary tale. Journal of Geophysical Research: Atmospheres 121(19), 11463-11485.

Sherriff-Tadano, S., Abe-Ouchi, A., 2020. Roles of sea ice-surface wind feedback in maintaining the glacial Atlantic meridional overturning circulation and climate. Journal of Climate 33(8), 3001-3018.

Shi, F., Yin, Q., Nikolova, I., Berger, A., Ramstein G., Guo, Z., 2020. Impacts of extremely asymmetrical polar ice sheets on the East Asian summer monson during the MIS-13 interglacial. Quaternary Science Reviews 230, 106164.
Short, D.A., Mengel, J.G., Crowley, T.J., Hyde, W.T., North, G.R., 1991. Filtering of Milankovitch cycles by Earth's geography. Quaternary Research 35(2), 157-173.
Singarayer, J.S., Valdes, P.J., Friedlingstein, P., Nelson, S., Beerling, D.J., 2011. Late holocene methane rise caused by orbitally controlled increase in tropical sources. Nature 470(7332), 82-85.
Smith, R.S., Gregory, J., 2012. The last glacial cycle: transient simulations with an AOGCM. Climate Dynamics 38(7), 1545-1559.
Stein, R., Fahl, K., Gierz, P., Niessen, F., Lohmann, G., 2017. Arctic Ocean sea ice cover during the penultimate glacial and the last interglacial. Nature Communications 8(1), 1-13.
Straneo, F., Saucier, F., 2008. The outflow from Hudson Strait and its contribution to the Labrador Current. Deep Sea Research Part I: Oceanographic Research Papers 55(8), 926-946.
Su, Q., Lyu, A., Wu, Z., Yin, Q., 2022. Diverse response of global terrestrial vegetation to astronomical forcing and CO_2 during the MIS-11 and MIS-13 interglacials. Climate Dynamics 1-18.
Sümegi, P., Gulyás, S., Molnár, D., Sümegi, B.P., Törőcsik, T., Almond, P.C., et al., 2019. Periodicities of paleoclimate variations in the first high-resolution non-orbitally tuned grain size record of the past 1 Ma from SW Hungary and regional, global correlations. Aeolian Research 40, 74-90.
Sun, J., Huang, X., 2006. Half-precessional cycles recorded in Chinese loess: response to low-latitude insolation forcing during the Last Interglaciation. Quaternary Science Reviews 25(9-10), 1065-1072.
Sun, X., Luo, Y., Huang, F., Tian, J., Wang, P., 2003. Deep-sea pollen from the South China Sea: Pleistocene indicators of East Asian monsoon. Marine Geology 201(1-3), 97-118.

Sun, Y., McManus, J.F., Clemens, S.C., Zhang, X., Vogel, H., Hodell, D.A., et al., 2021a. Persistent orbital influence on millennial climate variability through the Pleistocene. Nature Geoscience 14(11), 812-818.

Sun, Y., Clemens, S.C., Guo, F., Liu, X., Wang, Y., Yan, Y., et al., 2021b. High-sedimentation-rate loess records: A new window into understanding orbital-and millennial-scale monsoon variability. Earth-Science Reviews 220, 103731.

Tan, N., Contoux, C., Ramstein, G., Sun, Y., Dumas, C., Sepulchre, P., et al., 2020. Modeling a modern-like pCO_2 warm period (Marine Isotope Stage KM5c) with two versions of an Institut Pierre Simon Laplace atmosphere–ocean coupled general circulation model. Climate of the Past 16(1), 1-16.

Tang, Z., Li, T., Chang, F., Nan, Q., Li, Q., 2013. Paleoproductivity evolution in the West Philippine Sea during the last 700 ka. Chinese Journal of Oceanology and Limnology 31(2), 435-444.

Thevenon, F., Bard, E., Williamson, D., Beaufort, L., 2004. A biomass burning record from the West Equatorial Pacific over the last 360 ky: methodological, climatic and anthropic implications. Palaeogeography, Palaeoclimatology, Palaeoecology 213(1-2), 83-99.

Thomas, E.K., Clemens, S.C., Sun, Y., Prell, W.L., Huang, Y., Gao, L., et al., 2016. Heterodynes dominate precipitation isotopes in the East Asian monsoon region, reflecting interaction of multiple climate factors. Earth and Planetary Science Letters 455, 196-206.

Thornalley, D.J., Oppo, D.W., Ortega, P., Robson, J.I., Brierley, C.M., Davis, R., et al., 2018. Anomalously weak Labrador Sea convection and Atlantic overturning during the past 150 years. Nature 556(7700), 227-230.

Tian, J., Wang, P., 2006. Tropical process and its periodicity in the deep sea records. Earth Science-Journal of China University of Geoscience 31(6), 747-753. (in Chinese)

Tian, J., Wang, P., Cheng X., 2004. Pleistocene precession forcing of the upper ocean structure variations of the southern South China Sea. Progress in Natural Science 14(6), 683-688. (in Chinese)

Timmermann, A., Friedrich, T., Timm, O.E., Chikamoto, M.O., Abe-Ouchi, A., Ganopolski, A., 2014. Modeling obliquity and CO_2 effects on Southern Hemisphere climate during the past 408ka. Journal of Climate 27(5), 1863-1875.

Timmermann, A., Justino, F., Jin, F., Krebs, U., Goosse, H., 2004. Surface temperature control in the North and tropical Pacific during the last glacial maximum. Climate Dynamics 23, 353-370.

Titchner, H.A., Rayner, N.A., 2014. The Met Office Hadley Centre sea ice and sea surface temperature data set, version 2:1. Sea ice concentrations. Journal of Geophysical Research: Atmospheres 119(6), 2864-2889.

Trauth, M.H., Asrat, A., Cohen, A.S., Duesing, W., Foerster, V., Kaboth-Bahr, S., et al., 2021. Recurring types of variability and transitions in the ~620 kyr record of climate change from the Chew Bahir basin, southern Ethiopia. Quaternary Science Reviews 266, 106777.

Trauth, M.H., Deino, A.L., Bergner, A.G., Strecker, M.R., 2003. East African climate change and orbital forcing during the last 175 kyr BP. Earth and Planetary Science Letters 206(3-4), 297-313.

Trenberth, K.E., Caron, J.M., 2001. Estimates of meridional atmosphere and ocean heat transports. Journal of Climate 14(16), 3433-3443.

Tuenter, E., Weber, S.L., Hilgen, F.J., Lourens, L.J., 2007. Simulating sub-Milankovitch climate variations associated with vegetation dynamics. Climate of the Past 3(1), 169-180.

Turner, J., Hosking, J.S., Phillips, T., Marshall, G.J., 2013. Temporal and spatial evolution of the Antarctic sea ice prior to the September 2012 record maximum extent. Geophysical Research Letters 40(22), 5894-5898.

Turney, C.S., Kershaw, A.P., Clemens, S.C., Branch, N., Moss, P.T., Fifield, L.K., 2004. Millennial and orbital variations of El Niño/Southern Oscillation and high-latitude climate in the last glacial period. Nature 428(6980), 306-310.

Tzedakis, P.C., 2010. The MIS 11-MIS 1 analogy, southern European vegetation, atmospheric methane and the" early anthropogenic hypothesis". Climate of the Past 6(2), 131-144.

Tzedakis, P.C., Channell, J.E.T., Hodell, D.A., Kleiven, H.F., Skinner, L.C., 2012. Determining the natural length of the current interglacial. Nature Geoscience 5(2), 138-141.

Tzedakis, P.C., Drysdale, R.N., Margari, V., Skinner, L.C., Menviel, L., Rhodes, R.H., et al., 2018. Enhanced climate instability in the North Atlantic and southern Europe during the Last Interglacial. Nature Communications 9(1), 4235.

Tzedakis, P.C., Raynaud, D., McManus, J.F., Berger, A., Brovkin, V., Kiefer, T., 2009. Interglacial diversity. Nature Geoscience 2(11), 751-755.

Tzedakis, P.C., Wolff, E.W., Skinner, L.C., Brovkin, V., Hodell, D.A., McManus, J.F., et al., 2012. Can we predict the duration of an interglacial?. Climate of the Past 8(5), 1473-1485.

Ulfers, A., Zeeden, C., Voigt, S., Abadi, M.S., Wonik, T., 2022. Half-precession signals in Lake Ohrid (Balkan) and their spatio-temporal relations to climate records from the European realm. Quaternary Science Reviews 280, 107413.

Ullman, D.J., LeGrande, A.N., Carlson, A.E., Anslow, F.S., Licciardi, J.M., 2014. Assessing the impact of Laurentide Ice Sheet topography on glacial climate. Climate of the Past 10(2), 487-507.

van den Heuvel, E.P.J., 1966. On the precession as a cause of Pleistocene variations of the Atlantic Ocean water temperatures. Geophysical Journal International 11(3), 323-336.

Vare, L.L., Massé, G., Gregory, T.R., Smart, C.W., Belt, S.T., 2009. Sea ice variations in the central Canadian Arctic Archipelago during the Holocene. Quaternary Science Reviews 28(13-14), 1354-1366.

Venancio, I.M., Mulitza, S., Govin, A., Santos, T.P., Lessa, D.O., Albuquerque, A.L.S., et al., 2018. Millennial-to orbital-scale responses of western equatorial Atlantic thermocline depth to changes in the trade wind system since the last interglacial. Paleoceanography and Paleoclimatology 33(12), 1490-1507.

Verschuren, D., Sinninghe Damsté, J.S., Moernaut, J., Kristen, I., Blaauw, M., Fagot, M., Haug, G.H., 2009. Half-precessional dynamics of monsoon rainfall near the East African Equator. Nature 462(7273), 637-641.

Vogel, H., Wagner, B., Zanchetta, G., Sulpizio, R., Rosén, P., 2010. A paleoclimate record with tephrochronological age control for the last glacial-interglacial cycle from Lake Ohrid, Albania and Macedonia. Journal of Paleolimnology 44, 295-310.

Wagner, A.J., Morrill, C., Otto-Bliesner, B.L., Rosenbloom, N., Watkins, K.R., 2013. Model support for forcing of the 8.2 ka event by meltwater from the Hudson Bay ice dome. Climate Dynamics 41(11-12), 2855-2873.

Wang, P., Jian, Z., Zhao, Q., Li, Q., Wang, R., Liu, Z., et al., 2003. Evolution of the South China Sea and monsoon history revealed in deep-sea records. Chinese Science Bulletin 48, 2549-2561.

Wang, P., Wang, B., Cheng, H., Fasullo, J., Guo, Z., Kiefer, T., et al., 2014. The global monsoon across timescales: coherent variability of regional monsoons. Climate of the Past 10(6), 2007-2052.

Wang, P., Wang, B., Cheng, H., Fasullo, J., Guo, Z., Kiefer, T., et al., 2017. The global monsoon across time scales: Mechanisms and outstanding issues. Earth-Science Reviews 174, 84-121.

Wang, Y., Lu, H., Yi, S., Huber, M., Yang, F., Gu, Y., et al., 2022. Tropical forcing orbital-scale precipitation variations revealed by a maar lake record in South China. Climate Dynamics 1-12.

Wara, M.W., Ravelo, A.C., Revenaugh, J. S., 2000. The pacemaker always rings twice. Paleoceanography 15(6), 616-624.

Wei, G., Deng, W., Liu, Y., Li, X., 2007. High-resolution sea surface temperature records derived from foraminiferal Mg/Ca ratios during the last 260 ka in the northern South China Sea. Palaeogeography, Palaeoclimatology, Palaeoecology 250(1-4), 126-138.

Wei, G., Li, X., Liu, Y., Shao, L., Liang, X., 2006. Geochemical record of chemical weathering and monsoon climate change since the early Miocene in the South China Sea. Paleoceanography 21(4), 227-235.

Weirauch, D., Billups, K., Martin, P., 2008. Evolution of millennial-scale climate variability during the mid-Pleistocene. Paleoceanography 23(3), PA3216.

Venancio, I.M., Mulitza, S., Govin, A., Santos, T.P., Lessa, D.O., Albuquerque, A.L.S., et al., 2018. Millennial-to orbital-scale responses of western equatorial Atlantic thermocline depth to changes in the trade wind system since the last interglacial. Paleoceanography and Paleoclimatology 33(12), 1490-1507.
Verschuren, D., Sinninghe Damsté, J.S., Moernaut, J., Kristen, I., Blaauw, M., Fagot, M., et al., 2009. Half-precessional dynamics of monsoon rainfall near the East African Equator. Nature 462(7273), 637-641.
Wolff, E.W., Fischer, H., Fundel, F., Ruth, U., Twarloh, B., Littot, G.C., et al., 2006. Southern Ocean sea-ice extent, productivity and iron flux over the past eight glacial cycles. Nature 440(7083), 491-496.
Wu, Z., Yin, Q., Ganopolski, A., Berger, A., Guo, Z., 2023. Effect of Hudson Bay closure on global and regional climate under different astronomical configurations. Global and Planetary Change 222, 104040.
Wu, Z., Yin, Q., Guo, Z., Berger, A., 2020. Hemisphere differences in response of sea surface temperature and sea ice to precession and obliquity. Global and Planetary Change 192, 103223.
Yin, Q., 2013. Insolation-induced mid-Brunhes transition in Southern Ocean ventilation and deep-ocean temperature. Nature 494(7436), 222-225.
Yin, Q., Berger, A., 2010. Insolation and CO2 contribution to the interglacial climate before and after the Mid-Brunhes Event. Nature Geoscience 3(4), 243-246.
Yin, Q., Berger, A., 2012. Individual contribution of insolation and CO2 to the interglacial climates of the past 800,000 years. Climate Dynamics 38(3-4), 709-724.
Yin, Q., Berger, A., 2015. Interglacial analogues of the Holocene and its natural near future. Quaternary Science Reviews 120, 28-46.
Yin, Q., Berger, A., Crucifix, M., 2009. Individual and combined effects of ice sheets and precession on MIS-13 climate. Climate of the Past 5(2), 229-243.

Yin, Q., Berger, A., Driesschaert, E., Goosse, H., Loutre, M. F., Crucifix, M., 2008. The Eurasian ice sheet reinforces the East Asian summer monsoon during the interglacial 500 000 years ago. Climate of the Past 4(2), 79-90.
Yin, Q., Guo, Z., 2006. Mid-Pleistocene vermiculated red soils in southern China as an indication of unusually strengthened East Asian monsoon. Chinese Science Bulletin 51, 213-220.
Yin, Q., Guo, Z., 2008. Strong summer monsoon during the cool MIS-13. Climate of the Past 4(1), 29-34.
Yin, Q., Wu, Z., Berger, A., Goosse, H., Hodell, D., 2021. Insolation triggered abrupt weakening of Atlantic circulation at the end of interglacials. Science 373(6558), 1035-1040.
Yiou, P., Jouzel, J., Johnsen, S., Rögnvaldsson, Ö.E., 1995. Rapid oscillations in Vostok and GRIP ice cores. Geophysical Research Letters 22(16), 2179-2182.
Yu, Z., Ding, Z., 2003. Nonlinear coupling between 100 ka periodicity of the paleoclimate records in loess and periodicities of precession and semiprecession. Science in China Series D: Earth Sciences 46, 1077-1087.
Zeng, Y., Chen, S., Yang, S., Liang, Y., Wang, Y., 2019. Multiscale analysis of Asian Monsoon over the past 640 ka. Science China Earth Sciences 62, 843-852.
Zhang, Z., Jansen, E., Sobolowski, S.P., Otterå, O.H., Ramstein, G., Guo, C., et al., 2023. Atmospheric and oceanic circulation altered by global mean sea-level rise. Nature Geoscience 1-7.
Zhao, Y., Tzedakis, P.C., Li, Q., Qin, F., Cui, Q., Liang, C., et al., 2020. Evolution of vegetation and climate variability on the Tibetan Plateau over the past 1.74 million years. Science Advances 6(19), eaay6193.

Publications and Presentations

1. Manuscripts in preparation:

Wu Z.P. et al. The half-precession signals during the Quaternary.

Wu Z.P. et al. Hemisphere differences in climate response to astronomical forcing, CO_2 and Northern Hemisphere ice sheets.

2. Publications in peer-reviewed journals:

Wu Z.P., Yin Q.Z., Ganopolski A., BergerA., Guo Z.T., 2023. Effect of Hudson Bay closure on global and regional climate under different astronomical configurations. Global and Planetary Change, 222, 104040.

Wu Z.P., Yin Q.Z., Liang M.Q., Guo Z. T., Shi F., Lu H., Su Q.Q., Lyu A.Q., 2023. The effect of astronomical forcing on water cycle: sea ice and precipitation. Chinese Science Bulletin, 68, 1-16.

Wu Z.P., Yin Q.Z., Guo Z.T., Berger, A., 2022. Comparison of Arctic and Southern Ocean sea ice between the last nine interglacials and the future. Climate Dynamics, 59, 519-529.

Wu Z.P., Yin Q.Z., Guo Z.T., Berger A., 2020. Hemisphere differences in response of sea surface temperature and sea ice to precession and obliquity. Global and Planetary Change, 192, 103223.

Yin Q.Z., **Wu Z.P.**, Berger A., Goosse H., Hodell D., 2021. Insolation triggered abrupt weakening of Atlantic circulation at the end of interglacials. Science, 373(6558), 1035-1040.

He Z.L., Zhang Z.S, Guo Z.T., Tan N., Zhang Z.J., **Wu Z.P.**, Zhang C.X., Deng, C.L., 2023. The spatial–temporal evolution of the Asian summer monsoon during the late Miocene and potential CO_2 forcing: A data–model comparison. Global and Planetary Change, 221, 104052.

Li T., Li G.J, Chen T.Y., Sun Y.B., Yin Q.Z, **Wu Z.P.**, Robinson L.F., Li L., Zhang Z.K., Meng X.Q., Zhao L., Ji J.F., Chen J., 2023. Ice volume and insolation forcing of abrupt strengthening of East Asian winter monsoon during glacial inceptions. Geophysical Research Letters, 50(3), e2022GL102404.

Ranathunga K.N., Finke P.A., Yin Q.Z., **Wu Z.P.,** Hao Q.Z., Lu H., 2023. Driving factors of interglacial paleosol formation on the Chinese loess plateau and the effect of precession and ice sheets. Quaternary Science Reviews, 300, 107911.

Jiang H.C., Yin Q.Z., Berger A., Wei L.H., **Wu Z.P.,** Wei X.T., Shi, W., 2023. Orbitally and galactic cosmic forced abrupt climate events during the last glacial period. Quaternary Science Reviews, 301, 107921.

Su Q.Q., Lyu A.Q., **Wu Z.P.,** Yin Q.Z., 2023. Diverse response of global terrestrial vegetation to astronomical forcing and CO_2 during the MIS-11 and MIS-13 interglacials. Climate Dynamics, 60, 375-392.

Askjær T.G., Zhang Q., Schenk F., Ljungqvist F.C., Lu Z.Y., Brierley C.M., Hopcroft P.O., Jungclaus J., Shi X.X., Lohmann G., Sun W.Y., Liu J., Braconnot P., Otto-Bliesner B.L., **Wu Z.P.,** Yin Q.Z., Kang Y.B., Yang H.J., 2022. Multi-centennial Holocene climate variability in proxy records and transient model simulations. Quaternary Science Reviews, 296, 107801.

Gao F.Y., Yang J.H., Xia D.S., Lu H., Wang S.Y., Li K.M., Wang Z.Q., **Wu Z.P.,** Zhou J.X., Shi F.X., 2022. Linking moisture and near-surface wind with winter temperature to reveal the Holocene climate evolution in arid Xinjiang region of China. Geoscience Frontiers, 13(6), 101433.

Lu H., Yin Q.Z., **Wu Z.P.,** Shi F., Hao Q.Z., Xia D.S., Guo, Z.T., 2022. Insolation and CO_2 impacts on the spatial differences of the MIS-9 and MIS-11 climate between monsoonal China and central Asia. Journal of Geophysical Research: Atmospheres, 127(12), e2022JD036505.

Xiao G.Q., Sun Y.Q., Yang J.L., Yin Q.Z., Dupont-Nivete G., Alexis L., Kehew A.E., Hu Y.Z., Geng J.Z., Dai G.W., Zhao Q.Y., **Wu Z.P.**, 2020. Early Pleistocene integration of the Yellow River I: Detritalzircon evidence from the North China Plain. Palaeogeography, Palaeoclimatology, Palaeoecology, 546, 109691.

He Z.L., Guo Z.T., Yang F., Sayem A.S.M., Wu H.B., Zhang C.X., Hao Q.Z., Xiao G.Q., Han L., Fu Y., **Wu Z.P.**, Hu B., 2019. Provenance of Cenozoic Sediments in the Xining Basin Revealed by Nd and Pb Isotopic Evidence: Implications for Tectonic Uplift of the NE Tibetan Plateau. Geochemistry, Geophysics, Geosystems, 20, 4531-4544.

3. Presentations at conferences and workshops:

Wu Z.P., Yin Q.Z., Guo Z.T., Berger A., Comparison of Arctic and Southern Ocean sea ice between the last nine interglacials and the future. EGU General Assembly, Vienna, Austria, May 23-27, 2022. (Oral Presentation)

Wu Z.P., Yin Q.Z., Guo Z.T., Berger A., Insolation and CO_2 induced variations in the sea ice of the last nine interglacials and their comparison with the future. 6th PAGES Open Science Meeting, online, May 16-20, 2022. (Oral Presentation)

Wu Z.P., Yin Q.Z., Guo Z.T., Berger A., The different response of the climate system to astronomical parameters, GHG and ice sheets during past interglacials. Belgian National Comittee for Geodesy and Geophysics Study day on ‘Belgian contributions to Earth Sciences in a Changing World’, Brussels, Belgium, November 4-4, 2022. (Poster Presentation)

Wu Z.P., Yin Q.Z., Guo Z.T., Berger A., Insolation and CO_2 induced variations in the sea ice of the last nine interglacials and their comparison with the future. ICP14: 14th International Conference on Paleoceanography, Bergen, Norway, August 29-September 2, 2022. (Poster Presentation)

Wu Z.P., Yin Q.Z., Berger A., Guo Z.T., Hemisphere differences in response of sea surface temperature and sea ice to precession and obliquity. Geology and Earth Sciences Webinar-2020, online, November 12-13, 2020. (Oral Presentation)

Wu Z.P., Yin Q.Z., Berger A., Guo Z.T., Hemisphere differences in response of sea surface temperature and sea ice to precession and obliquity. EGU General Assembly, online, May 3-8, 2020. (Oral Presentation)

Wu Z.P., Yin Q.Z., Berger A., Guo Z.T., Different response of the Northern and Southern Hemisphere climates to obliquity and precession. BELQUA 2019 Annual Scientific Workshop, Brussels, Belgium, February 22, 2019. (Oral Presentation)

Wu Z.P., Yin Q.Z., Berger A., Guo Z.T., Different response of the Northern and Southern Hemisphere climates to obliquity and precession. EGU General Assembly, Vienna, Austria, April 7-12, 2019. (Poster Presentation)

Wu Z.P., Yin Q.Z., Berger A., Guo Z.T., The difference of hemispheric climates under the influence of astronomical forcing. INQUA Congress, Dublin, Ireland, July 25-31, 2019. (Poster Presentation)

Lu H., Yin Q.Z., **Wu Z.P.,** Shi F., Hao Q.Z., Xia D.S., Guo Z.T., Impacts of insolation and CO_2 on the spatial differences of the MIS-9 and MIS-11 climate between monsoonal China and central Asia. EGU General Assembly, Vienna, Austria, May 23-27, 2022. (Oral Presentation)

Ranathunga N., Finke P., Yin Q.Z., **Wu Z.P.,** Yu Y.Y., The Effect of Quaternary climate change on paleosol development by soil-climate modeling. EGU General Assembly, Vienna, Austria, May 23-27, 2022. (Oral Presentation)

Yin Q.Z., **Wu Z.P.,** Berger A., Goosse H., Hodell D., Astronomical forcing as a trigger of abrupt climate changes at the end of interglacials. EGU General Assembly, Vienna, Austria, May 23-27, 2022. (Oral Presentation)

Su Q.Q., Lyu A.Q., **Wu Z.P.,** Yin Q.Z., Diverse response of global climate and vegetation to astronomical forcing and CO_2 during MIS-11 and MIS-13. 6th PAGES Open Science Meeting, online, May 16-20, 2022. (Oral Presentation)

Yin Q.Z., **Wu Z.P.,** Berger A., Goosse H., Hodell D., Astronomically-induced abrupt cooling at the end of the last interglacial. 6th PAGES Open Science Meeting, online, May 16-20, 2022. (Oral Presentation)

Ranathunga N., Finke P., Yin Q.Z., **Wu Z.P.,** Modelling the effect of climate, dust deposition and ice sheets on paleosol development on the Chinese Loess Plateau. BELQUA annual workshop, Brussels, Belgium, March 29, 2022. (Oral Presentation)

Yin Q.Z., **Wu Z.P.,** Insolation triggered abrupt climate changes confirmed by speleothem records. Climate Change, The Karst Record IX (KR9), Innsbruck, Austria, July 17-20, 2022. (Oral Presentation)

Liang M.Q., Yin Q.Z., Li H.C, Sun Y., **Wu Z.P.,** Asynchronous Holocene Optimum in East Asia monsoon region recorded by stalagmites and its underlying climate dynamics. Climate Change, The Karst Record IX (KR9), Innsbruck, Austria, July 17-20, 2022. (Oral Presentation)

Su Q.Q., Lyu A.Q., **Wu Z.P.,** Yin Q.Z., Diverse Response of Global Climate and Vegetation to Astronomical Forcing and CO_2 During MIS-11 and MIS-13. Belgian National Comittee for Geodesy and Geophysics Study day on ‘Belgian contributions to Earth Sciences in a Changing World’, Brussels, Belgium, November 4-4, 2022. (Poster Presentation)

Yin Q.Z., **Wu Z.P.,** Berger A., Goosse H., Hodell D., Insolation threshold triggered abrupt changes of Atlantic overturning circulation at the end of interglacials. Belgian National Comittee for Geodesy and Geophysics Study day on ‘Belgian contributions to Earth Sciences in a Changing World’, Brussels, Belgium, November 4-4, 2022. (Poster Presentation)

Yin Q.Z., **Wu Z.P.,** Berger A., Goosse H., Hodell D., Insolation threshold triggered abrupt changes of Atlantic overturning circulation at the end of interglacials. ICP14: 14th International Conference on Paleoceanography, Bergen, Norway, August 29-September 2, 2022. (Poster Presentation)

Su Q.Q., Yin Q.Z., Lyu A.Q., **Wu Z.P.,** The response of global terrestrial vegetation to orbital forcing and CO_2 during MIS 11 and MIS 13. 7th International Geologica Belgica Meeting, Brussels, Belgium, September 15-17, 2021. (Poster Presentation)

Su Q.Q., Yin Q.Z., **Wu Z.P.,** The Roles of Astronomical Forcing and CO_2 in Global Vegetation Distribution During Nine Interglacials in the Past 800,000 Years. AGU Fall Meeting, online, December 1-17, 2020. (Poster Presentation)

Yin Q.Z., **Wu Z.P.**, Hodell D.A., Quiquet A., Berger A., Goosse H., Ramstein G., Insolation threshold as a trigger of abrupt oscillations in AMOC at the end of interglacials. AGU General Assembly, San Francisco, America, December 9-13, 2019. (Oral Presentation)

Xiao G.Q., Sun Y.Q., Yang J.L., Yin Q.Z., Dupont-Nivet G., Licht A., Kehew A., Xu Q.M., Hu Y.Z., Geng J.Z., Wang Z.X., Dai G.W., **Wu Z.P.**, Yellow River integration linked to Pleistocene increased climate instability. EGU General Assembly, Vienna, Austria, April 7-12, 2019. (Oral Presentation)